UNDERSTANDING LONG TIMESCALE PHENOMENA IN ATOMIC SYSTEMS FROM ACCELERATED MOLECULAR SIMULATION METHODS

BY

NATHAN PELLER WALTER

DISSERTATION

Submitted in partial fulfillment of the requirements
for the degree of Doctor of Philosophy in Nuclear, Plasma, and Radiological Engineering
in the Graduate College of the
University of Illinois at Urbana-Champaign, 2019

Urbana, Illinois

Doctoral Committee:

Associate Professor Yang Zhang, Chair and Director of Research
Professor Brent Heuser
Professor David Ruzic
Professor Kenneth Schweizer

Abstract

Conventional molecular dynamics simulations have been proven instrumental to the understanding of material behaviors. However, the temporal constraints of molecular dynamics simulations have limited attempts to capture long timescale dynamics of material systems, such as phase transitions or dynamics of supercooled liquids. This class of phenomena often requires the crossing by thermal activation of large energy barriers, which represent transition states separating two stable or metastable states of a system. Therefore, we propose two methods to simulate the escape of a system from a metastable state to a transition state, which, when repeated, leads to atomic trajectories of extremely slow or rare phenomena of non-equilibrium matter. The first method, all-atom Metadynamics, is a version of the popular advanced sampling method Metadynamics. By biasing over all atoms rather than collective variables, all-atom Metadynamics samples the potential energy landscape in all-atom dependent variable space. All-atom Metadynamics utility is displayed by studying the nucleation and crystal growth of a model Lennard-Jones Argon system, while also displaying the computational downside of Metadynamics, the scaling over simulation time. Thus, the second method, Varied Steepness Ascent Dynamics (Ascent Dynamics), is introduced as an alternative method with constant computational scaling over simulation time. Ascent Dynamics, based on former surface walking methods, is first verified and validated on several mathematical problems and on vacancy diffusion in a Lennard-Jones system, respectively, followed by application of the method to a two-dimensional polydisperse model liquid. Ascent Dynamics is shown to accurately sample the potential energy landscape without the large computational overhead.

To those who matter most, my parents, my partner, and my best friend

Acknowledgments

First, I would like to thank my parents, my friends, and my roommates for always supporting me and listening to my complaints when I was stressed and tired. I would also like to thank my lab mates Abhishek Jaiswal and Zhikun Cai for their useful discussions of results, for patiently teaching me when I first joined the group, and especially for helping me with codes and scripts.

I would particularly like to thank my friends Tish and Grace. They have been my support, my friend, and even my chauffeur. No truer friends exist, they will be the hardest part of leaving Champaign.

Most importantly, I would like to thank Professor Yang Zhang (Y Z) for his clairvoyant guidance, insightful mentoring, and patient help during this project. He has been invaluable to this work as well as my development as a graduate student and as a person.

Table of Contents

List of Tables

List of Figures

List of Abbreviations

BOP	Bond orientational order parameter
PEL	Potential Energy Landscape
MD	Molecular Dynamics
MC	Monte Carlo
MTD	Metadynamics
LJ	Lennard-Jones
BCC	Body centered cubic
FCC	Face centered cubic
HCP	Hexagonal close packing
liq	Liquid State
IE	Inherent Energy
CNT	Classical Nucleation Theory
NVT	Constant number, volume, and temperature
NPT	Constant number, pressure, and temperature
ART	Activation Relaxation Technique
GAD	Gentlest Ascent Dynamics

List of Symbols

$\bar{q}_6$	Sixth-order, first nearest-neighbor averaged, bond orientational order parameter
T_m	Melting temperature
T_g	Glass transition temperature
ϕ	Penalty Potential Energy Function
α	Newton's Steepest Descent Step Size
δ	Force Step Size

Chapter 1

Long Timescale Phenomena and the Energy Landscape

1.1 Multi-scale Multi-physics Modeling

Without argument, some of the most interesting phenomena in material science occur out of equilibrium, such as phase change, chemical reactions, vitrification, protein folding, aging, self assembly, etc. While these materials differ in classification, they all share the commonality of either occurring over long timescales or beginning via an extremely rare event. For example, the dynamics of deeply supercooled liquids can exceed the seconds timescale, or similarly, protein folding can have timescales ranging from microseconds to minutes depending on the temperature and the protein [9, 6]. Further, in engineering, the aging and degradation of materials, an essential phenomena in predicting long-term behavior of a material, can occur over years and decades [10].

Despite extensive efforts spent in studying these systems, a complete understanding of these materials from an atomic level is still lacking. One difficulty with studying these methods results from the atomic nature of the events. Many of these systems need information on the atomic scale. This heavily limits the number of experimental and computational methods capable of accessing these phenomena. Particularly, the atomic scale is traditionally studied with molecular dynamics (MD) and Monte Carlo (MC) methods, which are limited to short timescales (microseconds at best) and only structural information respectively, as partially shown in Figure 1.1. While molecular dynamics timescales are sufficient for studying equilibrium physics, it is often incapable of sufficiently sampling rare events and out-of-equilibrium dynamics. On the other hand, to simulate long timescales, most available methods simulate large length scales. As a result, there is a known linear correlation between the length and time scales of the computational methods available, as shown in Figure 1.1 [11]. Although, it is worth noting that the length of molecular dynamics simulations scales similarly to Moore's Law, and thus, as computers become more powerful, these systems timescales may become achievable by standard computers, however, currently the longest timescale available to molecular dynamics is in the micro to milli seconds.

Several books have been dedicated to this problem including [12, 13], in which a current understanding of the problem and common methods or solutions are reviewed. This thesis wishes to contribute to the question of how to simulate and understand long timescale phenomena on a molecular and atomic level. The region of time and length we are referring to are indicated in Figure 1.1, or timescales longer than milli seconds while on an atomic scale. The remainder of this chapter will cover the basis for most computational methods for studying long timescales of atomic behavior, the energy landscape, followed by a review of popular methods for this problem.

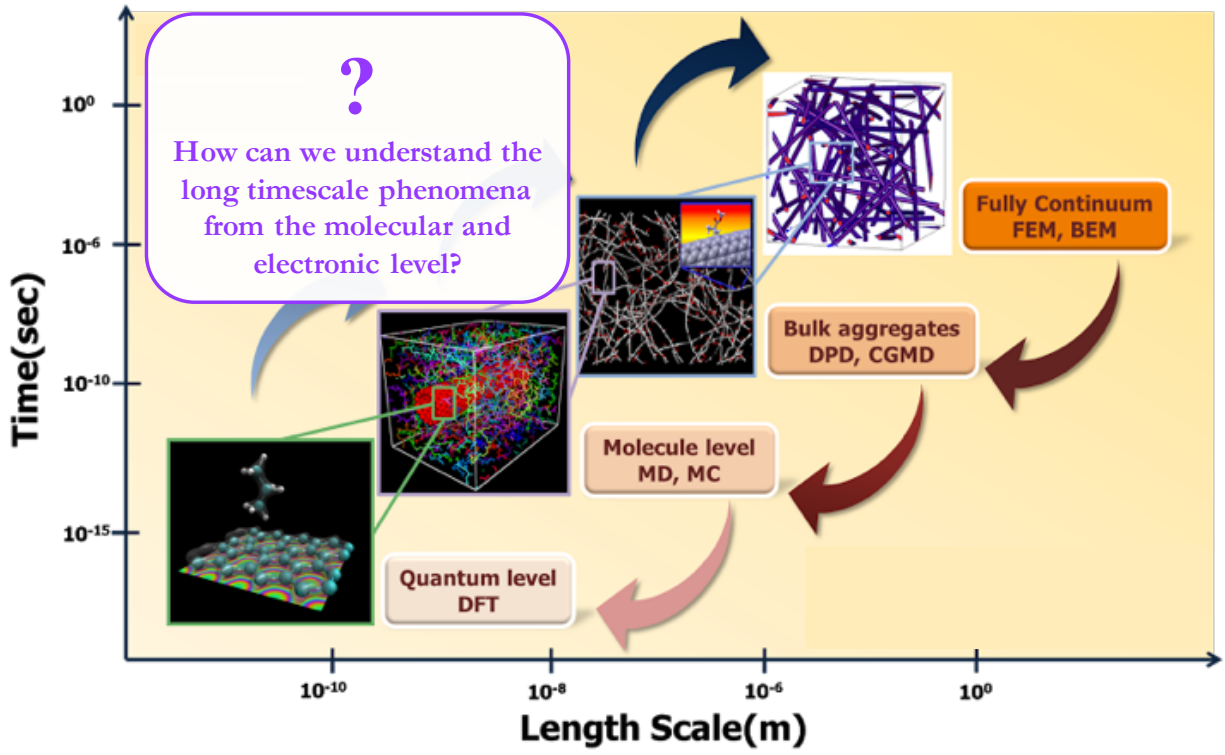

Figure 1.1: Computational methods plotted to show the length scale and timescale regions they are appropriate for studying. The Figure shows that traditionally the length scale and timescale are correlated, and until the invention of Metadynamics, no method was able to study the long timescale on the atomic length scale. Adapted from [3]

1.2 Energy Landscape Formulation

Because long timescale and rare event phenomena is often difficult to study experimentally or computationally, the recent energy landscape framework has garnered a great deal of attention to aid in explanation of material systems. The framework originally proposed by Goldstein [14], Stillinger and Weber [15, 16, 17, 4],

the study of viscous liquids and the glass transition, and has been extended to explain the dynamics of a plethora of systems. The energy landscape framework is rather intuitive despite its high dimensional complexity. Figure 1.2 displays a schematic drawing of the energy landscape as it pertains to liquids and solids [4]. As Figure 1.2 shows, the energy landscape is divided into energy basins and energy barriers, and is con-

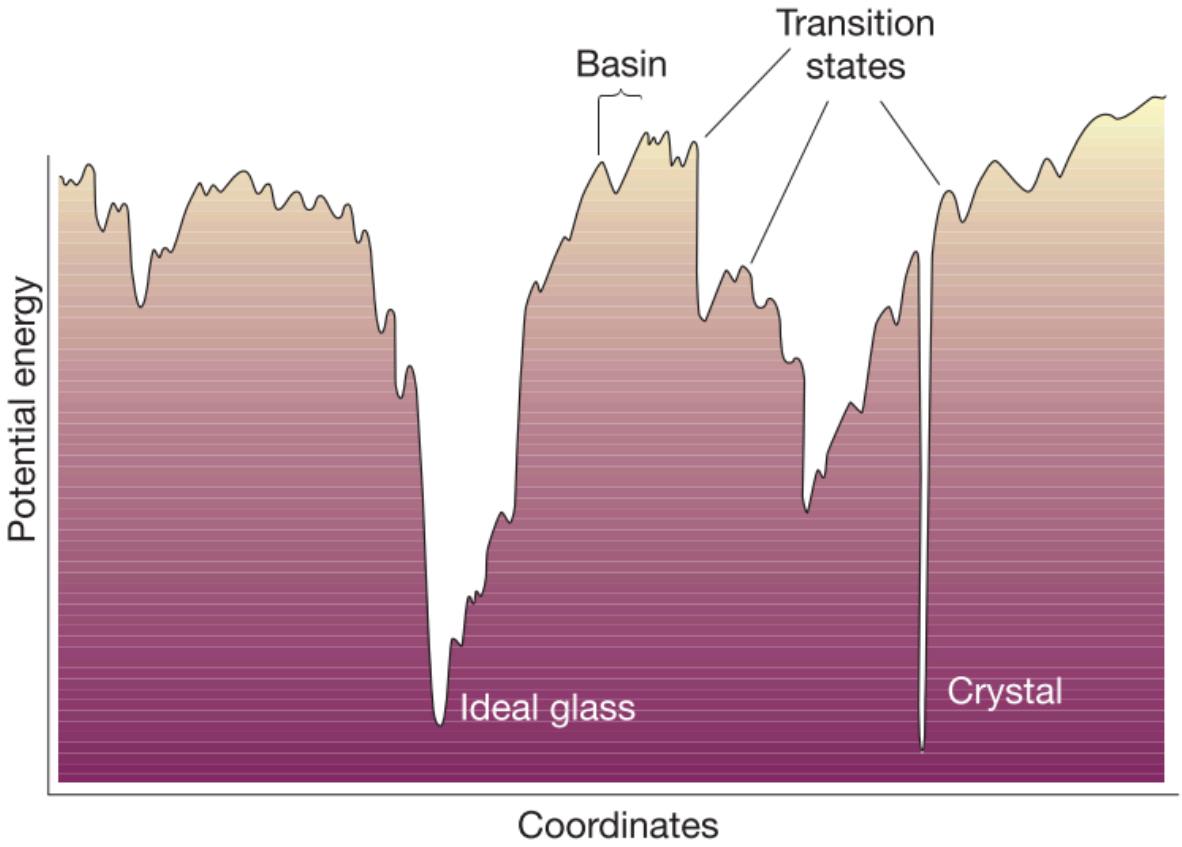

Figure 1.2: Schematic image of the potential energy landscape, adapted from [4]. A schematic plot of the potential energy landscape in 2-D (potential energy versus 1 configurational coordinate). The true potential energy landscape is multi-dimensional depending on the number of configurational coordinates; the dimensionality can range from 1 to 3N if all atoms coordinates are used.

sidered a function of the system configuration. While this figure displays the landscape as a two-dimensional image (one degree of freedom, coordinates), most energy landscapes are hyper-dimensional. The landscape considers the basins to be different structures of the system. Of note, the deepest minimum corresponds to the crystal state, and other higher energy states to be thermodynamically metastable states. The barriers separating these basins correspond to the dynamics of the system (maximums in the figure, saddle points

on a true landscape). Often, the small local barriers represent short time dynamics, and larger barriers separating deep minimum represent long timescale phenomena [18]. The schematic here provides an excellent framework for explaining the dynamics of materials in and out of equilibrium, particularly for describing the timescales of rare events. With this picture in mind, a system's dynamics can be described as a series of basins and barriers, gradually sampling a trajectory over a large portion of the landscape [15, 16, 17, 4].

The energy landscape has been a novel success for describing several different phenomena including both in and out of equilibrium, the relaxation of metastable materials, and many more; however, application of the energy landscape is primary focused on theoretical explanations. Generally, the landscape is drawn to describe the system from a fundamental understanding. At the moment, no experimental methods exist to verify the energy landscape, and only a handful of computational methods exist to verify the landscape theories. The energy landscape has been the focus of several books to describe phenomena from biological systems to vitrification of liquids and much more [19, 20]. These books have employed various methods to approximate the energy landscape or focused on systems with analytical energy landscapes.

The landscapes for different types of material systems and dynamics, such as glasses, crystallization, and protein folding, differ significantly. Briefly, the energy landscape for liquids is considered to be fairly level with small barriers, allowing the system to flow to any configuration on the landscape [16]. As the system is cooled below the melting temperature, the dynamics of the system slows down, and the energy landscape begins to influence the system. For crystal-forming liquids, the landscape is generally theorized to be funnel shaped with small barriers along the walls creating metastable states. This funnel-like structure allows the system to easily find the deep crystal basin and nucleate into a crystal. Conversely, a glass-forming liquid will enter a supercooled state where the landscape is diverse in basins and energy barriers. In this case, the landscape is more akin to a mountain range, where large mountains (barriers) represent collective long-time dynamics (α relaxations) and local hills (barriers) represent local rearrangements of the system (β relaxations) [17, 4]. Finally, protein systems are theorized to have a landscape between a crystal former and a glass former. The general shape is a funnel, however, many deep basins and large barriers allow for metastable mutant and misfolded states on the landscape [21, 22].

While, Figure 1.2 shows model potential energy landscape [4], it is important to note that in this schematic drawing the potential energy landscape has been reduced to a dependent on a single variable, the configurational coordinates, for simplicity and for display. However, a typical potential energy landscape is hyperdimensional ranging from one dimension to 3N dimensions, where N is the number of atoms in the system. Examples of configurational coordinates, or often referred to as collective variables in this thesis, are the bond angles or radius of gyration in proteins [23], the system bond orientational order parameter for ordered

structures [24], and the position of atoms on a region of interest [25, 26]. The more degrees of freedom the higher the dimension of the energy landscape, and the more complex the problem of sampling or computing the landscape becomes. As a result of the dimensionality problem, methods focused on the calculation of the landscape reduce the landscape to a few collective variables believed to explain the dynamics of interest.

The strength of the energy landscape is that the height of the barriers separating two basins and the value of the potential energy minimum can be used to explain dynamic behavior. Particularly, the probability of occupying a particular potential energy minimum with energy G is proportional to $\exp(\frac{-G}{k_B T})$ [27]. Thus, at high temperatures, the system can occupy both high and low energy minimums with high likelihood, while at lower temperatures, the system tends to occupy the lower energy minimums [27]. Similarly, the dynamics and many properties of the system, such as viscosity, are proportional to the height of the barriers separating configurations, and can be computed as proportional to $\exp(\frac{\Delta G}{k_B T})$ [25, 26]. Therefore, the strength of the landscape is that with a understanding of the landscape one can unveil a great deal of information about a systems structural and dynamical behavior.

It is the goal of this thesis to develop an efficient method for sampling or calculating this energy landscape for a given material. In an ideal case, if a system's complete energy landscape is known, much of the material's behavior and properties are also known. Thus, a method that can provide a statistically significant sampling of the landscape can provide accurate estimates to the material's behavior. The next section will cover some of the popular and common methods to sample the energy landscape and ergo sample dynamics outside the range of molecular dynamics.

1.3 Advanced Sampling Techniques

Recently, a new set of computational methods have been developed to probe the energy landscape, generally referred to as advanced sampling methods, which belong to a few sub categories. All of these methods fall within the region of Figure 1.1 of interest, but vary greatly in computational efficiency, required knowledge, and amount of landscape reduction.

The first category of advanced sampling methods are accelerated molecular dynamics methods. These methods use various algorithms to extend the timescale or configurational sampling of molecular dynamics and Monte Carlo. This category of methods include parallelizing the simulation over time [28]; parallel replica sampling which runs several simulations in parallel and swaps the configurations along the simulation to enhance configurational sampling [29]; Swap Monte Carlo which as a Monte Carlo scheme swaps atom locations rather than the standard scheme based on energy [30]; standard molecular dynamics which relies

on building bigger and optimized computers to extend the timescale of molecular dynamics [31]; and others.

The second category of methods is energy or force biasing methods. In general, these methods add a penalizing or biasing function to the system either directly to the potential energy or via the force to drive the system out of configurations of deep minimums on the energy landscape. Biasing methods are constructed from the energy landscape formalism. These methods include accelerated molecular dynamics which adds a energy bias to the system when the energy is below a threshold value to discourage sampling of low energy minimums [32]; Metadynamics which applies a bias to the potential energy continuously until the energy landscape is filled with the bias the sum of which is the inverse of the potential energy landscape [33, 34, 35]; Adaptive Force Biasing which applies a bias force to the system during the simulation to increase free energy sampling [36]; and others. A extensive review of the methods can be found in [37, 38, 39, 40]. Further, a review of Metadynamics and how to appropriately estimate collective variables can be found at [41].

Of particular interest for its broad success, application, and enhancements is Metadynamics. Metadynamics was originally proposed by Laio and Parrinello [33], and has since then been implemented for a range of applications. Metadynamics is broadly performed as follows. First, molecular dynamics simulations of a system are performed during which, a penalty energy function, usually of Gaussian shape, is periodically applied to the system. Generally, the penalty function and the energy landscape sampled is based on a collective variable of the system, for example bond angles or structure factor [42], as this reduces the dimensionality and the computational cost. The simulation terminates when the free energy landscape is "filled", another reason for reduced dimension landscapes as these require less penalties to converge to a filled landscape.

Alternatively, another form of Metadynamics, created by Kushima et al., applies penalty functions to fill a local minimum to drive the system from one minimum to another and samples the potential energy landscape [25]. This form of Metadynamics, or the Autonomous Basin Climbing method, has been applied to study viscosity, slow creep, defect activation, and more [43]. By sampling the basins and barriers of the landscape, the energy values along with a temperature mapping scheme were used to equate the barrier heights to the properties of the materials [43].

The third category of methods are string based methods, also known as saddle searching methods and surface walking methods. These methods come in two categories, single-ended and double-ended. Single-ended methods use information from the current minimum to search out a nearby saddle or transition state on the landscape. These methods include the activation relaxation technique (ART) which approximates the lowest direction of curvature from the force to move uphill to a transition state [44]; and gentlest ascent dynamics (GAD) which approximates the lowest direction of curvature by power iterating the Hessian matrix

to converge to a saddle point [45]. Double-ended methods use information of the starting configuration and the end configuration to compute the transition pathway between the two configurations. Methods include the nudged elastic band which uses a series of nodes between the two configurations and minimizes the energy of each node in a tangential direction to compute the transition pathway [46]; the growing string method which uses intelligent placement of it's initial nodes to converge to pathways more efficiently than more naive methods that place the nodes evenly along a tangential pathway between the starting and end point of the reaction [47]; and the minimum action method (MAM) which distances the nodes more efficiently so that clustering of nodes on the pathway is less likely to occur [48]. A comparison of the speeds of several of these methods is presented in [49]. Further, a review of minimum curvature methods can be found in [50], covering, power iterative methods, Lanczos methods, and dimer methods.

While each class of methods and each method itself has been incremental to improving advanced sampling and have provided novel insights to many problems and systems, there are draw backs to each method. Many require collective variables in order to achieve reasonable computational costs, which descriptive collective variables are not always available. Further, surface walking methods generally assume that the lowest direction of curvature is sufficient for a systems dynamics behavior, however, as will be discussed in Chapter 3, the lowest direction is not always descriptive of the system's dynamics. Thus, Metadynamics is covered more thoroughly in Chapter 2 as the work in my Master's is an extension of the Metadynamics method. Further, Gentlest ascent and activation relaxation technique are covered more thoroughly in Chapter 3 as they provide a motivation and background for Ascent Dynamics

1.4 Overview and Organization

The outline of the remaining report is as follows. In Chapter 2, a portion of my master's work is presented along with some further analysis since the original production. We represent the operating theory and algorithms for the method, along with application of the method to a model liquid to study nucleation and crystal growth. The work in the following chapters can be considered an extension of the work in my Master's, thus, Chapter 2 is presented as motivation and background. In Chapter 3, after discussing some of the computational pitfalls of Metadynamics and other biasing methods, we propose a, to the best of our knowledge new, surface walking method, Ascent Dynamics, for sampling the energy landscape. The method is based on previous surface walking methods, briefly mentioned above. Chapter 3 covers the formulation, verification, and validation of the method as well as establishes the need for a new method. In Chapter 4, Ascent Dynamics is applied to a model liquid system in order to show the capability of the method to

unveil dynamics of complex landscaped systems. In Chapter 5, computing the time scale of the simulations from the energy landscape will be discussed. The methods to compute the time scale from the landscape are independent of the method for computing the energy landscape (Metadynamics or Ascent Dynamics, or methods not discussed in this thesis), and are demonstrated on multiple systems. Finally, in Chapter 6, a summary of the work is discussed and future work directions are discussed briefly. In the appendix, additional information for implementing the Metadynamics method and additional potentials used to support the Ascent Dynamics method are included.

Chapter 2

All-Atom Metadynamics Simulations of Nucleation and Crystal Growth

2.1 Preface

This chapter is considered as a continuation of my Master's Thesis work [5]. Portions of this work were originally published in the master's work, particularly, the method formulation and development as a code source, and the original simulation [5]. However, further analysis has revealed new understandings and this work provides a solid background and motivation for the original work performed in the following chapters.

2.2 Introduction

Metadynamics, one of the more popular advanced sampling methods, has successfully been used to study a wide range of material phenomena including viscosity, slow creep, defect activation, protein folding and more [43]. Since the original formulation of well-tempered Metadynamics, many extensions have been made to improve the Metadynamics method. Here, we will represent an extension on the Metadynamics method to apply the biasing penalty functions to all atoms in a system rather than predefined collective variables as is typically done. The formulation of the method and key considerations is covered here to motivate the following chapters, however, substantially more information about considerations needed for a Metadynamics simulation, implementation of the method, and method details are provided in [5]. All-atom Metadynamics is then applied to a model liquid system to study nucleation and crystal growth. While the original data was collected for [5], further analysis has unveiled a potential approach for approximating the classical nucleation theory parameters from a Metadynamics simulation. Lastly, potential directions of future work with the Metadynamics method or nucleation is presented.

2.3 Metadynamics Literature Review

2.3.1 All-Atom Metadynamics

All-atom Metadynamics is an extension of the original Metadynamics of Laio and Parrinello [33], and the extension by Kushima et al [26, 25], and is adapted from [5]. The method's formulation is as follows, with a schematic illustration of the method presented in Figure 2.1. All-atom Metadynamics simulations begin with an arbitrary system configuration, typically a metastable configuration if energy minimization has been performed prior. Figure 2.1 shows the initial configuration on the potential energy landscape. The system configuration during the simulation is represented by $\mathbf{r}$, and the system potential energy is represented by $U(\mathbf{r})$. From a minimized configuration, we add a penalty function ϕ

$$\phi(\mathbf{r}, \mathbf{r}^{\alpha}_{\text{min}}) = H \exp\left(\frac{-\left(\mathbf{r} - \mathbf{r}^{\alpha}_{\text{min}}\right)^2}{2\sigma^2}\right) \tag{2.1}$$

where $\mathbf{r}^{\alpha}_{\text{min}}$ is the configuration where penalty α is applied, α represents the index of the penalties applied, H is the height of the penalty function, and σ is the width of the penalty function. While the penalty function can be of any arbitrary shape, we choose to use a multivariate Gaussian function because it is symmetric in all directions and quickly decays. A Gaussian function is also local on the landscape, so penalties applied in one minimum are unlikely to affect the landscape in nearby minimums. If the function does not locally decay, the biasing penalty may affect surrounding basins and saddle points. This added potential results in a force on each atom of

$$\mathbf{F}^{\alpha}(\mathbf{r}, \mathbf{r}^{\alpha}_{\text{min}}) = -\nabla\phi(\mathbf{r}, \mathbf{r}^{\alpha}_{\text{min}}) \tag{2.2}$$

$$\mathbf{F}^{\alpha}(\mathbf{r}, \mathbf{r}^{\alpha}_{\text{min}}) = \frac{H}{\sigma^2}\left(\mathbf{r} - \mathbf{r}^{\alpha}_{\text{min}}\right) \exp\left(\frac{-\left(\mathbf{r} - \mathbf{r}^{\alpha}_{\text{min}}\right)^2}{2\sigma^2}\right) \tag{2.3}$$

While the goal of all-atom Metadynamics is to bias the energy landscape, for implementation of the method, the system's force is modified by the addition of this biasing force. By maintaining the penalties applied at all locations α, the total system potential and force become

$$\begin{aligned} \Phi(\mathbf{r}) &= U(\mathbf{r}) + \sum_{\alpha} \phi(\mathbf{r}, \mathbf{r}^{\alpha}_{\text{min}}) \\ \mathbf{F}(\mathbf{r}) &= \mathbf{F}_{pp}(\mathbf{r}) + \sum_{\alpha} \mathbf{F}^{\alpha}(\mathbf{r}, \mathbf{r}^{\alpha}_{\text{min}}) \end{aligned} \tag{2.4}$$

where $\mathbf{F}_{pp}(\mathbf{r})$ is the force generated from the pair potential, $\Phi(\mathbf{r})$ is the potential energy of the system and the penalty functions, $U(\mathbf{r})$ is the potential energy of the system without the penalty functions, and $\mathbf{F}(\mathbf{r})$ is

the force applied to the system with the penalties applied. The addition of the penalty functions alters the potential energy and the force acting on the atoms of the system. Figure 2.1 B illustrates the added penalty energy in blue, and shows the total potential energy landscape has changed from figure panel A to B.

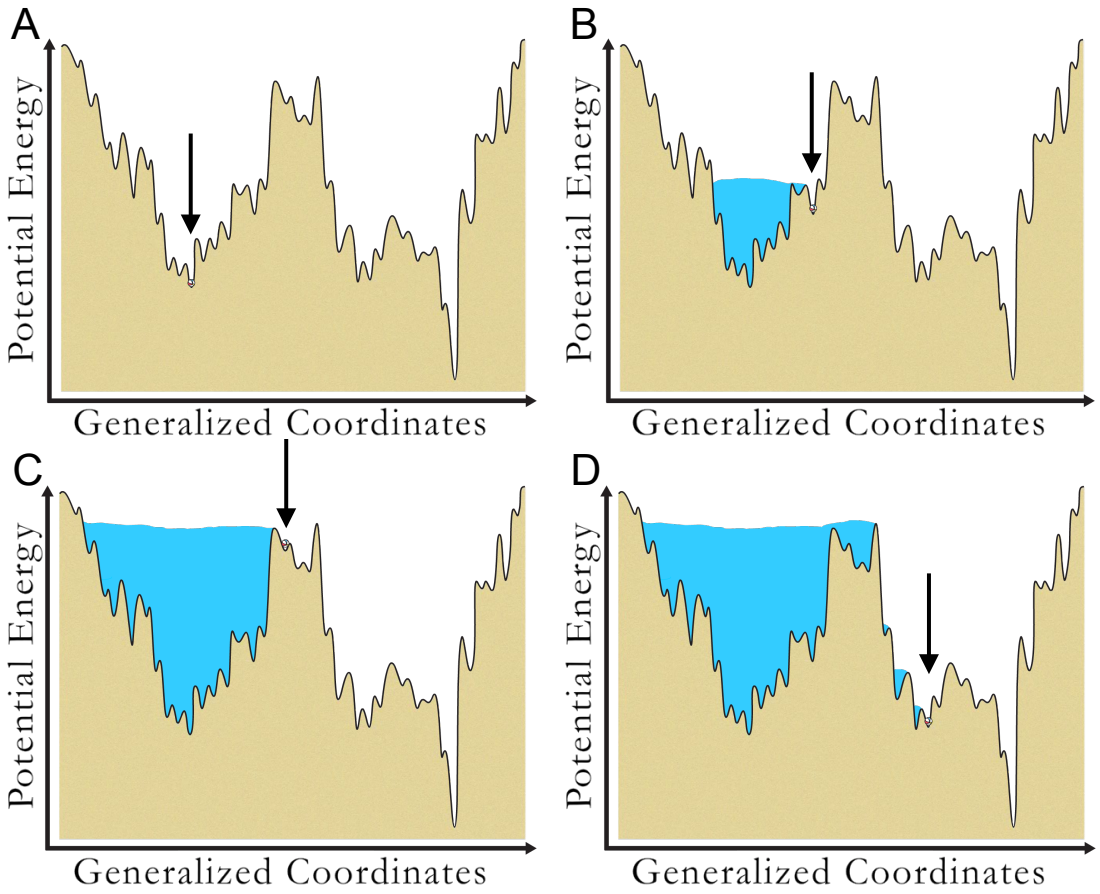

Figure 2.1: Four panel figure illustrating the all-atom Metadynamics method of a system on a potential energy landscape. Here, the tan region represents the original potential energy landscape $U(\mathbf{r})$, the blue region is the added biasing penalty functions, the ball represents the current system configuration, and the arrow is a guide for the eye. The vertical axis is the potential energy of the system as a function of generalized coordinate, which can be a collective variable or the system configuration in 3N. Adapted from [5]

The system's configuration is then updated by performing steepest descent on the modified potential energy, particularly,

$$\begin{aligned} \mathbf{r}_{i+1} &= \mathbf{r}_i - \delta \nabla \Phi(\mathbf{r}) \\ &= \mathbf{r}_i + \delta \mathbf{F}(\mathbf{r}) \end{aligned} \tag{2.5}$$

where i is the iteration of Newton's steepest descent, and δ is the step size of each iteration. Here, δ determines the speed and scale of the convergence of the method to the local minimum; smaller values result

in less error but larger values converge faster. After converging to a new minimum, the configuration is in a new local minimum of Φ-space, but not necessarily of U-space. This configuration is denoted $\mathbf{r}_{\min}^{\alpha+1}$. With the system converged to a minimum on Φ-space, the algorithm is repeated with a new penalty applied at the location of $\mathbf{r}_{\min}^{\alpha+1}$. To prevent the system from re-sampling previous visited minimums and to ensure the system overcomes the nearby barriers, the penalties are maintained throughout the simulation. The computational cost of this history-dependence on the penalties will be discussed further in the next chapter.

To illustrate the all-atom Metadynamics method, Figure 2.1 shows a schematic of a complete all-atom Metadynamics simulation. Panel A shows the system starting in an energy minimum of the original energy landscape. From panel A to panel B, a series of penalty functions (blue) have been applied to the system resulting in a modified potential energy landscape. The penalty functions and steepest descent forces the system from the original energy minimum to a new energy minimum. From panel B to panel C, further additions of penalty functions results in the left side of the landscape becoming inaccessible, and the system is driven over large energy barriers on the landscape to a new area of the original landscape. Lastly, from panel C to panel D, the system is driven over a large energy barrier separating two distinct regions of the landscape, allowing the system to sample a previously inaccessible region of the energy landscape. The result of this method is the system has overcome large energy barriers and sampled large portions of the landscape, which is considered comparable to macroscopically long time dynamics, especially compared to the timescale of molecular dynamics.

As mentioned above, $\mathbf{r}_{\min}^{\alpha}$ is a minimum on the Φ-space potential energy landscape, but not necessarily on the original energy landscape $U(\mathbf{r})$, or $\mathbf{r}_{\min}$. In a simulation, many minimums on the Φ-space landscape may be encountered before a minimum on the original landscape is sampled. Particularly, multiple penalties are generally required to overcome a barrier on the inherent landscape and sample a new minimum. After energy minimization is performed, the force on the system, $\mathbf{F}(\mathbf{r})$, is nearly zero, however, the force of the original potential, $\mathbf{F}_{pp}(\mathbf{r})$, is not guaranteed to be non-zero. Instead, if $\mathbf{F}_{pp}(\mathbf{r})$ is zero and $\sum_{\alpha} \phi(\mathbf{r}, \mathbf{r}_{\min}^{\alpha})$ is zero, a new minimum has been sampled, otherwise, if $\mathbf{F}_{pp}(\mathbf{r})$ is not zero, a new minimum has not been sampled. Thus, the simulation can be analyzed to determine the series of basins and barriers sampled by the system.

As a result of the penalties being a function of the system configuration and not a collective variable, the energy landscape sampled is a function of the system configuration and is therefore a 3N dimensional energy landscape. Generally, advanced sampling methods have focused on sampling free energy landscapes of one or two collective variables. By sampling the 3N all atom energy landscape, we apply no a priori bias or assumptions about the system. However, as discussed briefly in Appendix A and in [5], there are

assumptions made by the height and width of the penalty function, and they determine the scale of the landscape sampled.

The structure of the method is shown in Figure A.2, adapted from [5].

2.3.2 Net center of mass translation and rotation removal

One caveat of penalizing the system configuration is that there are d redundancies in the system. Particularly, the system of equations for the system are not linearly independent, and there are d dependent equations in the system. This is evident through the fact that the system can minimize the penalty function, $\phi(\mathbf{r}, \mathbf{r}^{\alpha}_{\min})$, by merely center of mass translation. Intuitively, one can see that minimization of $\phi(\mathbf{r}, \mathbf{r}^{\alpha}_{\min})$ is easily achieved by adding 2σ to each atoms x, y, z, or a combination of the three coordinate. As a result, in order to remove this redundancy, the landscape needs to be reduced d degrees of freedom.

Thus, we modify the force of the system by removing the center of mass translation

$$\mathbf{F}_i = \mathbf{F}_i - m_i \mathbf{A} \tag{2.6}$$

where $\mathbf{A}$ is a three dimensional vector defined as

$$\mathbf{A} = \frac{1}{N} \sum_{i}^{N} \frac{\mathbf{F}_i}{m_i} \tag{2.7}$$

where m_i is the mass of atom i and $\mathbf{F}_i$ is the force vector of atom i. By removing this net force from the system, the system no longer translates and minimizes the penalty energy via internal rearrangements.

Further, not only can the system relax the added potential energy by center of mass translation, but also via center of mass rotation. More explicitly, the problem is

$$\sum_{i} (\mathbf{r}_i - \mathbf{r}_{\mathrm{nm}}) \times \mathbf{F}_i \neq 0 \tag{2.8}$$

Thus, we need a modified force that suffices the following

$$\sum_{i} (\mathbf{r}_i - \mathbf{r}_{\mathrm{nm}}) \times \mathbf{F}'_i \neq 0 \tag{2.9}$$

where

$$\mathbf{F}'_i = \mathbf{F}_i - \mathbf{F}_{T,i} \tag{2.10}$$

Thus we have

$$\sum_i (\mathbf{r}_i - \mathbf{r}_{\text{nm}} \times \mathbf{F}_i) = \mathbf{M}_{\text{net}} \tag{2.11}$$

where $\mathbf{M}_{\text{net}}$ is the net moment on the system and is equal to

$$\mathbf{M}_{\text{net}} = \mathbf{I}_{\text{total}} \overrightarrow{\omega} = \sum_i \mathbf{I}_i \overrightarrow{\omega} \tag{2.12}$$

From the equation before

$$\begin{aligned} \sum_i (\mathbf{r}_i - \mathbf{r}_{\text{nm}} \times \mathbf{F}'_i) &= \sum_i (\mathbf{r}_i - \mathbf{r}_{\text{nm}}) \times (\mathbf{F}_i - \mathbf{F}_{T,i}) \\ &= \sum_i \mathbf{I}_i \overrightarrow{\omega} - (\mathbf{r}_i - \mathbf{r}_{\text{nm}}) \times \mathbf{F}_{T,i} \end{aligned} \tag{2.13}$$

using

$$\mathbf{I}_i \overrightarrow{\omega} = ||\mathbf{r}_i||^2 \overrightarrow{\omega} - (\overrightarrow{\omega} \cdot \mathbf{r}_i)\mathbf{r}_i = (\mathbf{r}_i \times \overrightarrow{\omega}) \times \mathbf{r}_i \tag{2.14}$$

the equation becomes

$$\begin{aligned} \sum_i (\mathbf{r}_i - \mathbf{r}_{\text{nm}} \times \mathbf{F}'_i) &= \sum_i ((\mathbf{r}_i - \mathbf{r}_{\text{nm}}) \times \overrightarrow{\omega}) \times (\mathbf{r}_i - \mathbf{r}_{\text{nm}}) + \mathbf{F}_{T,i} \times (\mathbf{r}_i - \mathbf{r}_{\text{nm}}) \\ &= \sum_i ((\mathbf{r}_i - \mathbf{r}_{\text{nm}}) \times \overrightarrow{\omega} + \mathbf{F}_{T,i}) \times (\mathbf{r}_i - \mathbf{r}_{\text{nm}}) \end{aligned} \tag{2.15}$$

by imposing

$$(\mathbf{r}_i - \mathbf{r}_{\text{nm}}) \times \overrightarrow{\omega} + \mathbf{F}_{T,i} = 0 \mathbf{F}_{T,i} = \overrightarrow{\omega} \times (\mathbf{r}_i - \mathbf{r}_{\text{nm}}) \tag{2.16}$$

we get the equation for the force modifier as

$$\mathbf{F}_{T,i} = (\mathbf{I}_{\text{total}}^{-1} \mathbf{M}_{\text{net}}) \times (\mathbf{r}_i - \mathbf{r}_{\text{nm}}) \tag{2.17}$$

Center of mass rotations were not evident in the nucleation simulations, but was a problem when studying molecular systems. Thus, this additional restraint on the method has been introduced to the formulation.

2.3.3 Bond Order Parameter

In this thesis, the Bond Order Parameter will be used to measure the local structure of the atoms in the system [51], which is a popular quantity for measuring medium and short range order. The bond order parameter for individual atoms, q_l, measures the structure of an atom based on the arrangement of the local atoms. Whereas, Q_l, the system wide bond order parameter, is a measure of structure based on all of the atoms, and is equivalent to q_l averaged over all the atoms in the system [1]. Here, l is the order of the bond order parameter, and typical values of this are 4 and 6 [51]. To increase the accuracy of the bond order parameter for distinguishing atoms in the liquid and crystal phase, $\bar{q}_l$ averages q_l over the neighboring atoms to provide a more accurate measure of the structure of an atom [51]. While not a experimentally determinable quantity, the bond order parameter is a very successful quantity for measuring phases in a molecular system. The bond order parameter per atom is defined as

$$q_l(i,t) = \sqrt{\frac{4\pi}{2l+1}\sum_{m=-l}^{l}|q_{lm}(i,t)^2|} \tag{2.18}$$

where i is the atom number, t is the time, and

$$q_{lm}(i,t) = \frac{1}{N(i)}\sum_{j=1}^{N(i)} Y_{lm}(\hat{r}_{ij}(t)) \tag{2.19}$$

m ranges from $-l$ to l, $N(i)$ is the number of nearest neighbors around atom i, and Y_{lm} is the spherical harmonic of order l and m, and $\hat{r}_{ij}$ is the unit vector between atom i and j. The unit vector is converted to spherical coordinates, which are required for the spherical harmonics functions. The full system bond order parameter of the system is defined as

$$Q_l(t) = \sqrt{\frac{4\pi}{2l+1}\sum_{m=-l}^{l}|Q_{lm}(t)^2|} \tag{2.20}$$

where

$$Q_{lm}(t) = \frac{\sum_{i=1}^{N} N(i) q_{lm}(i,t)}{\sum_{i=1}^{N} N(i)} \tag{2.21}$$

and N is the number of atoms in the system. The nearest neighbor averaged bond order parameter is defined as

$$\bar{q}_l(i,t) = \sqrt{\frac{4\pi}{2l+1}\sum_{m=-l}^{l}|\bar{q}_{lm}(i,t)^2|} \tag{2.22}$$

Table 2.1: Mean values for the bond orientational order parameters for several crystal structures for a monoatomic Lennard-Jones liquid [1, 2].

	Q_4	Q_6	q_4	$\bar{q}_4$	q_6	$\bar{q}_6$
BCC	.0820	.5008	.0899	.0334	.4405	.4080
FCC	.1909	.5745	.1709	.1582	.5073	.4914
HCP	.0972	.4848	.1079	.0841	.4454	.4218
liq	.0000	.0000	.1090	.0312	.3601	.1620

where

$$\bar{q}_{lm}(i,t) = \frac{1}{N(i)} \sum_{j=0}^{N(i)} q_{lm}(j,t) \tag{2.23}$$

The nearest neighbors of an atom are defined as the atoms within a cutoff distance of a respective atom, which is typically determined to be the distance of the first peak of the pair distribution function. The bond order parameter was also calculated by LiquidLib [52] for this work.

2.4 Classical Nucleation Theory Literature Review

One quintessential rare event phenomena of great interest is phase transitions, which are driven by atomic scale dynamics but can require large timescales to occur depending on the temperature and system size [53, 54]. However, despite large interest in the studying nucleation and crystal growth, a definitive method to study nucleation computationally or experimentally is difficult to conceive due to the time and length scales of nucleation and crystal growth [55]. To understand phase behavior, classical nucleation theory has been developed, in which nucleation is theorized as a free energy barrier separating the metastable phase and the stable phase [56].

Figure 2.2 shows a schematic drawing of the CNT framework [56, 57]. The figure shows that the barrier separates the two phases, the left side of the barrier is the metastable phase and the right side of the barrier is the stable phase [56, 57]. The top of the barrier, an unstable state, is depicted as have a nucleus of the new phase existing in a system of the metastable phase. In the absence of surfaces and impurities, a system will develop nuclei of the stable phase from density fluctuations [56, 57]. If the nucleus is as large as the critical nucleus size, the system will transition from the metastable phase to the stable phase from the nucleus growing throughout the system. However, if the site is smaller than the critical nucleus, the nucleus will collapse back to the metastable phase. In this chapter, the goal is to use all-atom Metadynamics to predict the critical nucleus size using classical nucleation theory and the sampled energy landscape from the simulation.

In classical nucleation theory, there is a repulsive energy preventing the transition from the metastable

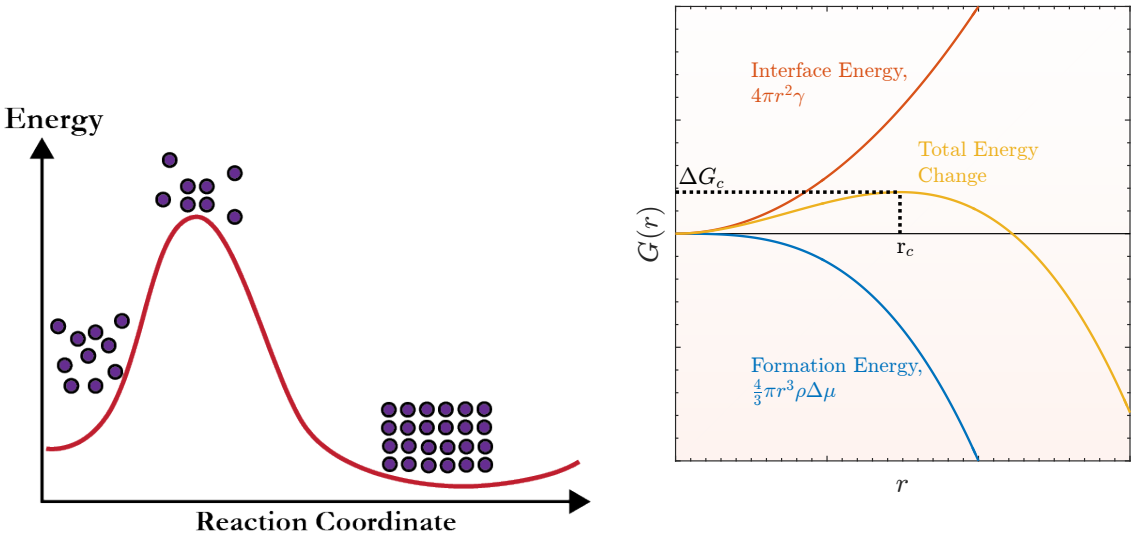

Figure 2.2: Left panel shows a schematic image of the classical nucleation theory, in which nucleation is a result of a single free energy barrier based on a single reaction coordinate, generally considered to be the number of atoms in the new phase nucleus. Right panel shows the calculation of the free energy barrier in classical nucleation theory as a function of the nucleus radius. Adapted from [5]

state to the stable state, caused by the creation of an interface between the two phases [57]. This repulsive energy can be determined by computing the change in the free energy as a function in the change of the area of the interface between the two phases, which is equivalent to

$$\Delta G_i = \frac{\partial G}{\partial A}\Delta A = A\gamma \tag{2.24}$$

where A is the surface area of the nucleation site, and γ is the surface tension of the liquid. This equation holds in the macroscopic picture in which an interface between two phases has a defined surface tension. If the nucleus site is assumed large enough that a defined surface tension is calculable, the repulsive energy takes the above form.

Conversely, the formation of a stable phase results in a decrease of the free energy of a system. The decrease in energy can be computed from the change in free energy as a function of the change in number of stable phase atoms, or $\partial G/\partial n$. This energy change can be determined from the chemical potential of the two phases and the number of atoms in the stable phase [57], or equivalently

$$\Delta G_f = V\rho\Delta\mu \tag{2.25}$$

where μ is the chemical potential, V is the volume of the nucleation site, ρ is the atomic density, and $\Delta\mu$ is the difference in the chemical potential defined as

$$\Delta\mu = \mu_{new} - \mu_{old} \tag{2.26}$$

where *new* and *old* indicate the metastable phase and the stable phase, respectively.

Generally, the nucleus site is assumed perfectly spherical, which results in

$$\begin{aligned} A &= 4\pi r^2 \\ V &= \frac{4}{3}\pi r^3 \end{aligned} \tag{2.27}$$

where r is the radius of the nucleation site [57]. Thus, the free energy barrier of nucleation as a function of nucleation site radius is determined by the following equation

$$\Delta G(r) = \Delta G_f(r) + \Delta G_i(r) = \frac{4}{3}\pi r^3 \rho \Delta\mu + 4\pi r^2 \gamma \tag{2.28}$$

This is pictorially displayed in Figure 2.2. The goal of this chapter is to compare this estimate to the free energy barrier with a computation of the barrier from the potential energy landscape sampled from all-atom Metadynamics

The critical radius can simply be calculated by

$$\left.\frac{d\Delta G(r)}{dr}\right|_{r=r_c} = 4\pi\rho\Delta\mu r_c^2 + 8\pi\gamma r_c = 0 \tag{2.29}$$

Solving this for r_c, results in

$$r_c = -\frac{2\gamma}{\rho\Delta\mu} = -\frac{2\gamma v}{\Delta\mu} \tag{2.30}$$

where v is the atomic specific volume [58].

2.4.1 Classical Nucleation Theory in Practice

In order to utilize the above derivation of the classical nucleation theory, an estimate of the nucleus size is needed. One highly successful method to estimate the nucleation site size is the coined embryo method, in which an MD simulation is initialized with a nucleus of the stable phase [59][60]. If the nucleus grows in the simulation, the nucleus is larger than the critical size, and vice versa if the nucleus shrinks [59][60]. By

varying the initial nucleus size, the critical nucleus size can be estimated. However, while a novel approach, the method assumes the nucleus to be perfectly ordered and perfectly spherical, which will be analyzed later from the all-atom Metadynamics simulation.

While Equation 2.24 is considered to be accurate, the general consensus is the assumption that the nucleus site is perfectly spherical and the derivations thereafter do not hold. Thus, there are two major sources of error, the assumption that the area is that of a sphere and the calculation on the surface tension. First, recent work has shown that the area of a critical nucleus site is highly non-spherical. Second, the value of the surface tension generally used is computed between a flat interface between a perfect crystal phase and a liquid phase, despite work indicating the outer layers of the critical nucleus may exhibit low order when compared to the center of the nucleus or a perfect structure. While difficult to completely separate these two sources of error or approximate which source has a larger effect, we can conclude both are potential sources of error in the computation of the nucleation rate. In the following sections, we shall show that indeed these assumptions hold poorly and propose an alternative approach for computing the interface energy for the critical nucleus.

2.5 Nucleation and Crystal Growth of Model System

Previously, we applied our all-atom Metadynamics method to a model liquid argon system based on the Lennard-Jones potential, in order to sample a trajectory along the energy landscape from a amorphous liquid phase to a crystal phase for two different densities [5]. The Lennard-Jones potential was chosen for its simplicity and ease of application [61]. Therein, we showed all-atom Metadynamics is able to directly sample an atomic trajectory of the nucleation and crystal growth process [5]. In this section, we first reintroduce the simulation performed, before performing further analysis from the original report to show how to approximate the critical nuclei from a all-atom Metadynamics sampled energy landscape.

In this thesis, we focus on the high density system previously simulated, with a density of 1.25 in Lennard-Jones unites. The simulation contained 864 argon atoms, and used the argon parameters for the Lennard-Jones model, σ of 3.40 Å and ϵ of 0.9977. For the all-atom Metadynamics simulation, the height of the penalty function was 1 kJ/mol, estimated from the depth of the Lennard-Jones potential, and the width squared was 0.1 nm^2, estimated roughly from the pair distribution function peak [62].

Figure 3.7 shows the pair potential and the key features for Lennard-Jones model, which is explicitly defined as

$$U(r) = 4\epsilon \left[\left(\frac{\sigma}{r}\right)^{12} - \left(\frac{\sigma}{r}\right)^{6} \right] \tag{2.31}$$

where U is the potential, r is the distance between two atoms centers, ϵ is the strength of the interaction between two atoms, and σ is the effective "diameter" of the atom. The Lennard-Jones potential was chosen as it is known to crystallize to an FCC crystal, which can be easily distinguished with $\bar{q}_6$ in the simulation.

The number of atoms was created such that in the crystal state, an unit cell is replicated six times in each direction. Thus, the number of atoms is equal to 4×6^3, or 864 atoms with a fixed box length of 3.0, this results in a density of 1.25 in Lennard-Jones units. The system was generated with a random configuration of atoms, and then, underwent energy minimization. An NVT simulation was then performed to equilibrate the system. The NVT simulation was 100 ps with a 1 fs time step at a fixed temperature of 120 K, well above the freezing temperature. Further simulation details are contained in [5].

2.5.1 Nucleation and Crystallization from All-Atom Metadynamics

The all-atom Metadynamics simulation of the Lennard-Jones system is summarized in Figure 2.3. The figure shows the real space visualization of the system at four critical points in the simulation. The atoms in the figures are colored by the bond order parameter. The energy landscape sampled in the simulation and where the four critical points occurred are shown as well. The insets of the figures show the computed diffraction pattern for the system.

Figure 2.3 shows that the system begins in an amorphous liquid configuration, indicated by the diffraction pattern's rings and the atoms being all blue. As the penalties are applied, the system rearranges into a pre-nucleated liquid. In this state, there are a select few atoms with medium to low order values, which is also shown by the change of the diffraction pattern. Next, the system undergoes rearrangement, and nucleated sites form in the system, shown by the diffraction pattern and the emergence of regions of high and medium order atoms. Closer analysis of this state shows that the regions of nucleation are highly non-spherical as is generally assumed for classical nucleation theory. Further, these regions show that they exhibit bond order parameter values below that of a perfect crystal. In fact, they also have regions of medium order, which has been predicted by others [63]. As a result, this questions the ability to use the surface tension to compute the free energy barrier, as the surface tension is generally computed between two flat interfaces of perfect order. Others have suggested that if the surface tension term were perfectly calculable, this estimate would still hold, however, given the distribution of ordered values and shape of the nucleation site, exact calculation of this term is difficult, as was discussed by others as well [64]. Finally, the simulation terminates with the system entering a perfect crystal form.

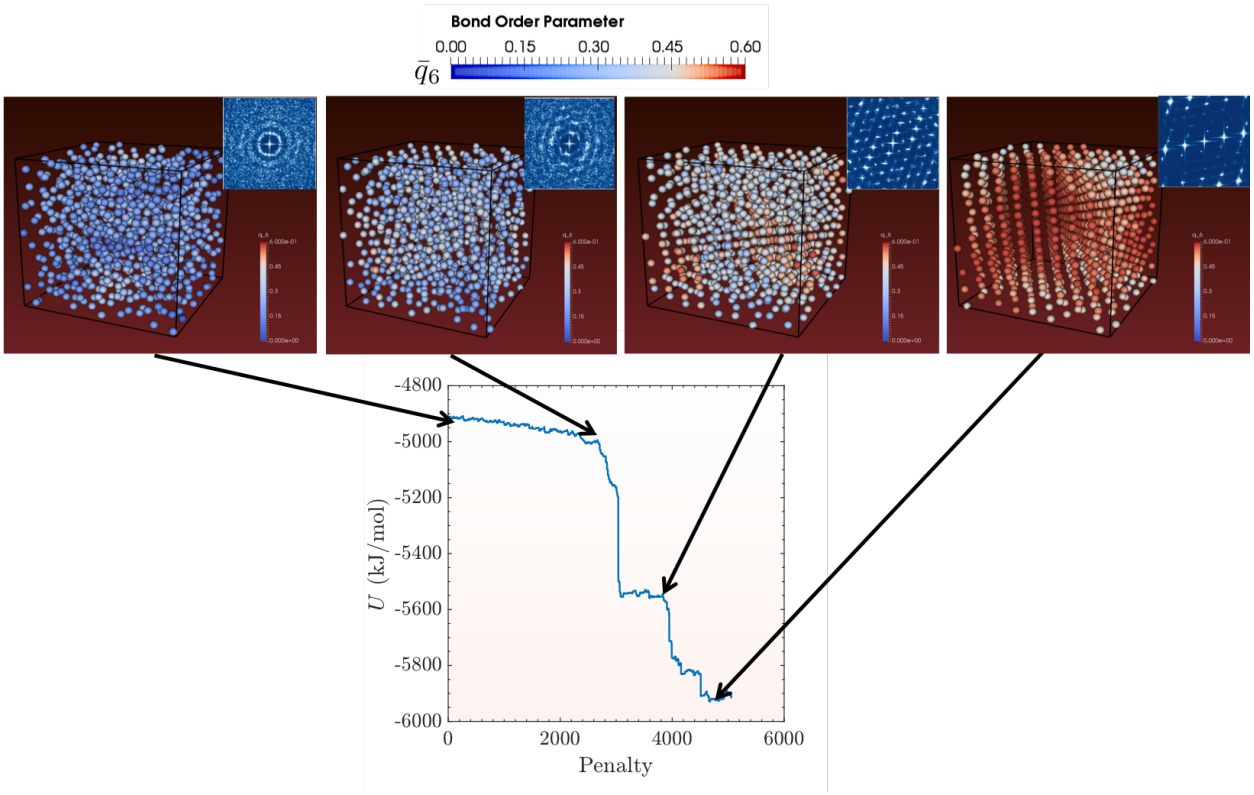

Figure 2.3: Results of the all-atom Metadynamics simulation of nucleation and crystal growth of a model liquid. The top panel shows the $\bar{q}_6$ values, which are used to color the atoms in the middle four panels. The middle four panels show the real space visualization of the system at various points along the sampled energy landscape. The atoms are colored by $\bar{q}_6$, with blue representing a disordered state and red representing an ordered state. The bottom panel shows the sampled energy landscape from the all-atom Metadynamics simulation as a function of the applied penalty function, which is an arbitrary parameter. From the left to the right panel, as an increasing number of penalties are applied, the system evolves from an amorphous liquid, to a pre-nucleated liquid, to a nucleated system, to an FCC crystal. The insets of the real space visualizations show the simulated diffraction pattern of the system.

2.5.2 Critical Nuclei Calculation

The goal of most studies of nucleation is to determine the critical nuclei for nucleation, generally estimating the size and shape of the nuclei. As discussed previously, the nuclei is assumed in many simulations to be perfectly spherical and to be in the final crystalline phase. In this section, the critical nuclei size is estimated from the sampled energy landscape, without assumptions about shape or structure.

In Figure 2.4, the classical nucleation theory lines are computed from the following equations. The repulsive energy from the surface interactions is computed as

$$\Delta G_{\text{repulsive}} = 4\pi r^2 \gamma \tag{2.32}$$

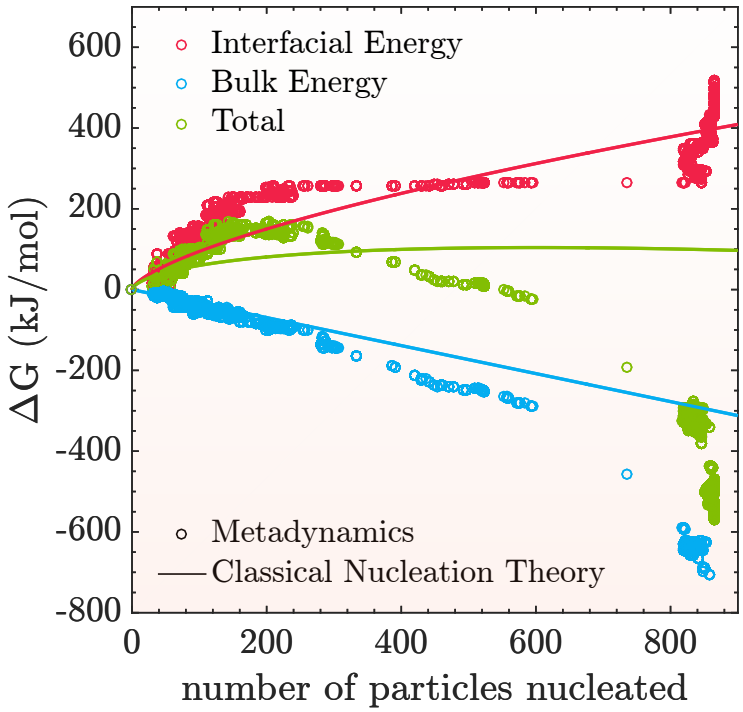

Figure 2.4: Comparison between the energy barrier computed from classical nucleation theory and from the energy landscape sampled by all-atom Metadynamics The smooth lines are computed with classical nucleation theory. The open circles are computed from the all-atom Metadynamics simulation and the sampled energy landscape.

where γ is equal to 3.02 in reduced units obtained from [54], and r is also in reduced units, shown as a red line in Figure 2.4. For reference, γ is generally computed by running a simulation with two phases, one liquid and one FCC crystal, and calculating the surface tension between the two flat interfaces of the two [65, 62, 66]. The energy released from formation is computed as

$$\Delta G_{\text{Bulk Energy}} = -\frac{4}{3}\pi r^3 n_s \Delta\mu \tag{2.33}$$

where μ is equal to 0.26 in reduced units obtained from [54], and n_s is one for this simulation, shown as the blue line in Figure 2.4. The number of particles in the nucleation site is computed from the radius of the nuclei site.

To compare with classical nucleation theory, the same two terms will be computed from the energy

landscape. Here, we propose computing the energy released from formation as

$$\Delta G_{\text{Bulk Energy}}(n) = E_{\text{nucleated configuration}}(n) - E_{\text{liquid configuration}} \tag{2.34}$$

where n is the number of nucleated particles. The repulsive energy for the formation of a nucleated site is computed by

$$\Delta G_{\text{repulsive}}(n) = \sum_{\text{barriers}} \Delta E_{\text{barrier}}(n) \tag{2.35}$$

where $\sum_{\text{barriers}}$ is the summation of the energy barriers from the liquid phase to the configuration with n nucleated particles, shown as open points on Figure 2.4. Generally, the repulsive term is determined as the work required to form the nucleus site. Here, we assume that the barriers overcome from the liquid phase to the current phase is equivalent to the work required to create the current phase.

Further, to determine the number of nucleated particles in a given configuration, the $\bar{q}_6$ of the particles is considered. If the bond order parameter is greater than the cut-off value of .35, the particle is considered to be in the crystal phase. The value of .35 was chosen because $\bar{q}_6 = .35$ is a good divider between the distribution of liquid values and the distribution of FCC values of the BOP.

Figure 2.4 shows the comparison between classical nucleation theory and all-atom Metadynamics approximation of the critical nuclei for the system. As a note, in the figure, after around 500 particles, the figure shows the all-atom Metadynamics values diverge, this is due to the system becoming majoritively in the crystal phase. the major difference in this figure is the location of the maximum for the energy barrier computed. From the classical nucleation values used, the estimated critical nucleus is around 652 particles, however, from all-atom Metadynamics the critical size is estimated around 200 particles. As discussed prior, a major source of this difference is with all-atom Metadynamics no assumption about the shape is made. Further, as discussed in the last section, the nucleus was shown to have a fair number of low ordered particles and not be uniformly perfect FCC as is often assumed in estimates of the nucleus size, which could be a cause of error in the estimation of the surface tension term.

2.5.3 Discussion

By simulating nucleation and crystal growth with All-Atom Metadynamics, we assume that the system traversed the minimum energy path from the amorphous state to the near perfect crystal state. As a result, unlike many other simulations, the simulation makes no a priori assumptions about the shape or structure of the nucleation state. However, one potential source of error in this analysis is performing the Metadynamics

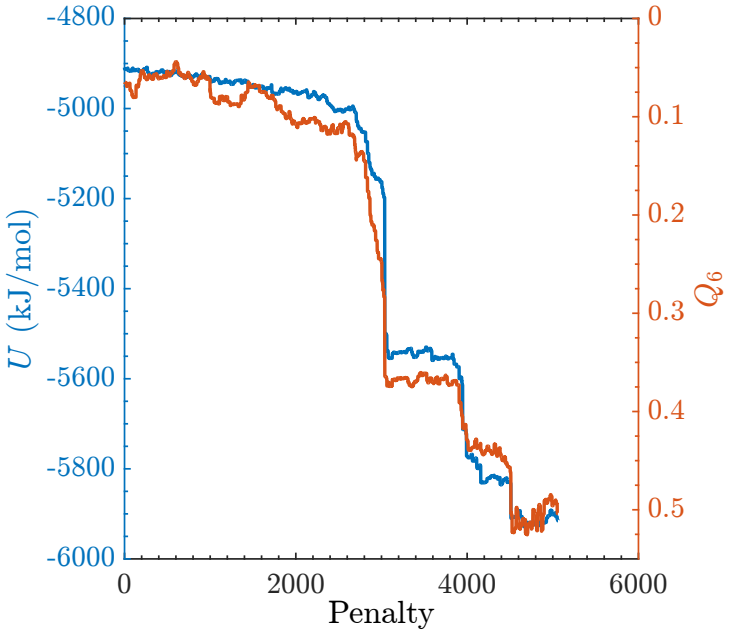

Figure 2.5: Potential energy landscape plotted as a function of penalty applied in blue as well as the Q_6 bond order parameter plotted as a function of the penalty applied in red

simulation as a constant density simulation. To be more accurate, a constant pressure simulation would be of interest.

2.6 Bond Order Parameter as an Appropriate Control Variable

Figure 2.5 shows the system wide bond order parameter, Q_6, plotted as a function of the penalty applied as well as the potential energy landscape plotted as a function of the penalty applied. The figure shows that the structure of the system and the potential energy coincide with one another very well. The figure also shows that when the system is at high energy levels, the Q_6 shows the system is still in an amorphous state. After around 2000 penalties are applied, the system undergoes a large structural change and the potential energy decreases drastically. The Q_6 shows the system is in a mixed state of partially structured and partially unstructured at this point. Then around 4000 penalties, another structural change occurs and the energy decreases once more as the system becomes a perfect FCC crystal.

Figure 2.5 also shows the viability of the bond order parameter as a collective variable for describing the system. Other studies of nucleation and phase change with advanced sampling methods have used Q_4 and Q_6 as the two collective variables for the sampled free energy landscape. However, here we have made

no assumptions in the all-atom Metadynamics simulation, and confirmed after that even in an unbiased simulation, the system will evolve on a landscape that is describable by the bond order parameter. However, this does not imply that this is a strong quantity for all systems, particularly, for more complex liquids such as water. Thus, we still believe the best approach is to use all-atom all-atom Metadynamics and make no assumptions on the descriptive variables of the system, and analyze the sampled landscape to determine collective variables that describe the energy landscape.

2.7 Summary

Metadynamics over the last decade has become a popular method for sampling the free energy landscape of material systems unveiling novel insights to dozens of phenomena. In this chapter, the original Metadynamics method is extended to sample the potential energy landscape of a system by biasing all atoms in the system rather than collective variables assumed to represent the nature of the system. All-atom Metadynamics allows the sampling of the complete potential energy landscape by adding potential energy in the form of multi-variate Gaussians to the system, which drive the system to overcome the energy barriers preventing the long time scale dynamics of interest. In order to ensure the system minimizes the added penalty energy via molecular rearrangements, the center of mass translation and rotation must be removed from the system. While computing the entire potential energy landscape is computationally difficult, we assume the sampled trajectory along the landscape is statistically representative of the landscape and of the dynamic behavior of the system.

The method is demonstrated on a monoatomic Lennard-Jones system, which is a known FCC crystal former. During the Metadynamics simulation, the system evolves from an amorphous liquid state to a nearly perfect crystal FCC state, measured by the popular bond orientational order parameter. While the exact time scale of the system is never deduced from the simulation, we known from other work that the nucleation and crystallization of a system of this size would never occur in the timescale of a molecular dynamics simulation due to the extremely low probability of a nucleation site forming in this system. From the simulation, the nucleation site is shown to be non-spherical and to have lower order than a perfect state. Further, fringe layers between the nucleus site and the liquid state show even lower orders of structure. This confirms that the nucleus site cannot be assumed to be perfectly spherical or perfectly structured. Therefore, we propose an approach to computing the free energy barrier from the energy landscape rather than from the surface tension and the chemical potential difference. Lastly, the bond order parameter is shown to be a strong collective variable for computing the potential energy landscape. With this approach, we believe that

crystallization of complex systems can be studied in detail, including systems with multiple crystal phases such as water, which was partially shown in [5].

Metadynamics, and the extensions there after, despite providing novel insights to phenomena across several fields, does suffer computationally. Much of the work in this chapter was the basis of my master's work [5] and is a strong motivation for the work in the following chapters. As will be discussed in the next chapter thoroughly, we found in using all-atom Metadynamics that Metadynamics can be computationally cumbersome and as a result limits the amount of sampling of the landscape that can be performed. As a result, despite many efforts to improve on the algorithm to increase the computational speed, we found a new method, Ascent Dynamics, that sampled the aspects of interest of the landscape more intentionally desirable. In the next chapter, our new method Ascent Dynamics will be introduced.

Chapter 3

Varied Steepness Ascent Dynamics for Fast Energy Landscape Sampling

3.1 Introduction

In the previous chapter, the success of all-atom metadynamics to study nucleation and crystal growth in a model system was discussed, with further details in [5]. All-atom metadynamics has also been used to study a series of protein systems to probe the correlation between the folding time and the activation energy of the energy landscape. The method was also used to study various phenomena in porous molecular cage systems. Further, other research groups using the original and other versions of metadynamics and other biasing methods have found great success unveiling new phenomena in fields ranging from chemistry, material science, and biology on a plethora of material systems. However, despite the utility of this method in many fields and problems, one glaring drawback of the all-atom metadynamics method is the computational cost. While studying these range of problems, it was revealed that all-atom metadynamics grows in computational cost over the simulation. Every penalty applied to a simulation increases the computational cost by a factor N^2, where N is the number of atoms in the system (for versions that use reduced number of variables, N is the number of variables describing the energy landscape). This effect is shown in Figure 3.1.

Figure 3.1 shows the real time spent for minimization as a function of penalty applied to the simulation. The simulation was performed over 16 cores, so the computational time is equal to the real time multiplied by 16. The figure shows that the best case time spent linearly increases as the number of penalties is applied, but because minimization can often require additional steps to converge, often the time spent is higher than the ideal case. The resulting computational cost for all-atom Metadynamics per minimization step is

$$\mathcal{O}(N_p N^2) \tag{3.1}$$

where N_p is the number of penalties, and N is the number of atoms in the system. This is the result of imposing the history dependence of the Metadynamics method. As a result, for ever penalty, the method computes a N^2 operation to compute the distance between the current position and the location of the applied

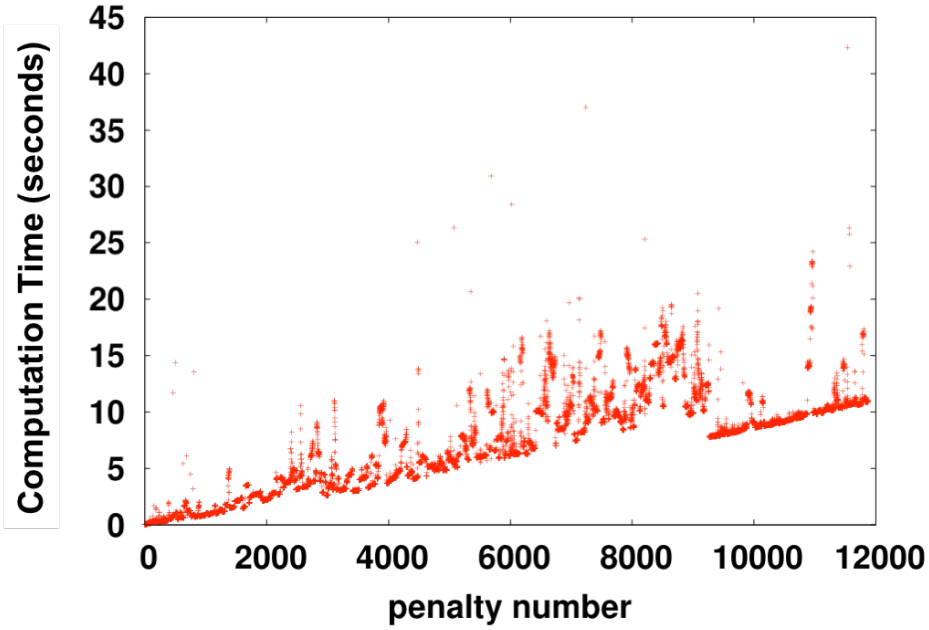

Figure 3.1: Real time spent per penalty for a metadynamics simulation of a binary Lennard-Jones system. The computational time is equal to the real time multiplied by 16.

penalty. As a result, once $N_p = N$, or N penalties have been applied to the system, the computational cost of this method is N^3, which for reference, molecular dynamics is N^2 without any kind of optimization.

Initial attempts to decrease the computational cost of this method were unsuccessful. First, we further parallelized the method. We tried improving the method by making more intelligent penalty functions, particularly, making the penalties more efficient by changing the shape or size to more efficiently fill the landscape. Others have developed methods to combine penalties that are similar in location and can be added to one another or use local information to vary the variance of the penalty function [67]. Others have proposed discretization of the landscape and look-up tables for the current value of the landscape as part of the implementation [42], and several other improvements have been proposed [68]. Lastly, we tried ideas of adding our intuition about the system into the algorithm to speed up convergence of the sampled landscape. However, the end result of all these ideas is to merely change the resulting slope of Figure 3.1, meaning, each idea decreases the slope of the figure but the complexity increases as more penalties are applied none the less.

Thus, we were motivated to develop a new method for sampling transition states and traversing along the energy landscape. This chapter is organized by first a review of existing methods that were used as a basis for the new method. Followed by a formulation and derivation of the new method. Lastly, verification and validation of the method is shown with model systems and a few methods for accelerating the method

are discussed.

3.2 Literature Review

As previously discussed briefly in the Chapter 1, the field of advanced sampling methods is rich with many different methods. Metadynamics belongs to the class of biasing methods. However, there are a many methods that belong to the surface walking class. Two advanced sampling methods that have found great success are the Activation Relaxation Technique and Gentlest Descent Dynamics. Both methods are surface walking methods.

3.2.1 Activation Relaxation Technique

Activation Relaxation Technique, or ART, is a surface walking method for calculating transition states [69, 44, 70, 71, 72]. The original authors were motivated to create a method for calculating transition states based on local information without increasing the computational complexity of the simulation, meaning without computing the second order derivative Hessian matrix. The motivation being that numerical calculation of the Hessian matrix is a very expensive computation to do every step. Thus, the goal was to determine a method for approximating the principle direction of the energy landscape of a current configuration efficiently.

Thus, ART determined the following methodology [69, 44, 70, 71, 72]. The core equation of the method is

$$\mathbf{G}(\mathbf{r}) = \mathbf{F}(\mathbf{r}) - (1+\alpha)(\mathbf{F}(\mathbf{r}) \cdot \hat{\mathbf{r}})\hat{\mathbf{r}} \tag{3.2}$$

where α is a control parameter that determines stability of convergence, $\mathbf{G}$ is the modified force for the system, $\mathbf{F}$ is the original force of the system, and $\hat{\mathbf{r}}$ is the unit vector from the current configuration to the previous minimum configuration. Then, the system configuration is updated with

$$\mathbf{r}_i = \mathbf{r}_{i-1} - \delta\mathbf{G}(\mathbf{r}) \tag{3.3}$$

where δ is the step size for each iteration.

The idea behind this method is that at any given point the force can be decomposed into two components, one component is in the direction towards the nearest minimum and the other component is perpendicular to the direction towards the nearest minimum. Thus, if the force always points upwards along the gradient, then $\hat{\mathbf{r}}$ is an approximation to the direction of negative curvature at the current configuration [69, 44, 70, 71, 72].

As a quick example, if the force points in the direction towards the nearest minimum and $\alpha = 2$, then the

modified force with be the opposite of the force. The modified force will point away from the minimum and therefore be an uphill step on the landscape. In a less ideal scenario, $(1+\alpha)(\mathbf{F}(\mathbf{r})\cdot\hat{\mathbf{r}})\hat{\mathbf{r}}$ results in flipping the sign of the component of the force that points towards the minimum, while the sign of the component of the force that points perpendicular remains the same. Thus, the direction towards the minimum is maximized on the landscape, while the direction perpendicular is minimized.

While difficult to visualize, this method has been shown very successful at converging to transition states of simple landscapes. In particular, this method has been used for a range of problems including, defect dynamics, simple proteins, and others [44, 70, 71, 72]. In order to apply this method, the systems are often characterized by collective variables in order to simplify the free energy landscape.

However, the method has been shown to struggle with convergence due to the parameter α. Further, the method is limited to index-1 transitions due to the use of $\hat{\mathbf{r}}$. In order to sample higher order transition states, knowledge of higher order directions on the landscape would be required. For example, an equivalent of $\hat{\mathbf{r}}$ from the current position to the nearest index-1 saddle point.

3.2.2 Gentlest Ascent Dynamics

Gentlest Ascent Dynamics, or GAD, is another surface walking method for calculating transition states that built upon the formulation of previous methods such as Nudged Elastic Band, Transition Path Sampling, and Activation Relaxation Technique [45]. Whereas most other surface walking methods avoid computation of the Hessian matrix, GAD determined that the Hessian matrix was the only viable method for computing accurate and stable transition path ways. Some of the stability issues with ART arise from avoiding the Hessian matrix. Similar to ART, GAD attempts to calculate the lowest eigenvalue eigenvector, or the direction of lowest curvature, and remove the projection of this direction from the modified force for updating the position of the system. In GAD, the core equation becomes

$$\mathbf{F}'(\mathbf{r}) = \mathbf{F}(\mathbf{r}) - 2(\mathbf{F}(\mathbf{r})\cdot\mathbf{n})\mathbf{n} \tag{3.4}$$

where $\mathbf{n}$ is the lowest eigenvalue eigenvector of the Hessian matrix. The key difference between GAD and ART is that ART's $\hat{\mathbf{r}}$ is an approximation of the direction of lowest curvature at the current configuration whereas GAD's $\mathbf{n}$ is the exact calculation of the lowest direction of curvature. $\mathbf{n}$ is then calculated as

$$\mathbf{H}\mathbf{n} = \lambda_0\mathbf{n} \tag{3.5}$$

However, to avoid diagonalization of the Hessian matrix which is an expensive computation, GAD uses the following equation to approximate the value of $\mathbf{n}$

$$\mathbf{n}_i = \frac{\mathbf{H}\mathbf{n}_{i-1}}{\mathbf{n}_{i-1} \cdot \mathbf{H}\mathbf{n}_{i-1}} \tag{3.6}$$

Which can very easily be seen as a power iteration scheme for solving for the lowest eigenvalue eigenvector [73].

The overall method then uses a random vector at the minimum as an initial guess for the transition state. The configuration is then updated based on the modified force $\mathbf{F}'$. The new Hessian matrix is computed and used to update the value of $\mathbf{n}$. After several iterations of this, the value of $\mathbf{n}$ begins to converge to an accurate estimate of the lowest eigenvalue eigenvector. Thus, at this point GAD follows along the modified force based on the vector of lowest curvature until convergence to a transition state[45].

GAD has found success in being used for many problems including defect diffusion, protein folding and chemical transitions, and more. Particularly, GAD was initially shown to be effective on many two and three dimensional equations with stable saddle index-1 points [45]. Later, GAD was shown to effectively sample simple transition states in material systems with reduced Hessian matrices based on the region of interest in the system, such as vacancy diffusion [74]. Others then showed the success of the method on simple molecular systems with index-1 transition points based on collective variables [75, 76].

However, as the authors discuss, by power iterating to converge on the eigenvector, this method suffers from size scaling. The larger the order of the Hessian and the system size, the longer the method takes to converge on an accurate evaluation of the eigenvector. Further, similar to ART and most other surface walking methods, GAD is focused on a single lowest transition vector often characterized by using collective variables of the system.

A lot of further work focused on evaluating the strength of GAD on more mathematical examples [77, 78, 79, 80]. GAD was shown to not always take a direct route to the transition state, but can sometimes extend past the transition state and then take a down hill approach to the transition state [80]. Some work has focused on the stability of GAD as a saddle searching method [81]. These works focused on mathematical models and found that GAD can suffer from stability depending on the shape of the vector field of the saddle point, including problems with imaginary eigenvectors and eigenvalues. However, as a counter point, the types of saddles that stability issues have been found in are not likely to occur on a materials energy landscape.

Several attempts to improve on the original GAD method have been proposed in recent years. Partic-

ularly, some methods have attempted to further reduce the computational cost of GAD. One such method is the iterative minimization formulation, which uses intelligent algorithms to convert the transition state sampling into an optimization problem reducing the overall computational complexity [82]. Another such method is the "simplify" GAD which reduces the complexity of the transition state sampling by reducing the system of differential equations being solved from three to two[83]. Another improvement of GAD is the proposed MD-GAD, which combines the algorithm of GAD and molecular dynamics to add thermal energy to the method [45]

Other attempts to extend the original GAD method focused on increasing the order of the saddles sampled with GAD from index-1 to index-2 [84, 85]. However, at higher orders, the errors from approximating the directions of lowest curvature in GAD begins to increasingly affect the stability of the method. Leading one to need a "region of interest" for the method to be successful and often reports the method going in incorrect directions [85].

3.3 Varied Steepness Ascent Dynamics Formulation

In this section, we propose a new method for sampling the energy landscape.

3.3.1 Motivation

ART and GAD have shown great success as a advanced sampling method for simple landscapes. Systems that can be reduced to one or two simple collective variables are ideal for ART and GAD. However, when a system cannot be reduced to a few simple variables, ART and GAD focus on following only the lowest direction of curvature and thus only sample index-1 transition points. Further, as will be discussed later, merely following higher orders of curvature of the landscape are not sufficient for explaining more complex transitions in most systems. Instead, complex systems, like liquids, or systems without simple two dimensional landscapes, have been shown to exhibit transitions that are of higher order on the landscape not merely of higher magnitude, although the two are rather correlated [86, 87]. It has even been proposed that the fragile vs strong relationship in liquids is the result of respectively different transition state indexes as the liquids are cooled [88, 89]. Further, phase transitions, while index one transitions along a well defined collective variable, are likely not index 1 saddle points when a collective variable is unknown. Although, it has been proposed that higher order saddle points on the landscape are merely multiple independent index-1 saddle points superimposed resulting in a higher order saddle point [90]. Thus, as will be discussed further in this chapter, a method that samples transition states of arbitrary order is of interest for studying complex systems. Hence,

we introduce Ascent Dynamics, an advanced sampling method for transition states of arbitrary order and without the computational overhead of our previous Metadynamics method and without the stability issues of approximating the direction of lowest curvature.

3.3.2 Method Formulation

We have developed a method for effectively traversing the energy landscape of a system through a series of activation and relaxations. First, the method will be described abstractly, and then, the method will be described concretely through its mathematical formalism.

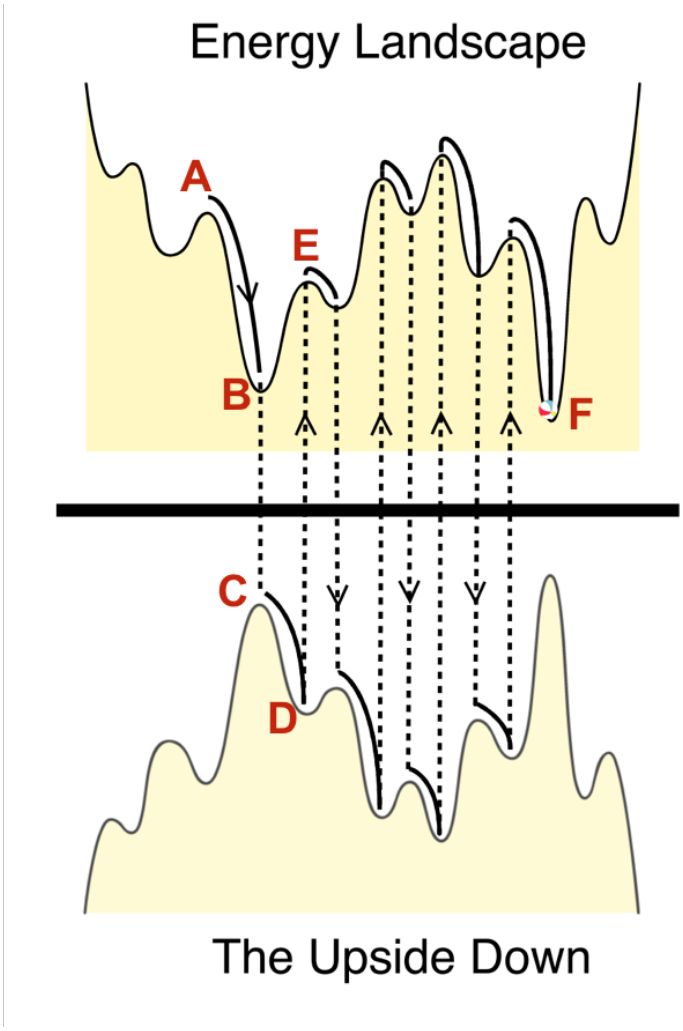

Figure 3.2: Schematic illustration of ascent dynamics on a model 1-D energy landscape. The system begins in an arbitrary configuration and is minimized to a local basin of attraction. From which, if the landscape is inverted, the minimum becomes a maximum and local maximums become minimums. Minimization on the inverted landscape results in convergence to a transition state. A-F shows a possible trajectory using this method.

Beginning with a system in any configuration, the system is relaxed to a local minimum of the energy landscape with steepest descent (Figure 1, A-B). To activate the system from a minimum, the landscape is reflected over a principle direction creating an upside down energy landscape (Figure 3.2, B-C). In the upside down, minimums become transition states, and transition states become basins of attraction. The system is then relaxed in the upside down from a transition state to a basin of attraction (Figure 3.2, C-D). In the original landscape, the system has traveled from a minimum to a transition state (Figure 3.2, D-E). Repeating this simple process in series, the system evolves over the energy landscape (Figure 3.2, E-F), providing a robust sample of transition states and metastable states.

A naïve approach to achieve the aforementioned method would be to flip the sign of the force during steepest descent, $\mathbf{F}' = -\mathbf{F}$, which would result in Figure 3.5 A. This approach works perfectly when the energy landscape is a function of one variable, as is often assumed for simple systems. In fact, much of the success of GAD and ART is by focusing on single variable landscapes, as this allows for a simple sign change to the force to sample the transition state of interest. However, for landscapes of more than two degrees of freedom, as many interesting systems exhibit, this approach no longer works. When the sign of the force is flipped, the system evolves to local maximums of the energy landscape. In an atomic system, the maximums of the potential energy landscape is two particles' centers colliding, an obvious nonphysical event, shown in Figure 3.3.

To avoid attraction to a global or local maximum on the energy landscape, we tried several ideas to discourage direct attraction between two particles, including setting minimum distances between two particles, decomposing the force based on atoms least likely to attract on top of one another, and many others. However, not only were many of these attempts ad hoc, but also unsuccessful.

However, a more physical solution is to decompose the energy landscape based on the principle components of the landscape, as shown in Figure 3.4. Figure 3.4 A shows that on a one dimensional landscape, because there is only one non-trivial eigenvector, the sign of the force can be changed and the transition states will be successfully sampled, as is the goal. Figure 3.4 B shows that on a two dimensional landscape, there are two non-trivial eigenvectors and one trivial eigenvector. In this vein, one can see schematically that following one of the eigenvectors leads to sampling the transition state of interest while following the other results in sampling a local maximum. Thus, we propose that if a method can be created to decompose the landscape based on it's principle components, the force can be decomposed based on these principle components. If the sign of only the lowest curvature principle components projections of the force are changed, then the system will sample the transition states of interest while avoiding maximum states characteristic of the higher curvature principle components.

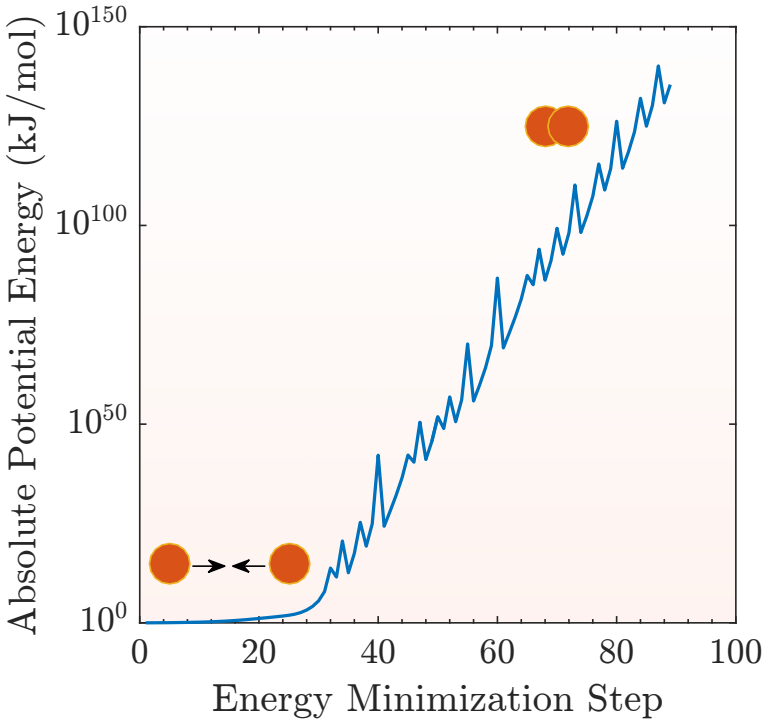

Figure 3.3: Energy landscape sampling from steepest ascent. The result of using $\mathbf{F}' = -\mathbf{F}$ is that two particles will converge on one another and result in unrealistic infinite system energy.

To achieve this effect of decomposing the force based on the landscape's information, the force is decomposed by principle components based on the full second derivative Hessian. The sign of the force is flipped in the directions of the lowest eigenvalued eigenvectors, while maintaining the sign of the remaining principle directions (Figure 3.2 B-C), mathematically, this takes the form

$$\mathbf{F}' = \mathbf{F} - 2\sum_{i=0}^{s}(\mathbf{F}\cdot\mathbf{e}_i)\mathbf{e}_i \tag{3.7}$$

The location of the system is then updated by

$$\mathbf{r}_{i+1} = \mathbf{r}_i + \delta_i \mathbf{F'}_i = \mathbf{r}_i + \delta_i \left[\mathbf{F} - 2\sum_{i=0}^{s}(\mathbf{F}\cdot\mathbf{e}_i)\mathbf{e}_i\right] \tag{3.8}$$

where δ_i is a chosen step length. Thus, the energy is minimized in the directions of the landscape that evolve to maximums and maximized in the directions of saddle points (Figure 3.2 C-D). As a result, the system evolves to transition points (Figure 3.2 D-E). The principle components of the force are determined

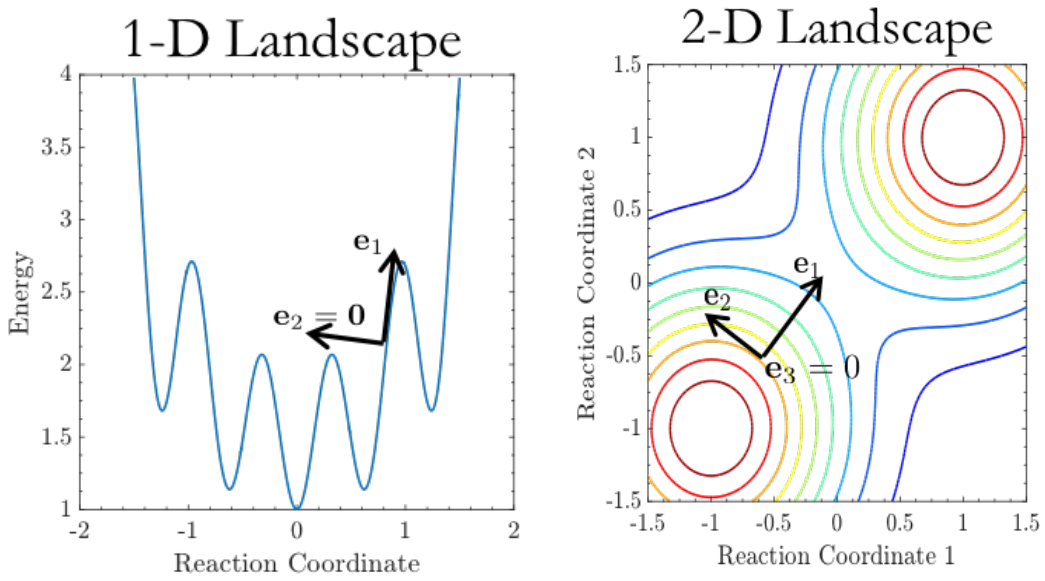

Figure 3.4: Left, a one dimensional energy landscape and the corresponding principle components. The non-trivial component is in the direction of the transition state, and the trivial component is tangential to the landscape. Right, a two dimensional energy landscape and the corresponding principle components. The first non-trivial component is in the direction of the transition state, the second non-trivial component is in the direction of the contour lines, and the trivial component is tangential to the landscape.

by solving

$$H\mathbf{e} = \lambda\mathbf{e} \tag{3.9}$$

where H is the Hessian of the system based on the current position. In equation 3.7, s is referred to as the steepness parameter. The steepness parameter determines the number of principle directions of the landscape will be inverted. The more directions included the steeper the path the system traverses on the energy landscape and the more complex the transition state becomes. When $s = 0$, equation 3.7 becomes steepest descent. When $s = 1$, equation 3.7 becomes an exact form of gentlest ascent dynamics or activation relaxation technique. When $s = dN$, where d is the dimension and N is the number of particles, equation 3.7 becomes steepest ascent and is equivalent to $\mathbf{F}' = -\mathbf{F}$, resulting in convergence to a local maximum on the energy landscape. For $1 \leq s \leq dN$, the system is performing ascent dynamics.

Relaxations from transition states to metastable states are performed with steepest descent (Figure 3.2 A-B)

$$\mathbf{r}_{i+1} = \mathbf{r}_i + \delta_i \mathbf{F}_i \tag{3.10}$$

where δ_i is a chosen step length. To increase performance for both ascents and descents, we use an adaptive step length. The step length is initially chosen conservatively to ensure stability of the first step. From

there, after each step, the step length for descents is adjusted following

$$\delta_i = \begin{cases} 1.2\delta_i, & \text{if } \mathrm{E}_i < \mathrm{E}_{i-1}. \\ 0.5\delta_i, & \text{if } \mathrm{E}_i \geq \mathrm{E}_{i-1}. \end{cases} \tag{3.11}$$

For ascents the step length is adjusted following

$$\delta_i = \begin{cases} 0.5\delta_i, & \text{if } \mathrm{E}_i \leq \mathrm{E}_{i-1}. \end{cases} \tag{3.12}$$

By adapting the step length, the relaxations and activations reach conversion more rapidly. Convergence to a transition state or a metastable state is determined by

$$\frac{|E_{i+1} - E_i|}{E_i} < \epsilon_E \quad \text{or} \quad \delta_i < \epsilon_\delta \tag{3.13}$$

where ϵ is a chosen threshold value.

By repeating this process, a series of transition states and metastable states are sampled (Figure 3.2 A-F).

As will be discussed more later, the true uniqueness of this method is the summation over multiple directions of curvature on the landscape in the modification of the force. This summation allows for convergence to higher order transition states which have been shown to dominate the dynamics of liquid systems.

3.3.3 Prefactor

In ART, the prefactor for the projection of the force in the modified force is $(1 + \alpha)$, where α is a control parameter that dictates the stability of the algorithm. In Equation 3.7, the prefactor is 2. The value of 2 was chosen so that in the modified force the projection of the force on the eigenvector is opposite that of in the original force. In this sense, if only looking in the direction of the eigenvector, Equation 3.7 results in Figure 3.2. However, during development of the method, we studied the effects of that prefactor. Lower and higher values of the prefactor resulted in slower convergence of the method to transition states. Lower values, but greater than 1, resulted in slower convergence due to the system following a less efficient path. Higher values resulted in slower convergence due to the system following paths that over commit to following the eigenvector and as a result do not minimize the force in the other eigenvectors.

Similarly, Ascent Dynamics follows the lowest s eigenvalue eigenvectors, because the largest eigenvalue eigenvectors represent pairs of atoms converging onto one another. We did also try studying if the prefactor

was less than 2 but greater than 1 if using the larger eigenvalue eigenvectors becomes viable. However, if the prefactor is anything greater than 1, pairs of atoms always converge onto one another, and if the prefactor is 1 or less than 1, the system remains in a local minimum.

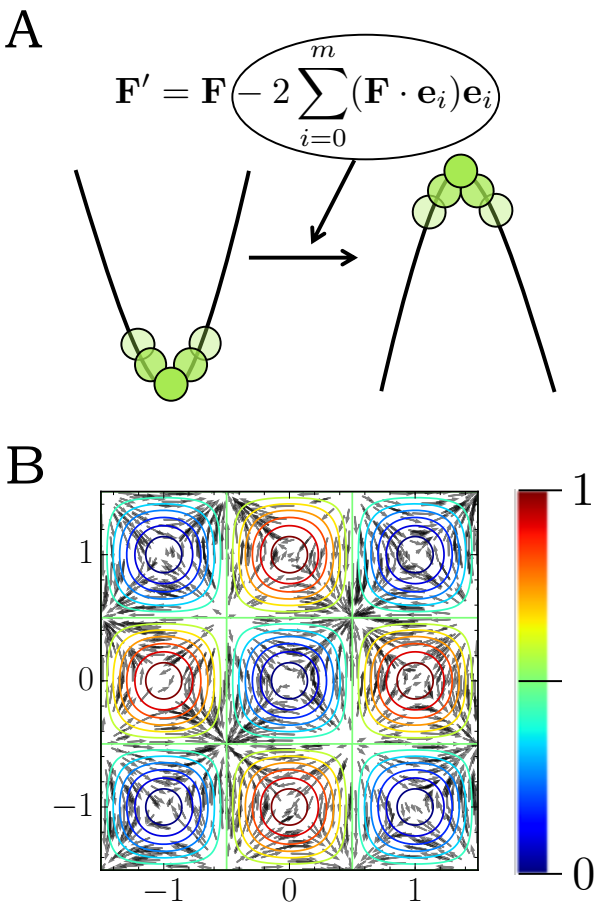

Figure 3.5: (A) The circled term in the ascent dynamics method results in an attractive basin of an energy minimum to be inverted to an activated mode. This results in the system evolving away from the initial position of the minimum. (B) Visualization of the modified force for $U(x, y) = -\cos(\pi x)\cos(\pi y)$. The vector field shows the path taken during a possible ascent dynamics simulation.

3.3.4 Minimum Steps

While in theory Ascent Dynamics should converge to the exact transition state and basin of attraction, in actuality, due to numerical errors and approximations, Ascent Dynamics never perfectly converges to the local configuration in which the forces are zero, or $\mathbf{F} = 0$. The addition of an adaptive step size for both minimization and for transition state sampling allows the method to converge extremely close to the true

solution.

As a result though, at the beginning of an ascent or descent, the magnitude of the force or the modified force is reasonable small, as regions near transition states and minimum states are defined by their low curvature. Thus, in these regions, the convergence criteria is already met generally, as the change in energy is rather small near this initial states. In order to escape these regions, a minimum number of steps is required at the start of an ascent or descent to ensure that the system has not been falsely determined as converged to the new sampled state. There is no easy determination of the minimum number of steps required, although, erring on the higher side only results in wasted iterations near the new sampled state, while erring on the low side results in convergence to an incorrect state. Generally, 500 for descents and ascents has resulted in no resampling of the same state while not adding unnecessary iterations.

3.3.5 State Perturbation

As previously mentioned, while in theory Ascent Dynamics should converge to the exact transition state and basin of attraction, in actuality, due to numerical errors and approximations, Ascent Dynamics never perfectly converges to the local configuration in which the forces are zero, or $\mathbf{F} = 0$. The addition of an adaptive step size for both minimization and for transition state sampling allows the method to converge extremely close to the true solution.

As a result, especially when sampling low order transition states (ex. 1 or 2), the system will converge to the same positions. In other words, after converging nearly to the transition state, the system will sit just short of the true transition state and thus have a force pointing back into the minimum it just escaped from. Thus, applying minimization at this point results in resampling of the previous minimum. Repeated iterations will result in resampling of the same minimum and transition state. This becomes increasingly unlikely to occur as the order of transitions being sampled is increased because of the increase in minimization pathways.

In order to prevent discourage resampling of the same points for low order sampling, small configuration perturbations can be utilized in the Ascent Dynamics method. More explicitly, after convergence to a transition state or minimum state, the following can be performed

$$\mathbf{r} = \mathbf{r} + \delta(1 + N(0, 0.1)) \tag{3.14}$$

where δ is the final value of the step size for the current iteration, and $N(0, 0.1)$ is the normal distribution with mean 0 and standard deviation 0.1. Because δ is small at convergence, this will slightly alter the

starting place for the next iteration. For example, using this perturbation after converging to a order 2 saddle configuration, the system will be modified slightly enough that minimization to a new minimum is more likely than without the perturbation.

3.4 Verification

To verify that following eigenvectors to local transition points works, we test the method aforementioned on several mathematical model problems. The first test case is defined by the interaction potential as a function of two variables

$$U(x, y) = -\cos(\pi x)\cos(\pi y) \tag{3.15}$$

This function was shown in the original GAD formulation as a verification set as well [45]. The resulting force of the system is

$$\mathbf{F}(x, y) = -\nabla U(x, y) = \begin{bmatrix} -\pi \sin(\pi x)\cos(\pi y) \\ -\pi \cos(\pi x)\sin(\pi y) \end{bmatrix} \tag{3.16}$$

with a Hessian of

$$H(x, y) = \pi^2 \begin{bmatrix} \cos(\pi x)\cos(\pi y) & -\sin(\pi x)\sin(\pi y) \\ -\sin(\pi x)\sin(\pi y) & \cos(\pi x)\cos(\pi y) \end{bmatrix} \tag{3.17}$$

The associated eigenvectors and eigenvalues of this model are

$$\mathbf{e} = \frac{1}{\sqrt{2}}[1, \pm 1] \tag{3.18}$$

$$\lambda = \pi^2 \left(\cos(\pi x)\cos(\pi y) \mp \sin(\pi x)\sin(\pi y)\right) \tag{3.19}$$

Choosing the first eigenvalue and eigenvector, λ_1 and $\mathbf{e}_1$, the modified force is

$$\mathbf{F}' = \pi[\cos(\pi x)\sin(\pi y), \sin(\pi x)\cos(\pi y)] \tag{3.20}$$

which corresponds to a modified potential, or an upside down potential of

$$U'(x, y) = -sin(\pi x)\sin(\pi y) \tag{3.21}$$

This modified force is shown in Figure 3.5 B. The original potential, $U(x, y)$ is plotted as a color map, and the modified force is overlaid as black arrows. Thus, if a system started near the minimum (0,0), following

the vector field results in convergence to the transition point at (0.5, 0.5). Similarly, following the vector field from any initial point in the range (0:1, 0:1) results in convergence to the transition point (0.5, 0.5).

The first model test case shows that following the modified force will indeed converge to a transition state. However, the model potential was highly symmetrical. Thus, test case two was designed to create a landscape with non-symmetrical basins of attraction to test if the method is biased towards transition states based on locality to the minimum. The potential is defined as

$$U(x, y) = \cos(\pi xy)\cos(\pi y) \tag{3.22}$$

The resulting force of the system is

$$\mathbf{F}(x, y) = \begin{bmatrix} \pi y \sin(\pi xy)\cos(\pi y) \\ \pi x \sin(\pi xy)\cos(\pi y) + \pi \cos(\pi xy)\sin(\pi y) \end{bmatrix} \tag{3.23}$$

with a Hessian of

$$H_{11}(x, y) = \pi^2 y^2 \cos(\pi xy)\cos(\pi y) \tag{3.24}$$

$$H_{12}(x, y) = -\pi \sin(\pi xy)\cos(\pi y) - \pi^2 xy \cos(\pi xy)\cos(\pi y) + \pi^2 y \sin(\pi xy)\sin(piy) \tag{3.25}$$

$$H_{21}(x, y) = -\pi \sin(\pi xy)\cos(\pi y) - \pi^2 xy \cos(\pi xy)\cos(\pi y) + \pi^2 y \sin(\pi xy)\sin(piy) \tag{3.26}$$

$$H_{22}(x, y) = -\pi^2 x^2 \cos(\pi xy)\cos(\pi y) + 2\pi^2 x \sin(\pi xy)\sin(\pi y) - \pi^2 \cos(\pi xy)\cos(\pi y) \tag{3.27}$$

The associated eigenvectors and eigenvalues of this model are not as simple as the previous case and are computed on the fly during the simulation.

The transition states, minimums, and maximums of the first two test cases were all respectively equal in value, which is not going to be true in a real system. Thus, test case three was designed to have transition states of different values to test if the ascent dynamics method is biased towards certain transition states based on value. The potential is defined as

$$U(x, y) = -\cos(\pi x)\cos(\pi y) + \frac{x}{2} \tag{3.28}$$

The resulting force of the system is

$$\mathbf{F}(x,y) = \begin{bmatrix} -\pi \sin(\pi x)\cos(\pi y) - \frac{1}{2} \\ -\pi \cos(\pi x)\sin(\pi y) \end{bmatrix} \tag{3.29}$$

with a Hessian of

$$H(x,y) = \pi^2 \begin{bmatrix} \cos(\pi x)\cos(\pi y) & -\sin(\pi x)\sin(\pi y) \\ -\sin(\pi x)\sin(\pi y) & \cos(\pi x)\cos(\pi y) \end{bmatrix} \tag{3.30}$$

The associated eigenvectors and eigenvalues of this model are not as simple as the previous case and are computed on the fly during the simulation.

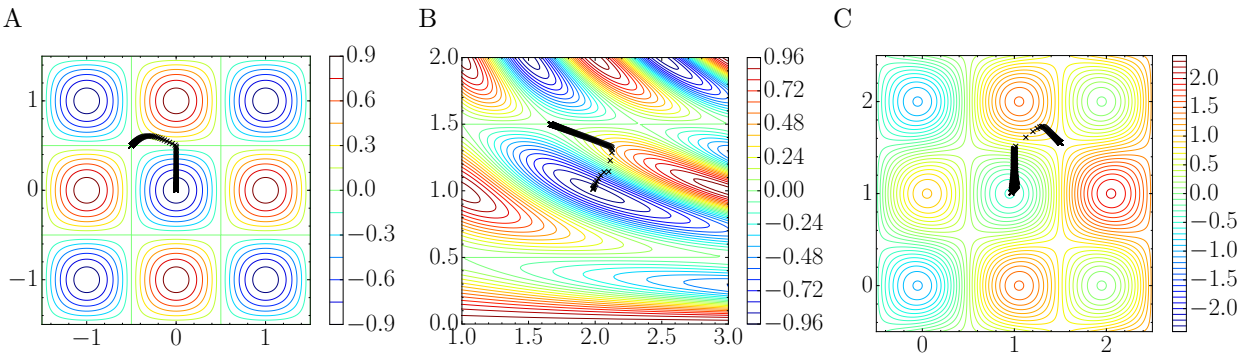

Figure 3.6: Sample trajectories, shown as black x's, using ascent dynamics are shown for three two dimensional test cases. (A) Trajectory along the potential $U(x,y) = -\cos(\pi x)\cos(\pi y)$. (B) Trajectory along the potential $U(x,y) = \cos(\pi xy)\cos(\pi y)$. (C) Trajectory along the potential $U(x,y) = -\cos(\pi x)\cos(\pi y) + \frac{x}{2}$

Figure 3.6 shows trajectories using ascent dynamics on the three model test cases aforementioned. Figure 3.6 A shows the trajectory of ascent dynamics for the first test case. The figure shows that by starting in the minimum at (0, 0), the system converges to the transition state at (-0.5, 0.5). This figure shows that ascent dynamics will converge to a local transition state. While only one trajectory is shown, the system is equally likely to converge to any of the surrounding transition states ($\pm$ 0.5, $\pm$ 0.5). Interestingly, the figure appears to show the system following the vector (0,1), despite the eigenvectors being (1,1) and (1,-1). Closer analysis shows that the system is actually following the eigenvectors, however, because the eigenvalues are equal in value from symmetry of the problem, the system is oscillating from one vector to the other. The result is the system following either (0,1) or (1,0) depending on how the eigenvectors are summed. In a real system, this is unlikely to occur as repeated eigenvalues are less likely to exist in a material system.

Figure 3.6 B shows the trajectory of ascent dynamics for the second test case. This test case was to study the method when applied to non-symmetrical basins of attraction. Of note, unlike the symmetric case, the

trajectory follows along the modified force more directly since the eigenvalues are not equal in value. While only one trajectory is shown, the system converged to all four surrounding transition states. The system showed preference to converge to the transition state that near (1.6, 1.5), as the method is biased towards transitions closer in distance from the original minimum. However, the system will also converge to the transition at (1.0, 1.5) as well.

Figure 3.6 C shows the trajectory of ascent dynamics for the third test case. This test case created to study the method when applied to a basin with local transitions of different value. The system converged to all four surrounding transition states. However, the system showed preference to the two lower valued transition states over the two higher valued transition states. Similar to Metadynamics, the probability of which transition state is sampled is based heavily on the initial position of the system near the minimum.

All three trajectories showed an interesting choice of the method to follow a path to values over the transition state value, nearing a local maximum, before changing directions and converging to a transition state. This occurs because the system follows paths to the contour line that is equal in value to the transition state, but, because the eigenvectors are not perpendicular with these contour lines, the system extends into regions of higher value before following a negative path to the transition state. This has been shown to occur in many minimum path following method for transition state sampling [80].

The previous test cases were all two dimensional models. Thus, test case four was designed to evaluate the method on a high dimensional model. The potential of the test case is

$$U(\mathbf{x}) = \Pi_{j=0}^{n} \cos(\pi x_j) \tag{3.31}$$

with the corresponding force in each direction

$$\mathbf{F}_i(\mathbf{x}) = \pi \sin(\pi x_i) \Pi_{j \neq i} \cos(\pi x_j) \tag{3.32}$$

and the associated Hessian matrix calculated from

$$H_{i,i}(\mathbf{x}) = -\pi^2 \Pi_{j=0}^{n} \cos(\pi x_j) \tag{3.33}$$

$$H_{i,k}(\mathbf{x}) = -\pi^2 \sin(\pi x_i) \sin(\pi x_k) \Pi_{j \neq i,k} \cos(\pi x_j) \tag{3.34}$$

this case is similar to that of test case 1, in that it is symmetrical in all directions, but can be evaluated on any dimension. First, the test of three dimensions (n = 3) was considered. The initial position of (-1, -1, -1)

was chosen, this is a minimum with value -1. When applying ascent dynamics on a single eigenvector, the transition state at (-.5, -1, -1) was initially sampled, but as was others such as (-1, .5, -1) etc. To evaluate the method when using a higher steepness parameter, ascent dynamics on two eigenvectors was applied, and the transition states of (-.5, -.5, -1), and it's associated permutations, was sampled. Thus, the method does indeed sample higher order transition states when increasing the steepness factor.

As a final note from these test cases, when ascent dynamics was applied with all eigenvectors used to modify the force, the system always converged to a local maximum. This tested that the code was accurately computing the eigenvectors and would reproduce $\mathbf{F} = -\mathbf{F}$ when used.

3.5 Validation

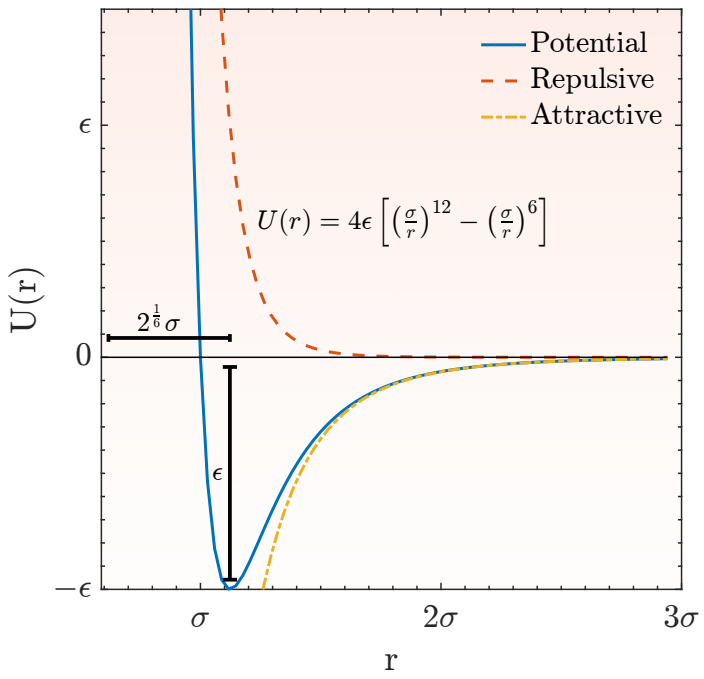

Figure 3.7: The Lennard-Jones potential is plotted as a function of atomic distance. The potential is also separated into the repulsive and attractive contributions. Key features of the potential such as the minimum energy and distance are shown.

To validate our implementation of the algorithm and the method itself on physical systems, we applied ascent dynamics to a simple vacancy diffusion problem in a 2-D Lennard-Jones system. The potential and

key features are shown in 3.7. The system potential is defined as

$$U(\mathbf{r}) = \sum_i \sum_{j \neq i} 4\epsilon \left[\left(\frac{\sigma}{r_{ij}} \right)^{12} - \left(\frac{\sigma}{r_{ij}} \right)^{6} \right] \tag{3.35}$$

with associated force on each particle

$$\mathbf{F}_i = -\sum_{j \neq i} 4\epsilon \left[\frac{12\sigma^{12}}{r_{ij}^{14}} - \frac{6\sigma^6}{r_{ij}^6} \right] \mathbf{r_{ij}} \tag{3.36}$$

and the Hessian is defined as

$$H(\mathbf{r}) = \begin{bmatrix} \frac{\partial^2 U}{\partial x_1 \partial x_1} & \frac{\partial^2 U}{\partial x_1 \partial y_1} & \cdots & \frac{\partial^2 U}{\partial x_1 \partial y_n} \\ \frac{\partial^2 U}{\partial y_1 \partial x_1} & \frac{\partial^2 U}{\partial y_1 \partial y_1} & \cdots & \frac{\partial^2 U}{\partial y_1 \partial y_n} \\ \vdots & \vdots & \ddots & \vdots \\ \frac{\partial^2 U}{\partial x_n \partial x_n} & \frac{\partial^2 U}{\partial x_n \partial y_1} & \cdots & \frac{\partial^2 U}{\partial y_n \partial y_n} \end{bmatrix} \tag{3.37}$$

where the tridiagonal terms are defined as

$$H_{i,i}(\mathbf{r}) = \frac{\partial^2 U(\mathbf{r})}{\partial x_i \partial x_i} = 4\epsilon \sum_{j \neq i} \left[\left(\frac{168\sigma^{12}}{r_{ij}^{16}} - \frac{48\sigma^6}{r_{ij}^8} \right) (x_j - x_i)^2 - \left(\frac{12\sigma^{12}}{r_{ij}^{14}} - \frac{6\sigma^6}{r_{ij}^6} \right) \right] \tag{3.38}$$

$$H_{i,i+1}(\mathbf{r}) = \frac{\partial^2 U(\mathbf{r})}{\partial x_i \partial y_i} = 4\epsilon \sum_{j \neq i} \left[\left(\frac{168\sigma^{12}}{r_{ij}^{16}} - \frac{48\sigma^6}{r_{ij}^8} \right) (x_j - x_i)(y_j - y_i) \right] \tag{3.39}$$

$$H_{i+1,i}(\mathbf{r}) = \frac{\partial^2 U(\mathbf{r})}{\partial y_i \partial x_i} = 4\epsilon \sum_{j \neq i} \left[\left(\frac{168\sigma^{12}}{r_{ij}^{16}} - \frac{48\sigma^6}{r_{ij}^8} \right) (x_j - x_i)(y_j - y_i) \right] \tag{3.40}$$

$$H_{i+1,i+1}(\mathbf{r}) = \frac{\partial^2 U(\mathbf{r})}{\partial y_i \partial y_i} = 4\epsilon \sum_{j \neq i} \left[\left(\frac{168\sigma^{12}}{r_{ij}^{16}} - \frac{48\sigma^6}{r_{ij}^8} \right) (y_j - y_i)^2 - \left(\frac{12\sigma^{12}}{r_{ij}^{14}} - \frac{6\sigma^6}{r_{ij}^6} \right) \right] \tag{3.41}$$

and the off tridiagonal terms are defined as

$$H_{i,j}(\mathbf{r}) = \frac{\partial^2 U(\mathbf{r})}{\partial x_i \partial x_j} = -4\epsilon \left[\left(\frac{168\sigma^{12}}{r_{ij}^{16}} - \frac{48\sigma^6}{r_{ij}^8} \right) (x_j - x_i)^2 - \left(\frac{12\sigma^{12}}{r_{ij}^{14}} - \frac{6\sigma^6}{r_{ij}^6} \right) \right] \tag{3.42}$$

$$H_{i,j+1}(\mathbf{r}) = \frac{\partial^2 U(\mathbf{r})}{\partial x_i \partial y_j} = -4\epsilon \left[\left(\frac{168\sigma^{12}}{r_{ij}^{16}} - \frac{48\sigma^6}{r_{ij}^8} \right) (x_j - x_i)(y_j - y_i) \right] \tag{3.43}$$

$$H_{i+1,j}(\mathbf{r}) = \frac{\partial^2 U(\mathbf{r})}{\partial y_i \partial x_j} = -4\epsilon \left[\left(\frac{168\sigma^{12}}{r_{ij}^{16}} - \frac{48\sigma^6}{r_{ij}^8} \right) (x_j - x_i)(y_j - y_i) \right] \tag{3.44}$$

$$H_{i+1,j+1}(\mathbf{r}) = \frac{\partial^2 U(\mathbf{r})}{\partial y_i \partial y_j} = -4\epsilon \left[\left(\frac{168\sigma^{12}}{r_{ij}^{16}} - \frac{48\sigma^6}{r_{ij}^8} \right) (y_j - y_i)^2 - \left(\frac{12\sigma^{12}}{r_{ij}^{14}} - \frac{6\sigma^6}{r_{ij}^6} \right) \right] \tag{3.45}$$

where i and j are even indices. Further, σ is the effective atom size and ϵ determines the strength of the interaction potential. The interaction potential is shown in Figure 3.7. The system studied is composed of 119 Lennard-Jones atoms in a 5 nm box. The system is initialized in it's closest packed configuration with a single vacancy. Figure 3.8 shows the initial configuration for the system.

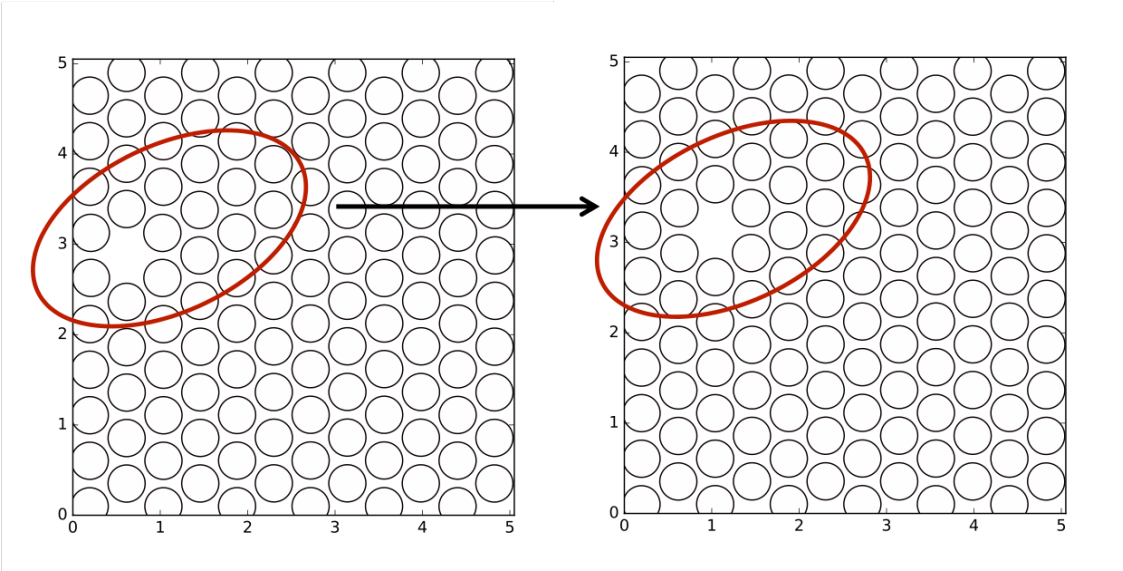

Figure 3.8: Ascent Dynamics of a 119 Lennard-Jones atoms system with a single vacancy in the system. The vacancy is highlighted by the red circle. From the left figure to the right figure, the vacancy is filled by an atom and emerges in the place of the atom.

Figure 3.8 shows the result of using Ascent Dynamics on a Lennard-Jones system with a single vacancy. In this case, the value of the steepness factor s in Ascent Dynamics was 4, where the first 3 lowest vectors represented trivial motion in the system. To validate that indeed the lowest 3 vectors represent trivial motion in the system, the modified force and eigenvector for the lowest 3 eigenvalues were plotted. The lowest eigenvalue eigenvector showed to be center of mass translation in the x-direction, the second lowest eigenvalue eigenvector showed to be center of mass translation in the y-direction, and the third lowest eigenvalue eigenvector showed to be center of mass rotation about the z-direction.

However, the projection of the force on these three lowest eigenvalue eigenvectors is zero, and thus does not result in any motion when applying Ascent Dynamics with s less than 4. Because the projection is zero onto the center of mass translation and rotation vectors, unlike with Metadynamics, there is no worry about needing to remove the center of mass translation or rotation for the position update. Whereas in Metadynamics, the bias force could be minimized via center of mass translation or rotation.

With s equal to 4, Figure 3.8 shows that Ascent Dynamics results in the sampling of a transition path

with the vacancy being filled with a neighbor atom. The transition state was sampled to have a transition energy of approximately 2.4 in reduced units. By comparison, in [91], the transition energy for a similar system was found to be approximately 2.69 in reduced units via a series of MD simulations. The difference in our solutions is assumed to be the result of slightly different configuration initializations of the two systems.

3.6 Steepness Factor

As mentioned previously, the methods that utilize surface walking techniques utilize the direction of lowest curvature and only sample transitions of index-1. Whereas, Ascent Dynamics follows directions of multiple lowest curvatures on a high dimensional landscape. Shown in the previous section, following the lowest direction of curvature is sufficient for simple problems such as vacancy diffusion. However, as many authors have found, transitions in complex systems such as liquids, proteins, and phase transitions are characterized by transitions that are of higher order than index-1.

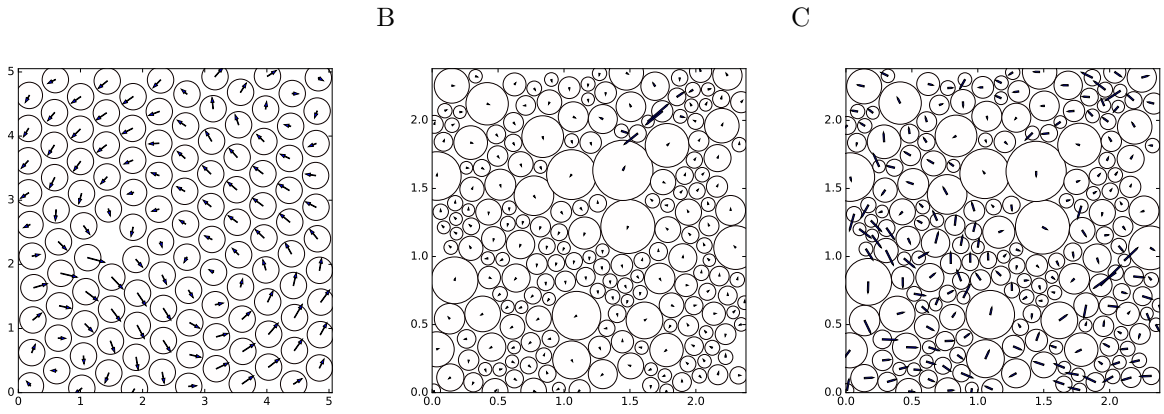

Figure 3.9: (A) Vector field of the modified force from Ascent Dynamics with $s = 4$ for a vacancy diffusion problem in a Lennard-Jones system. (B) Vector field for the modified force from Ascent Dynamics with $s = 4$ for a model liquid system. (C) Vector field for the modified force from Ascent Dynamics with $s = 15$ for a model liquid system.

To emphasize this, Figure 3.9 shows the need for sampling higher order transitions in Liquids. Figure 3.9 A shows the modified force from Ascent Dynamics with $s = 4$ for a vacancy diffusion problem. In this system, the transition state is easily definable as a index-1 transition, as the transition state can be defined by a single variable, the location of the vacancy. The figure shows the vector field of the system, and there is a clear collective behavior in the system. Similarly, when surface walker methods have been applied to proteins, the proteins are described by a couple collective variables As a result, previous methods have shown their success on problems that have evident index-1 transition states as they are sampling simple or reduced

energy landscapes.

However, liquids are difficult to describe with only a few collective variables, and many have found that transitions in liquids are of higher order than index-1. This is shown by Figure 3.9 B and C, which shows the vector field in a model liquid from Ascent Dynamics at $s = 4$ and $s = 15$. The system is a model liquid described more extensively in the next chapter. Figure 3.9 B shows that when only the lowest eigenvalue eigenvector is followed there is only 4 active atoms in the system. And in fact, a complete iteration of Ascent Dynamics with $s = 4$ for this system results in no transition state sampled. Figure 3.9 C shows that when $s = 15$ the vector field shows system wide dynamics. Further, with $s = 15$, Ascent Dynamics results in a complex transition sampled.

3.7 Finite Difference Hessian Evaluation

One method for enhancing the Ascent Dynamics method is using finite difference to update the values of the eigenvalues and eigenvectors being used rather than solving for them at each iteration. The motivation here is that computationally it is easier to parallelize and speed up vector math in most computer languages than it is to parallelize and speed up linear algebra algorithms for solving the eigenvalue and eigenvector problem of a matrix. Particularly, finite difference updates of the eigenvalues and eigenvectors is computationally less intensive than diagonalizing and solving the Hessian matrix at every configuration.

For this derivation, we will start with the eigenvalue problem

$$H\mathbf{e}_i = \lambda_i \mathbf{e}_i \tag{3.46}$$

and take the derivative based on configuration of the system

$$\dot{H}\mathbf{e}_i + H\dot{\mathbf{e}}_i = \dot{\lambda}_i \mathbf{e}_i + \lambda_i \dot{\mathbf{e}}_i \tag{3.47}$$

After each iteration of the configuration, we wish to maintain the following rule for all eigenvectors

$$||\mathbf{e}_i|| = 1 \tag{3.48}$$

In order to maintain this, we enforce

$$\dot{\mathbf{e}}_i \perp \mathbf{e}_i \quad \text{or} \quad (\dot{\mathbf{e}}_i, \mathbf{e}_i) = 0 \tag{3.49}$$

Therefore, we will take the right inner product of 3.47 with $\mathbf{e}_i$, resulting in

$$(\dot{H}\mathbf{e}_i, \mathbf{e}_i) + (H\dot{\mathbf{e}}_i, \mathbf{e}_i) = (\dot{\lambda}_i\mathbf{e}_i, \mathbf{e}_i) + (\lambda_i\dot{\mathbf{e}}_i, \mathbf{e}_i) \tag{3.50}$$

The following relationships will simplify the above equation

$$(H\dot{\mathbf{e}}_i, \mathbf{e}_i) = 0 \tag{3.51}$$

$$(\dot{\lambda}_i\mathbf{e}_i, \mathbf{e}_i) = \dot{\lambda}_i \tag{3.52}$$

$$(\lambda_i\dot{\mathbf{e}}_i, \mathbf{e}_i) = 0 \tag{3.53}$$

This results in the relation

$$\dot{\lambda}_i = (\dot{H}\mathbf{e}_i, \mathbf{e}_i) \tag{3.54}$$

Then, taking the right inner product of 3.47 with $\mathbf{e}_j$ leads to

$$(\dot{H}\mathbf{e}_i, \mathbf{e}_j) + (H\dot{\mathbf{e}}_i, \mathbf{e}_j) = (\dot{\lambda}_i\mathbf{e}_i, \mathbf{e}_j) + (\lambda_i\dot{\mathbf{e}}_i, \mathbf{e}_j) \tag{3.55}$$

We can use the following relationships

$$(H\dot{\mathbf{e}}_i, \mathbf{e}_j) = (\dot{\mathbf{e}}_i, H\mathbf{e}_j) \tag{3.56}$$

$$(\dot{\lambda}_i\mathbf{e}_i, \mathbf{e}_j) = 0 \tag{3.57}$$

The relationship $(H\dot{\mathbf{e}}_i, \mathbf{e}_j) = (\dot{\mathbf{e}}_i, H\mathbf{e}_j)$ holds because the Hessian is symmetrical. Using this relationship leads to

$$(\dot{H}\mathbf{e}_i, \mathbf{e}_j) + (\dot{\mathbf{e}}_i, H\mathbf{e}_j) = (\lambda_i\dot{\mathbf{e}}_i, \mathbf{e}_j) \tag{3.58}$$

$$(\dot{H}\mathbf{e}_i, \mathbf{e}_j) + (\dot{\mathbf{e}}_i, \lambda_j\mathbf{e}_j) = (\lambda_i\dot{\mathbf{e}}_i, \mathbf{e}_j) \tag{3.59}$$

$$(\dot{H}\mathbf{e}_i, \mathbf{e}_j) + \lambda_j(\dot{\mathbf{e}}_i, \mathbf{e}_j) = \lambda_i(\dot{\mathbf{e}}_i, \mathbf{e}_j) \tag{3.60}$$

$$(\dot{H}\mathbf{e}_i, \mathbf{e}_j) = (\lambda_i - \lambda_j)(\dot{\mathbf{e}}_i, \mathbf{e}_j) \tag{3.61}$$

Then, by taking the right inner product with $\mathbf{e}_j$ and summing over j, the following relation is arrived at

$$\dot{\mathbf{e}}_i = \sum_{j \neq i} \frac{1}{\lambda_i - \lambda_j}(\dot{H}\mathbf{e}_i, \mathbf{e}_j)\mathbf{e}_j \tag{3.62}$$

Lastly, because Ascent Dynamics updates the configuration of the system with small steps, we can calculate $\dot{H}$ as ΔH between each iteration. Thus with Equation 3.54 and 3.62, the change in the eigenvalues and eigenvectors can be calculated from the change in the Hessian matrix during each iteration. This scheme was tested on some of the test cases in the verification section, and shown to converge to the correct transition states.

However, there is some error that results from using this finite difference scheme and the true eigenvalues and eigenvectors at the current configuration. Thus, to use this scheme correctly in Ascent Dynamics, the algorithm will compute the true eigenvalues and eigenvectors at the first iteration. Then, use the finite difference scheme for M iterations. After M iterations, the true eigenvalues and eigenvectors should be computed again.

The benefit of using this scheme is that this scheme is easier to parallelize and vectorized than solving the eigenvalue problem for the Hessian matrix is at ever iteration. This can result in some improvement in speed and efficiency.

3.8 Ascent Dynamics Package

Ascent Dynamics was originally tested, developed, verified, and validated in Python 2, because Python allows for fast implementation of ideas, easy unit and functional test suite development, and an easy to use linear algebra package. However, after verification and validation of the Ascent Dynamics algorithm, the ability to run larger systems became of interest. As a result, the method was re-developed in Julia 1.0. Table 3.1 shows the net gains of producing the method in Julia over Python.

Further, the package has been developed with a test suite to maintain the development of the code. The package has been built with several potentials implemented including, Lennard-Jones (two and three dimensional), Binary Lennard-Jones, Polydisperse (two and three dimensional), and MB-water (a two dimensional water model).

Similar to the implementation of Metadynamics, the Ascent Dynamics has a large amount of small numbers added in ever iteration. As a result, consecutive runs from the same initial conditions can deviate from one another as the result of finite size additions causing different rounding errors in the computational methods. However, as with metadynamics, we assume that this results in a different trajectory along the landscape, but is still a statistically significant sampling of a trajectory along the landscape.

Table 3.1: Real time for computation of potential energy, forces, Hessian, and energy minimization for systems of 64, 200, and 500 atoms between Python, Julia, and Julia vectorized. The two times listed for Julia are the time when compiling the code and when the code is already compiled. Because Julia compiles the code just in time, the first use of any function is longer than future calls to the function.

Potential Energy

	N = 64	N = 200	N = 500
Python	0.0171	0.167	1.031
Julia (direct Transfer)	0.408 / 0.012	0.479 / 0.0789	0.851 / 0.422
Julia (vectorized)	1.285 / 0.00070	1.316 / 0.0129	1.354 / 0.0949

Forces

	N = 64	N = 200	N = 500
Python	0.0177	0.173	1.036
Julia (direct Transfer)	0.046 / 0.0070	0.109 / 0.0692	0.470 / 0.423
Julia (vectorized)	0.379 / 0.00077	0.391 / 0.0121	0.446 / 0.091

Hessian

	N = 64	N = 200	N = 500
Python	0.0382	0.335	2.115
Julia (direct Transfer)	0.123 / 0.0148	0.256 / 0.1396	0.974 / 0.931
Julia (vectorized)	0.860 / 0.0025	0.932 / 0.02828	1.061 / 0.146

Energy Minimization (steps = 5000)

	N = 64	N = 200	N = 500
Python	179.1	1643.5	10164.9
Julia (direct Transfer)	71.1 / 71.1	697.7 / 697.7	4433.1 / 4433.1
Julia (vectorized)	7.24 / 6.96	84.0 / 84.0	412.7 / 412.7

3.9 Summary

In this chapter, we introduced the method Ascent Dynamics for intelligently sampling the potential energy landscape. Despite the great success of previous methods for sampling the energy landscapes and unveiling insights to various phenomena, a computationally efficient and non-biasing method was of interest. In the previous chapter, we discussed one of the most popular biasing methods, metadynamics, however, here we showed that the computational time of the method increases at best linearly as the landscape is sampled. As a result, the computational slow down impedes metadynamics from sampling a larger portion of the landscape or from studying larger system sizes. Comparatively, a class of methods coined surface walkers has shown great promise for simple landscapes of one dimension.

In this chapter, we extended the class of surface walkers to sample landscapes of any dimension by decomposing the force vector by the principle components of the second derivative Hessian matrix, or the landscape abstractly. By changing the sign of the lowest curvature directions of the force, the system configuration is updated in the direction of a local transition state. As a result, Ascent Dynamics efficiently

samples transition states of a system. The lowest curvature directions are indicative of the dynamics of the system, as has been thoroughly discussed in other works.

The method is first verified on mathematical problems of several dimensions. The various verification problems support that the method converges to transition states of interest. The method is then validated to work on real systems by applying the method to a vacancy diffusion problem of a two dimensional Lennard-Jones crystal with one vacancy. The vacancy is shown to diffuse from one site to another as expected.

Further, we discuss and show the relevance of developing a method for sampling higher dimensional transition states. Previous surface walking methods, such as GAD and ART, emphasized phenomena that can be described accurately on a one dimensional energy landscape, such as the vacancy diffusion problem. However, many systems undergo transitions that are indicative of higher order transitions states, for example liquids, glasses, proteins, and many more, as has been discussed thoroughly in literature. Thus, by allowing for the "steepness" of the method to be tuned, the transition states of interest can be more directly targeted for sampling.

Ascent Dynamics was developed into a package in the programming language Julia maintained on GitHub The linear algebra packages used in Julia were of interest for the development of this package.

In the next chapter, Ascent Dynamics will be applied to a model liquid system, a two dimensional polydisperse liquid, to validate Ascent Dynamics ability to unveil insights to real systems with complex transition states.

Chapter 4

Varied Steepness Ascent Dynamics of a 2-D Polydisperse Model System

4.1 Introduction

To test the utility of Ascent Dynamics, we apply the method to study a model liquid system composed of a polydisperse atoms. In this chapter, using Ascent Dynamics, the energy landscape of a model system is computed. Further, the effects of the steepness parameter, s, is determined with this model system. From the energy landscape, Ascent Dynamics is shown to unveil unique dynamics in a highly dense system that would otherwise show dynamics outside the scale of most molecular methods.

4.2 Polydisperse Formulation

The polydisperse system from [92, 93] was chosen as a model liquid to study the utility of Ascent Dynamics with. The polydisperse system has a continuous distribution of atom sizes with a high density of small particles and a low density of larger particles to frustrate the system. The large particles disrupt the system such that crystallization of the smaller particles is discouraged. This system was chosen because a clear collective variable to describe the dynamics of the system is unavailable. Thus, we can show the benefit of using multiple eigenvectors for liquids with this system.

The potential of the polydisperse system is

$$U_{ij}(r) = v_0 \left(\frac{\sigma_{ij}}{r}\right)^n + c_0 + c_1 \left(\frac{r}{\sigma_{ij}}\right)^2 + c_2 \left(\frac{r}{\sigma_{ij}}\right)^4 \tag{4.1}$$

where i and j represent the atom number, σ_{ij} is the effective atom radius for the interaction between atoms i and j, c_0, c_1, and c_2 are coefficients such that the potential, the first derivative with respect to r, and the second derivative with respect to r are 0 at $r = 1.25\sigma_{ij}$, and $n = 12$. The polydisperse potential is shown in Figure 4.1 A. The potential is purely repulsive and has a smooth cut-off distance for the potential and the force at $r = 1.25\sigma_{ij}$ shown by 4.1 A.

A

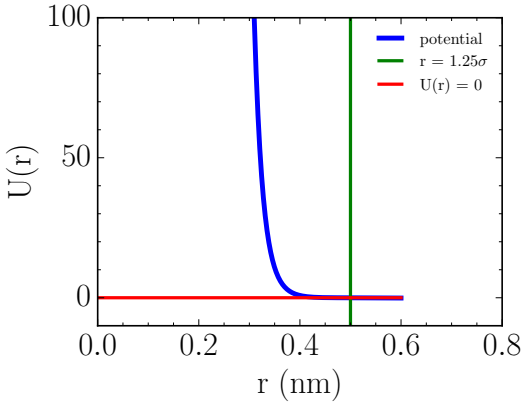

B

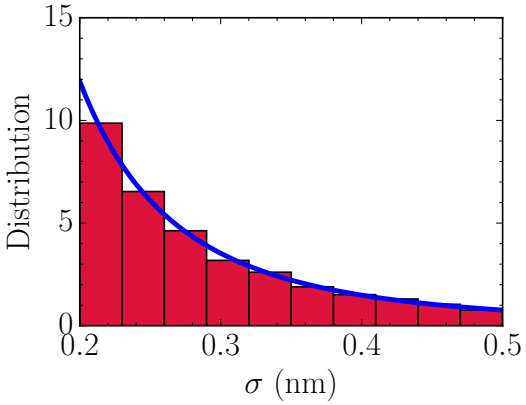

Figure 4.1: (A) The polydisperse potential is plotted in blue. In green, the location of $r = 1.25\sigma_{ij}$ is shown, and in red, the location of $U(\mathbf{r} = 0$ is shown as a guide for the eye to cut-off of the potential. The potential is purely repulsive, and is first and second order smooth at the cut-off distance. (B) The distribution of the atom sizes in nanometers is shown. The red histogram shows the results of the codes sampling of the distribution. The blue line shows the exact distribution of $f(\sigma) = A\sigma^{-3}$.

The effective atom radius between two atoms is explicitly defined as

$$\sigma_{ij} = \frac{\sigma_i + \sigma_j}{2} \tag{4.2}$$

where σ is the diameter of the atom selected randomly from the distribution $f(\sigma) = A\sigma^{-3}$ between $\sigma \in [\sigma_{min}, \sigma_{max}]$. The atom sizes were therefore sampled from

$$F^{-1}(u) = ((1-u)\sigma_{min}^{-2} + u\sigma_{max}^{-2})^{\frac{1}{2}} \tag{4.3}$$

where u is the uniform distribution. The distribution of the atom sizes is shown in Figure 4.1 B. The figure shows the desired distribution as a blue line, and the distribution sampled in the simulation.

The potentials coefficients are explicitly defined as

$$\begin{aligned} c_0 &= -v_0\frac{1}{1.25^n} - \frac{1}{8}v_0 n\frac{1}{1.25^n}(n+6) \\ c_1 &= \frac{1}{4}v_0 n\frac{1}{1.25^n}(n+4) \\ c_2 &= \frac{v_0 n(n+2)}{-8 * 1.25^n} \end{aligned} \tag{4.4}$$

Arrived from

$$U_{ij}(r \geq 1.25\sigma_{ij}) = 0 \tag{4.5}$$

$$\frac{\partial U_{ij}}{\partial r_{ij}}(r \geq 1.25\sigma_{ij}) = 0 \tag{4.6}$$

$$\frac{\partial^2 U_{ij}}{\partial {r_{ij}}^2}(r \geq 1.25\sigma_{ij}) = 0 \tag{4.7}$$

Further, the first derivative of the potential or -**F** is defined as

$$\mathbf{F}_i = -\frac{\partial U_{ij}}{\partial \mathbf{r}} = \sum_{j \neq i} \left(-n v_0 \frac{\sigma_{ij}}{r^{n+2}} + \frac{2c_1}{\sigma_{ij}} + \frac{4c_2 r^2}{\sigma_{ij}^4} \right) \mathbf{r} \tag{4.8}$$

The Hessian matrix for the system is defined as

$$H(\mathbf{r}) = \begin{bmatrix} \frac{\partial^2 U}{\partial x_1 \partial x_1} & \frac{\partial^2 U}{\partial x_1 \partial y_1} & \cdots & \frac{\partial^2 U}{\partial x_1 \partial y_n} \\ \frac{\partial^2 U}{\partial y_1 \partial x_1} & \frac{\partial^2 U}{\partial y_1 \partial y_1} & \cdots & \frac{\partial^2 U}{\partial y_1 \partial y_n} \\ \vdots & \vdots & \ddots & \vdots \\ \frac{\partial^2 U}{\partial y_n \partial x_1} & \frac{\partial^2 U}{\partial y_n \partial y_1} & \cdots & \frac{\partial^2 U}{\partial y_n \partial y_n} \end{bmatrix} \tag{4.9}$$

and the second derivatives of the potential used in the Hessian are

$$\begin{aligned} H_{i,i}(\mathbf{r}) = \frac{\partial^2 U(\mathbf{r})}{\partial x_i \partial x_i} = \sum_{j \neq i} & v_0 n(n+2) \frac{\sigma_{ij}^n}{r^{n+4}} (x_i - x_j)^2 + 8c_2 \frac{1}{\sigma_{ij}^4} (x_i - x_j)^2 \\ & - v_0 n \frac{\sigma_{ij}^n}{r^{n+2}} + 2c_1 \frac{1}{\sigma_{ij}^2} + 4c_2 \frac{r^2}{\sigma_{ij}^4} \end{aligned} \tag{4.10}$$

$$\begin{aligned} H_{i,i+1}(\mathbf{r}) = \frac{\partial^2 U(\mathbf{r})}{\partial x_i \partial y_i} = \sum_{j \neq i} & v_0 n(n+2) \frac{\sigma_{ij}^n}{r^{n+4}} (x_i - x_j)(y_i - y_j) \\ & + 8c_2 \frac{1}{\sigma_{ij}^4} (x_i - x_j)(y_i - y_j) \end{aligned} \tag{4.11}$$

$$\begin{aligned} H_{i+1,i}(\mathbf{r}) = \frac{\partial^2 U(\mathbf{r})}{\partial x_i \partial y_i} = \sum_{j \neq i} & v_0 n(n+2) \frac{\sigma_{ij}^n}{r^{n+4}} (x_i - x_j)(y_i - y_j) \\ & + 8c_2 \frac{1}{\sigma_{ij}^4} (x_i - x_j)(y_i - y_j) \end{aligned} \tag{4.12}$$

$$\begin{aligned} H_{i+1,i+1}(\mathbf{r}) = \frac{\partial^2 U(\mathbf{r})}{\partial y_i \partial y_i} = \sum_{j \neq i} & v_0 n(n+2) \frac{\sigma_{ij}^n}{r^{n+4}} (y_i - y_j)^2 + 8c_2 \frac{1}{\sigma_{ij}^4} (y_i - y_j)^2 \\ & - v_0 n \frac{\sigma_{ij}^n}{r^{n+2}} + 2c_1 \frac{1}{\sigma_{ij}^2} + 4c_2 \frac{r^2}{\sigma_{ij}^4} \end{aligned} \tag{4.13}$$

where i is an even number for 0 to 2N-2. These terms are the tridiagonal terms of the matrix. The

non-tridiagonal terms are defined as

$$\begin{aligned} H_{i,j}(\mathbf{r}) = \frac{\partial^2 U(\mathbf{r})}{\partial x_i \partial x_j} =& - v_0 n(n+2)\frac{\sigma_{ij}^n}{r^{n+4}}(x_i - x_j)^2 - 8c_2\frac{1}{\sigma_{ij}^4}(x_i - x_j)^2 \\ &+ v_0 n\frac{\sigma_{ij}^n}{r^{n+2}} - 2c_1\frac{1}{\sigma_{ij}^2} - 4c_2\frac{r^2}{\sigma_{ij}^4} \end{aligned} \tag{4.14}$$

$$\begin{aligned} H_{i,j+1}(\mathbf{r}) = \frac{\partial^2 U(\mathbf{r})}{\partial x_i \partial y_j} =& - v_0 n(n+2)\frac{\sigma_{ij}^n}{r^{n+4}}(x_i - x_j)(y_i - y_j) \\ &- 8c_2\frac{1}{\sigma_{ij}^4}(x_i - x_j)(y_i - y_j) \end{aligned} \tag{4.15}$$

$$\begin{aligned} H_{i+1,j}(\mathbf{r}) = \frac{\partial^2 U(\mathbf{r})}{\partial y_i \partial x_j} =& - v_0 n(n+2)\frac{\sigma_{ij}^n}{r^{n+4}}(x_i - x_j)(y_i - y_j) \\ &- 8c_2\frac{1}{\sigma_{ij}^4}(x_i - x_j)(y_i - y_j) \end{aligned} \tag{4.16}$$

$$\begin{aligned} H_{i+1,j+1}(\mathbf{r}) = \frac{\partial^2 U(\mathbf{r})}{\partial y_i \partial y_j} =& - v_0 n(n+2)\frac{\sigma_{ij}^n}{r^{n+4}}(y_i - y_j)^2 - 8c_2\frac{1}{\sigma_{ij}^4}(y_i - y_j)^2 \\ &+ v_0 n\frac{\sigma_{ij}^n}{r^{n+2}} - 2c_1\frac{1}{\sigma_{ij}^2} - 4c_2\frac{r^2}{\sigma_{ij}^4} \end{aligned} \tag{4.17}$$

where i and j are even numbers from 0 to 2N-2. Here, we have defined $\mathbf{r} = [x_i - x_j, y_i - x_j]$.

4.3 Ascent Dynamics of Polydisperse System

4.3.1 Polydisperse Energy Landscape

Ascent Dynamics of a the previously defined polydisperse system is explored in this section. For this section and the next, the system considered has 500 polydisperse atoms sampled from in the range $[\sigma_{min}, \sigma_{max}] = [.1\text{nm}, .5\text{nm}]$. The box length is 3.77 nm, resulting in a packing fraction of $\phi = 0.92$. The packing fraction was computed from both the equation $\phi = \sum_i \sigma_i^2 \pi / 4L^2$, where σ_i is the effective diameter of atom i, and computed from approximating the amount of free space from discretization of the system into areas occupied by atoms and unoccupied by atoms, shown in Figure 4.2. For the polydisperse system, the following parameters were set $v_o = 1$, $n = 18$, $\eta = 0$, and the dimension was 2.

The initial configuration was created as a grid with the atom centers equally spaced in rows and columns. As 500 is not a perfect square, some of the grid spaces were left empty. The sizes of the atoms were then randomly determined from the sampling scheme described before. Energy minimization was performed on the system using steepest descent to converge on the initial configuration for the Ascent Dynamics simulation. An example of the system during the Ascent Dynamics simulation is shown in Figure 4.3 A.

For this section, the steepness parameter chosen was $s = 50$, or $s/N = 0.1$. The initial step size for

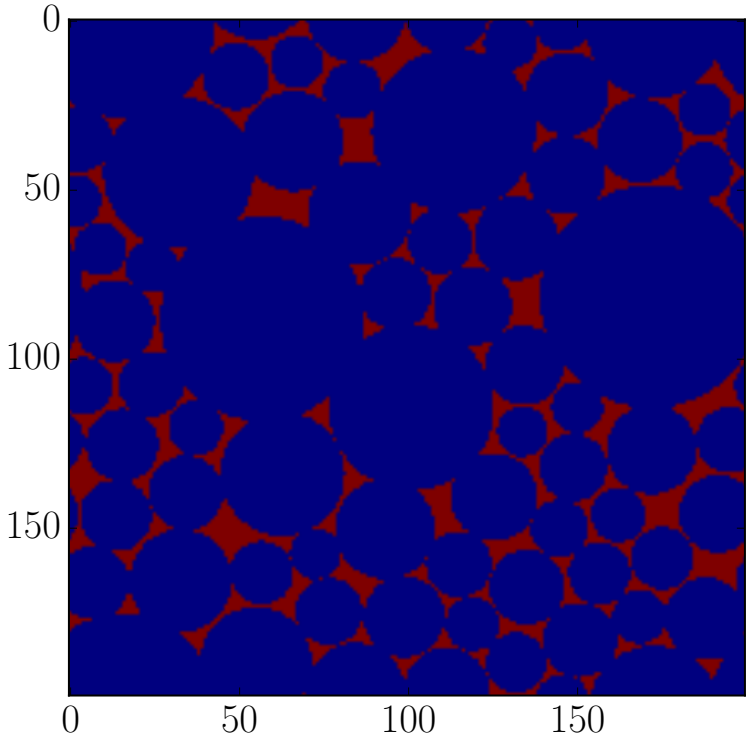

Figure 4.2: Figure of the calculation of the packing fraction from free space. Blue cells represent occupied space and red cells represent free space. The packing fraction is then the sum of the blue cells over the total number of cells. There are 200x200, or 4e4, cells in this image, which was found to be sufficient for estimating the packing fraction to two decimals.

ascents was .0006, with a maximum number of steps per ascent of 10000 and a minimum number of steps of 1000 to escape the initial region of low slope. The initial step size for descents was .0006, with a maximum number of steps per descent of 5000 and a minimum number of steps of 500. Convergence to a transition state or a minimum was considered when the relative change in energy per step was less than 1e-8. The total number of iterations of Ascent Dynamics, or the number of transition states sampled, was 200.

Figure 4.3 shows an example of one iteration of Ascent Dynamics on the described system. The system begins in a metastable state, defined by the force of the system being approximately zero, shown in Figure 4.3 A. The system then follows a minimum path computed by the formulation described in the previous chapter. At every step the local information is used to compute the next minimum step towards a transition state. The system after many steps converges to a transition state, in this case of order 50 because $s = 50$, shown in Figure 4.3 B. Here the atoms are colored by their individual displacement from the metastable state, with

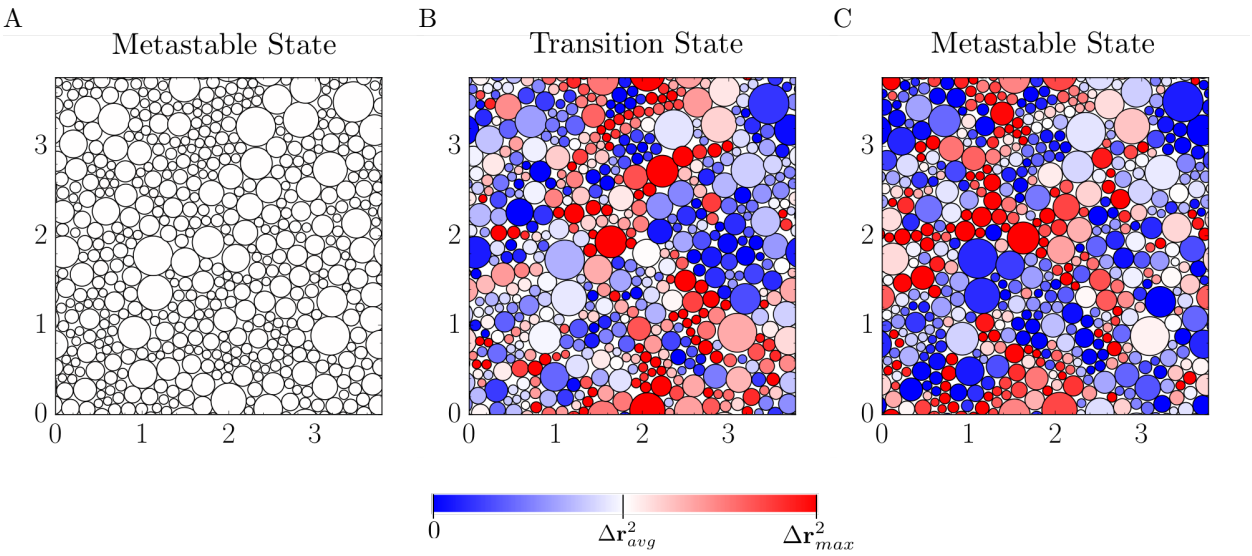

Figure 4.3: The three panels show an example transition from one metastable state to another with ascent dynamics. The atoms are colored by the squared displacement of the atom. Results here are shown for a 500 atom simulation.

a divergent color distribution where white represents average particle displacement, red represents large particle displacement, and blue represents little particle displacement. Lastly, from this transition state, steepest descent is performed to converge to a new metastable state shown in Figure 4.3 C.

Figure 4.3 the atoms are colored by the squared displacement defined as

$$\Delta \mathbf{r}_i^2 = |\mathbf{r}_i(\text{metastable state}) - \mathbf{r}_i(\text{current state})| \tag{4.18}$$

where $\mathbf{r}_i$ is the coordinates of atom i, $\mathbf{r}_i$(metastable state) is the coordinates of the atoms at the initial metastable state being escaped from in the Ascent Dynamics step, and $\mathbf{r}_i$(current state) is the coordinates of the atoms at the current state (either a transition state or a new metastable state). In other words, the atoms are colored by the displacement from the initial metastable state. Not to be confused with assuming that the atoms are colored by the sum of displacements undergone during each step to converge to the transition state. Thus, in Figure 4.3, blue atoms may have not moved from their position in the metastable state, but may have moved while sampling the path to the transition state.

From the color in Figure 4.3, it is clear that the system does not return to the original metastable state that the system escaped from during the ascent trajectory. Further, the figure shows clear regions or clusters of red atoms and blue atoms, representing highly mobile groups and low mobility groups. In the transition state, there exists clear regions where the particles have high displacements and clear regions

where the particles have low displacements. These regions similarly exist in the new metastable state as well. Closer qualitative analysis of these regions across the 200 sampled transition states reveals that highly mobile regions tend to be composed of atoms of variable size. Comparatively regions of lower mobility tend to be composed of mostly the same size. This observation is confirmed by performing a cluster analysis based on the mobility and studying the standard deviation of the particle size of the cluster as a function of the mobility. This observation is supported by the fact that large variation in particle size increases the local frustration in the region, while low variation allows for the region to become fairly organized. Thus, for this system, one structural indicator of a mobile group could be the variation in particle size of the region.

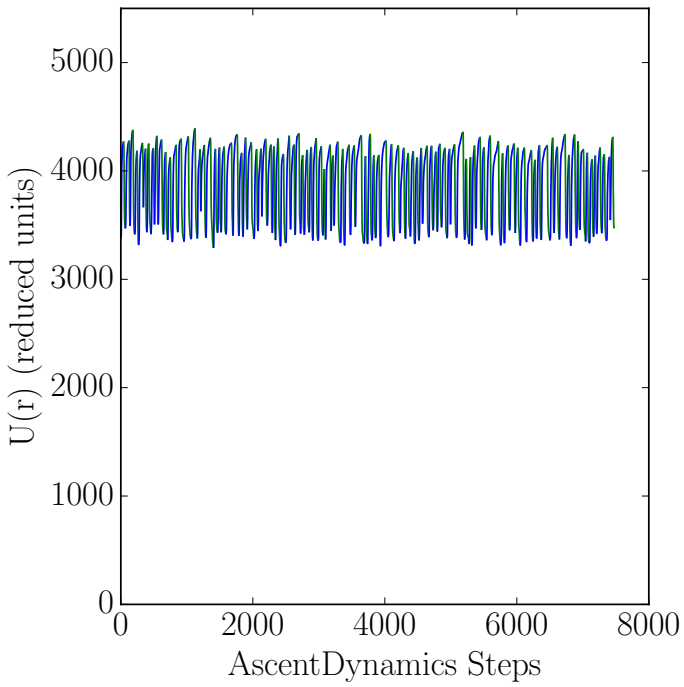

Figure 4.4: Potential energy landscape sampled by Ascent Dynamics for a 500 atom simulation of polydisperse atoms with $s = 50$. Ascents are plotted in blue and descents are plotted in green.

While Figure 4.3 shows an example of a single iteration of Ascent Dynamics, the simulation performed 200 iterations of transition state sampling. The resulting energy landscape sampled is shown in Figure 4.4. The figure shows that an Ascent Dynamics trajectory results in a rich sampling of the energy landscape. Interestingly, the figure shows that with the Ascent Dynamics method, the transition states sampled have similar energies. This is the result of Ascent Dynamics always sampling transitions of the same order, which will generally have similar energies [94].

Figure 4.5 shows the distribution of system distances for ascents and descents. The figure shows that the

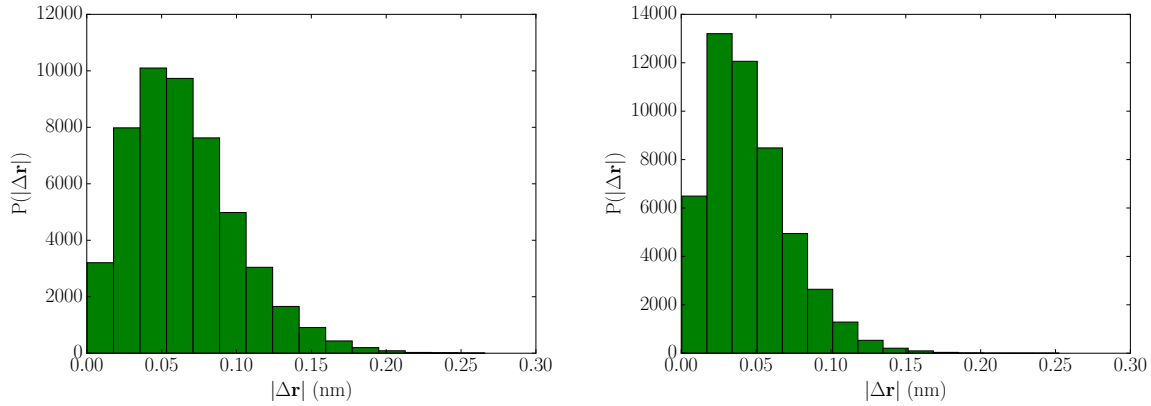

Figure 4.5: Distribution of distances for (A) ascents and (B) descents.

system undergoes smaller displacements when converging to a metastable state than to a transition state. This is the result of following steepest descent which encourages convergence to the closest metastable state, where as the ascent dynamics algorithm may need to search for a longer period to converge to a transition state.

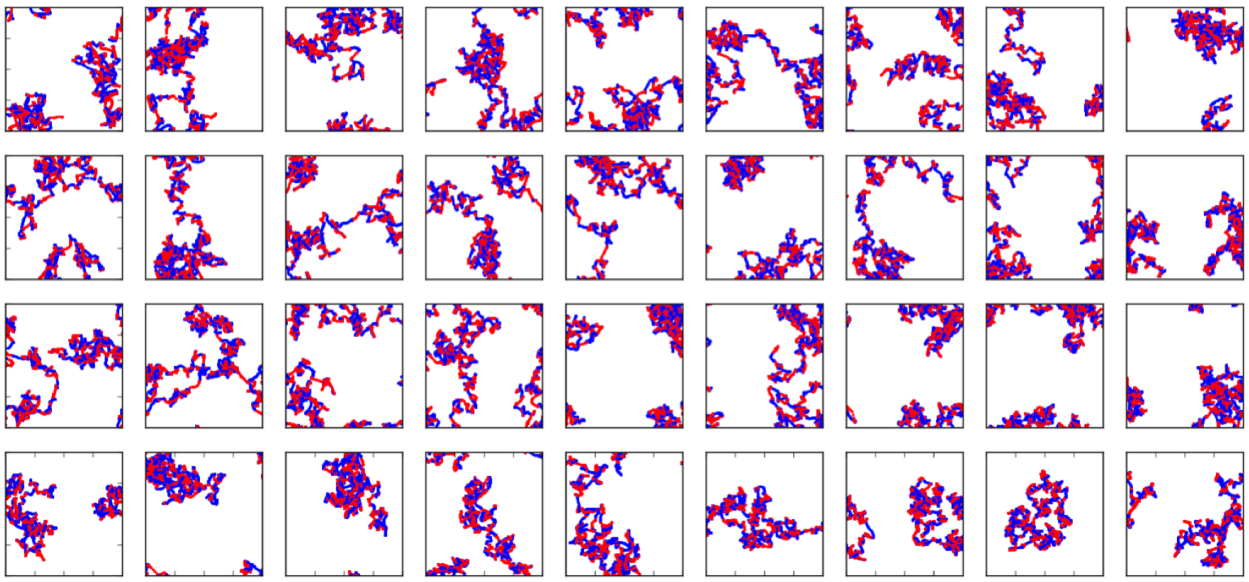

Figure 4.6: Individual trajectories of particles in a simulation. The trajectory is blue for descents and red for ascents.

While Figure 4.3 shows that in a single iteration of Ascent Dynamics the system does not return to the original metastable state, we need to guarantee that the system does not return to the same metastable state after multiple or alternating iterations of Ascent Dynamics. In metadynamics this is guaranteed by the history dependence of the penalty function preventing the revisiting of metastable states, however, Ascent

Dynamics has no guarantee that revisiting will not occur. Figure 4.6 shows individual trajectories of the atoms in the Ascent Dynamics simulation. Thus, this figure shows that at least for moderate steepness factors, revisiting is unlikely as the figure shows that the particles are indeed undergoing some long range displacements and trajectories.

4.3.2 Tuning of Steepness Parameter

In metadynamics, there were two control parameters that determined the scale of the energy landscape dynamics sampled, the height and width of the penalty function being applied to the system. As shown in Figure A.1, the height and width for metadynamics has a very large impact on the scale of the landscape sampled. The width determines the efficacy with which the basins are filled, and the height determines the scale of the barriers sampled. As discussed thoroughly in my masters, the width and height of a metadynamics simulation are critical to sampling the dynamics desired.

Similarly, Ascent Dynamics also has a control parameter that determines the scale of the dynamics sampled. Previously mentioned briefly in the previous chapter, the steepness parameter is essential to the effectiveness of Ascent Dynamics to sample the energy landscape at a desirable scale. At this point, the steepness parameter has been discussed in terms of it making Ascent Dynamics effective for systems that have more than one underlying descriptor. Particularly, the need for higher steepness parameters for sampling dynamics more complex than single variable dynamics such as vacancy diffusion. In this section, the effect of controlling the steepness parameter will be evaluated.

For this section, the same system in the previous section was evaluated. However, the steepness parameter was varied from 5 to 50 by 5, and also 75 was performed, for the same number of iterations and from the same initial setup.

Figure 4.7 shows three energy landscapes sampled by Ascent Dynamics, for (A) $s = 25$ (B) $s = 50$ and (C) $s = 75$. These three steepness factors were selected to show the range of the landscapes sampled. The figure shows that by increasing the steepness factor the energy landscape sampled changes drastically. Particularly, the range of the landscape increases as the steepness parameter is increased. It is worth noting, that as the steepness parameter increases, the number of steps required per minimization or transition state sampling increases, or the steps to convergence is increased.

The change of the energy landscape sampled is more clearly displayed in Figure 4.8. Figure 4.8 A shows the average energy of the minimums and transition states sampled in the Ascent Dynamics simulation as a function of the steepness parameter (The figure uses the reduced steepness parameter which will be discussed

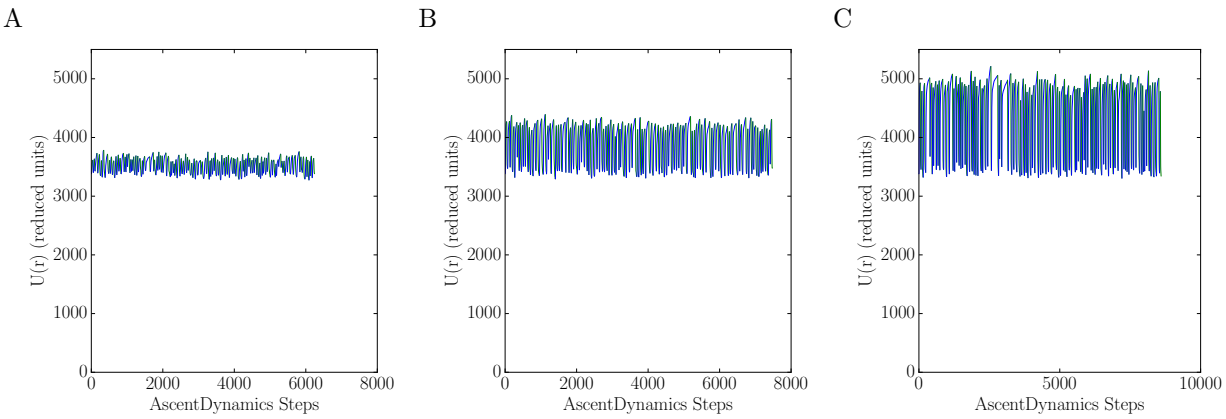

Figure 4.7: Potential energy landscape sampled for a 500 atom simulation of polydisperse atoms from Ascent Dynamics for (A) $s = 25$ (B) $s = 50$ and (C) $s = 75$. The figures are shown on the same scale to clearly show the effect of increasing the steepness parameter s.

in the next section). As previously alluded to, the scale of the transition state energy increases as a function of the steepness parameter, in a seemingly linear trend. Interestingly, the scale of the minimums sampled is uncorrelated with the steepness parameter, displaying no change as the steepness is increased. This is expected for this system as the system was chosen for its lack of a clear minimum state, or because this system is expected to have a rough energy landscape.

Similarly, Figure 4.8 B shows the energy barriers sampled as a function of the steepness parameter. The energy barrier shows a nearly linear relationship with the steepness parameter. The figure further shows standard deviation of the energy barriers computed as bars in the figure. Thus, not only does the average energy barrier increase linearly with the steepness parameter, but the distribution of energy barriers increases with steepness parameter. This implies that the landscape is rougher at higher transition state levels.

Figure 4.9 A shows the trajectories of the simulations as a function of Ascent Dynamics steps, with darker colored lines representing increasing steepness parameter of the simulation. Figure 4.9 B shows the final system displacement of the system as a function of the steepness parameter. Other than the outlier at around $s/N = 0.05$, the displacement of the system increases for increasing steepness parameter. This is mostly likely due to there being an increasing number of transition states for higher steepness factors and an increasing number of pathways along the landscape when higher order transitions are sampled [95, 96, 94].

The trends observed in this section will continue as the steepness parameter is increased further to an extent. As previously discussed briefly, once the steepness parameter is equal to the number of atoms in the system, or the reduced steepness factor is 0.5, the system will display two atoms centers converging on one another. Thus, the trends here should continue to $s = N$ at which point the trends will diverge.

A

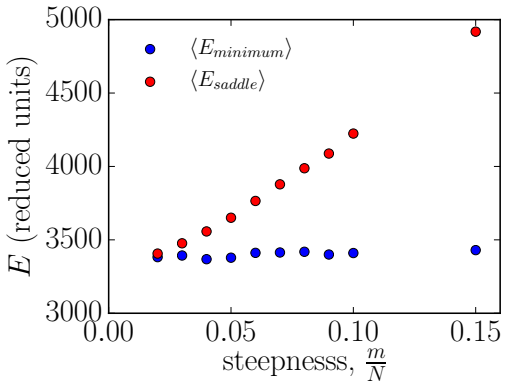

B

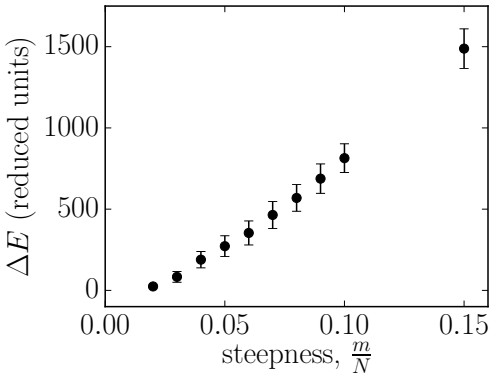

Figure 4.8: (A) The average energy of the minimums and saddles sampled as a function of the steepness parameter. The saddles energy is plotted in red and the minimums are plotted in blue. (B) The average energy barrier sampled as a function of steepness parameter.

The steepness has recently been shown to be very essential in other dynamics as well such as crystallization. Similar to the parameters in metadynamics, it was found that if the steepness parameter is too small, the system will overcome barriers so small that crystallization will never occur. Similarly, steepness parameters too large will result in crystallization occurring so fast that the intermediate steps are not seen. However, a steepness parameter in the middle, a very appropriate steepness results in a clear simulation of the crystallization process.

Thus, the steepness parameter can be easily used to control the type of dynamics sampled in an Ascent Dynamics simulation. While in metadynamics the pair distribution function and or mean squared displacement can be used to quickly determine the width of the penalties used, a clear heuristic method to determine the steepness parameter is still needed. One option is to use the linear relation between average displacement per transition state or the energy barrier and the steepness parameter to estimate a good steepness parameter if an estimate of these two quantities is known before hand. It has been theorized that the saddle order in liquids and the temperature of the system are directly correlated [88, 89]. As a result, this correlation of the two may offer a viable approach for determining an appropriate steepness factor.

4.3.3 Atom Size Effects

For this section, a smaller system was considered. The packing fraction was kept the same at $\phi = 0.92$. For the polydisperse system, the following parameters were set $v_o = 1$, $n = 18$, $\eta = 0$, and the dimension was 2. The number of particles used in this section was 64.

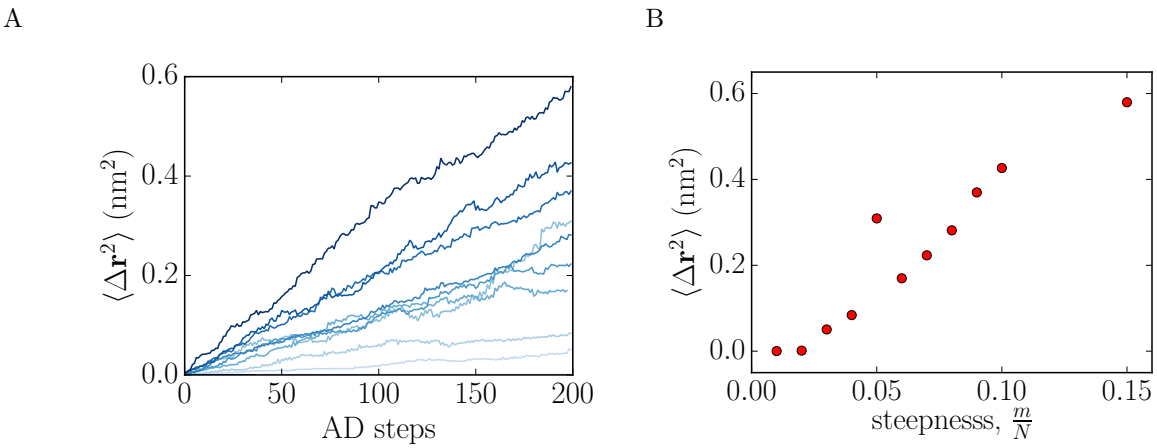

Figure 4.9: (A) The displacement of the system as a function of Ascent Dynamics steps. Higher steepness parameter trajectories are shown in darker colors. (B) Final system displacement of the system as a function of steepness parameter.

For this section, the steepness parameter chosen was $s = 9$, or $s/N = 0.14$. The initial step size for ascents was .0006, with a maximum number of steps per ascent of 10000 and a minimum number of steps of 1000 to escape the initial region of low slope. The initial step size for descents was .0006, with a maximum number of steps per descent of 5000 and a minimum number of steps of 500. Convergence to a transition state or a minimum was considered when the relative change in energy per step was less than 1e-8. The total number of iterations of Ascent Dynamics, or the number of transition states sampled, was 200.

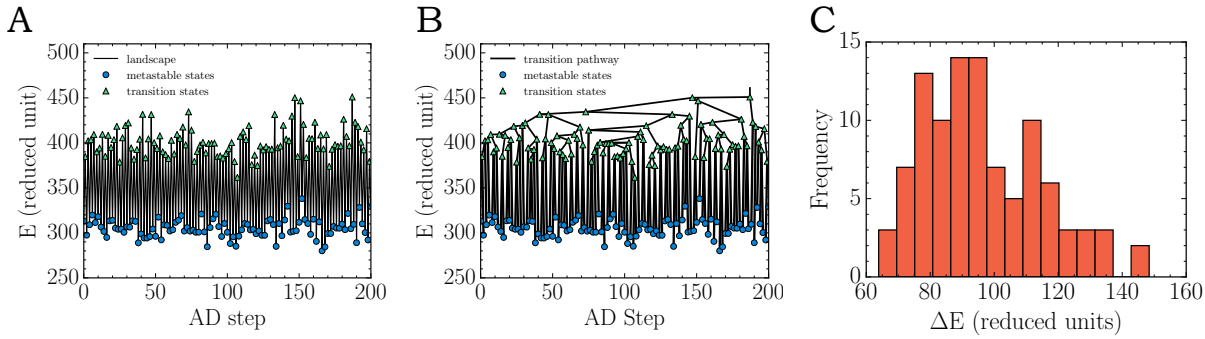

Figure 4.10: (A) The sampled energy landscape. (B) Disconnectivity plot of the landscape. (C) Distribution of transition energies.

Figure 4.10 A shows the energy landscape sampled during the ascent dynamics simulation. Like most model liquid systems, the metastable states are close in energy value as are the transition energies. Thus, there are no clearly distinct regions of the landscape. In other words, the landscape for dense liquids is rough

with similar metastable and transition states.

Figure 4.10 B shows the disconnectivity plot of the ascent dynamics simulation. This figure shows the required transition states required for the system to travel along the landscape from one metastable state to another. This shows the distinct regions of the landscape separated by the larger energy barriers.

Figure 4.10 C shows the distribution of the energy barriers sampled. Each data point is the energy required to go from one metastable state to either the forward or backward transition state. As to be expected, the distribution is roughly normal around an average value of 95 reduced units. The range of transition energies is from 60 to 150 reduced units, or an average barrier of 1.4 in reduced units per atom indicates these are substantial barriers being sampled.

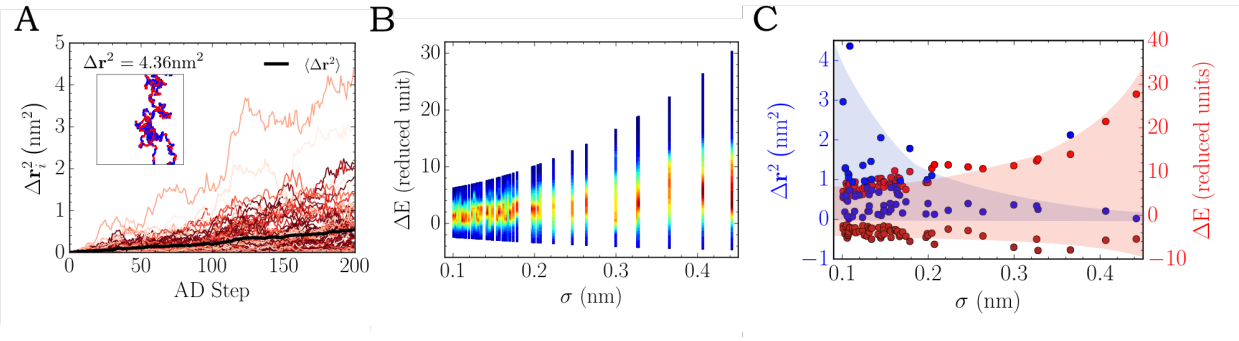

Figure 4.11: (A) The squared displacement of each particle as a function of AD step. Lighter lines indicate smaller atoms, darker lines are larger atoms. (inset) Trajectory of the most displaced atom in the system with a total displacement on 4.36 nm^2 (blue: ascent, red: descent). The black line is the system averaged squared displacement. (B) Distribution of transition energies for each particle. (C) (blue) Total squared displacement of each particle based on its diameter. (red) Largest and smallest transition energy of each particle based on its diameter. The colored region is to guide the eye to the area covered for each quantity.

Figure 4.11 A shows the squared displacement of each particle as a function of AD step. The squared displacement of each particle and the system squared displacement shows the system never returns to a previous minimum or transition point, each iteration of ascent dynamics drives the system further along the energy landscape providing a unique trajectory along the landscape. The inset shows an example trajectory of one of the particles. The red points indicate an ascent trajectory and blue points indicate a descent trajectory.

Figure 4.11 B shows the distribution of transition energies for each particle as a function the particle's diameter. In other words, for each particle, the change in energy from a minimum to the next corresponding transition is plotted as a density distribution. From the figure, as a particles diameter increases the average energy per transition increases linearly. For the smallest particles, the change in energy during a transition is about 1/10 that of the largest particles. This implies that transitions are dominated by the movement

of larger particles, and the movement of the smaller particles are in response to this motion. Further, the spread or standard deviation of the distribution increases non-linearly as the particle diameter increases.

An interesting feature of Figure 4.11 B, is a portion of each particle's distribution is negative. This paints a unique picture of the transition state for a liquid. Prior understanding of a transition was that the system as a whole was following an increasing trajectory along the energy landscape, in which the system ends in a higher energy state. However, it appears that while most particles are increasing in energy, some of the particles are undergoing a relaxation process while the others are being excited. In the lens of cooperative dynamics, this paints a picture that certain particles lead the transition process and are therefore in an excited state, but other particles follow behind relaxing into the space created by the excited particles. In the lens of the energy landscape, while the system as a whole is following an increasing energy pathway, along the pathway, certain directions are decreasing in energy.

Figure 4.11 C shows two quantities. The blue points and left y-axis shows the total displacement of each particle as a function of the particle's diameter. The red points and right y-axis shows the maximum and minimum change in energy from a minimum to a transition point as a function of the particle's diameter. The shaded regions are a guide for the eye to show the region covered by the quantity. This figure shows that the most mobile particles are generally smaller particles. Further, as the particle diameter increases, the mobility decreases significantly. There is an inverse relationship between the energy change and the total distance traveled by the particle. The most mobile particles have the lowest changes in energy and smallest diameter, while the least mobile have the largest changes in energy and largest diameters.

Further, it was found that increasing the steepness factor, or when sampling higher order transition states, the distribution of the barriers for larger atoms increases at a far faster rate than the smaller atoms. This indicates that larger energy transition states are increasingly dominated by the mobility of the large atoms. As the larger atoms are the source of frustrating the system, the larger atoms logically impede the transitions of the system.

4.3.4 Normalized Parameters

Since two system sizes were discussed in this chapter, how to compare the two is critical to understanding the Ascent Dynamics method. As Figure 4.10 A and Figure 4.4 show, different system sizes result in different energies for the energy landscape. It has been shown in several previous works that to compare these two systems the normalized energy must be used for this system. Thus, the landscape per atom is comparable, or using U/N is comparable regardless of system size.

Similarly, as previously mentioned briefly, in order to compare two Ascent Dynamics simulations of different sizes the reduced steepness factor should be considered. The steepness factor can range from 0 to 2N for 2-D systems, and thus, the two systems in this chapter have ranges of 0 to 1000 and 0 to 128 respectively for sizes 500 and 64 atoms. Regardless of system size the lowest three eigenvectors are always the center of mass translation and rotation. Thereafter though, increasing the steepness factor increases the scale of the dynamics more drastically for smaller systems. However, we found that if Ascent Dynamics simulations with similar values for s/N are compared, the two simulations are comparable. For example, the 64 atom system with $s = 9$, or $s/N = .14$, and the 500 atom system with $s = 75$, or $s/N = .15$, display similar energy landscapes, statistics, and average displacements per iteration.

Therefore, the value of s/N truly determines the scale of the transition states and dynamics sampled by Ascent Dynamics. Interestingly, this implies though that for the same scale of transition states, larger systems have larger order transition states.

4.3.5 Extension of Method

Thus far, we have focused on a two dimensional polydisperse system. In this section, extending the method to higher dimensions will be the focus. In terms of method implementation, by extending to three dimensions, the computational difficulty of the method should remain relatively constant. However, the major difference will be 3 trivial eigenvectors instead of 2 trivial eigenvectors will always exist in the eigenspace. The three eigenvectors will relate to center of mass translation in the x-, y- , and z- directions. Further, the value of s for ideal landscape sampling will be higher because of the increase in dimensionality.

To prove Ascent Dynamics is sufficient for transition state sampling in three dimensions, Figure 4.12 shows an example of an Ascent Dynamics simulation on a 3-dimensional polydisperse system. The system is identical to the one discussed thus far in the chapter, but in three dimensions. The exact potential is derived in the Appendix sections.

The noticeable differences between three dimensions and two dimension simulations of the polydisperse system is the number of iterations to converge to a transition state is higher for three dimensions than two dimensions.

Ascent dynamics was also tested on a model water system called MB-water. The potential is derived in the Appendix sections. This model is two dimensional in space, but a three dimensional system as each atom is defined by an x-, y-, and θ- coordinate, where θ determines the angle between the horizontal plane and the hydrogen bond. This system was used to test the success of Ascent Dynamics on systems that have

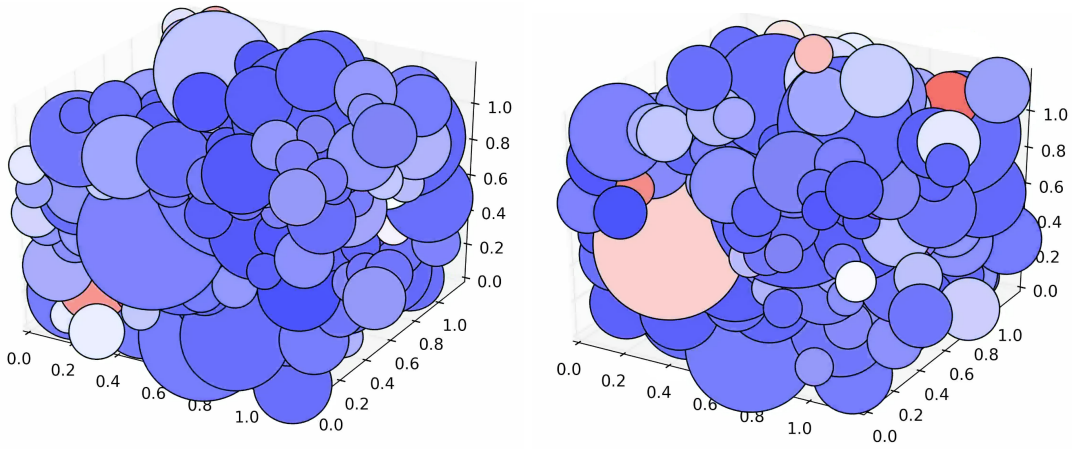

Figure 4.12: Three dimensional polydisperse system. From left to right, the figure shows the transition state sampled with Ascent Dynamics when applied to a three dimensional polydisperse system. The atoms are colored based on the total displacement from the initial state, blue representing little to no displacement and red representing large displacement, similar to Figure 4.3.

torsional transition states.

Thus, in both cases, increasing the complexity of the problem resulted in a slight increase in the computational cost of Ascent Dynamics. However, no more of an increase than would be noticeable in any other advanced sampling method, or molecular dynamics simulation.

4.4 Summary

In this chapter, the Ascent Dynamics method was applied to a model liquid system defined by the two-dimensional polydisperse potential. This potential was chosen because the polydispersity discourages order in the system, making it an ideal model liquid system. Ascent Dynamics was then shown to result in convergence to transition states in a system with a jammed packing fraction. While the exact timescale was not determined, the packing fraction was set to a value that would result in incredibly slow or sluggish dynamics in a molecular dynamics simulation.

Ascent Dynamics was shown to determine a sampled energy landscape with an assortment of transition states. The method was shown to result in transition states that are less local than the subsequent minimum sampled from the transition state. More clearly, the distance traveled by the system to converge at a transition state was larger than the distance traveled to converge to a new minimum state after the transition state was sampled.

Using this system as a model, the significance of the steepness parameter s was investigated in this

chapter. The steepness parameter as the name implies was shown to determine the scale of the transition state sampled. Particularly, higher values of s sampled more complex transition states, where the complexity is determined by the number of negative eigenvalues at the transition states. Further, higher values of s resulted in higher energy transition states being sampled. Traditionally in the landscape formalism, larger energy barriers between two neighbor minimums is considered to represent longer timescales. Thus, we assume that s can be used to determine the time scale of the phenomena of interest. This is further shown by simulations with larger s values resulting in larger rearrangements and longer displacements, indicative of longer timescales in a system.

Further, from this simulation, it was shown that the larger atoms despite having lower mobilities in the simulation contributed the largest portion of energy barrier. We conclude then that large atoms the determining factor in the frustration in the system. Lastly, Ascent dynamics is shown to be extendable to higher dimension systems with only a slight decrease in computational cost that would be expected of increasing the complexity of the landscape being sampled.

In the next chapter, methods for determining the timescale from an energy landscape sampling will be discussed.

Chapter 5

Temporal Information from the Landscape

5.1 Introduction

Until this point, we have mainly emphasized on the height of the energy barriers, discussing transition states solely in terms of there energy values. In this chapter, we will discuss some potential methods for producing the time scales of the transition states being sampled. In the previous chapters, we have assumed the time scale being simulated due to the phenomena being simulated is known to occur on very long time scales relative to those accessible by molecular dynamics.

5.2 Timescale from Maxwell Relaxation Time

Molecular dynamics simulations update the atom positions by integrating Newton's equations of motions, which results in atomic trajectories based on time [7]. However, all-atom metadynamics simulations update atom positions based on the energy of the system, which results in atomic trajectories as a function of energy. Thus, a all-atom metadynamics simulation results in an energy landscape as a function of all-atom metadynamics step. The landscape can be used to determine the energy barriers separating the configuration basins. We can also use our temperature mapping method to determine the temperature of that energy basin. We assume that the relaxation time, τ, for a given basin, $\mathbf{r}(\alpha_1)$, at a mapped temperature, T, separated from a neighboring basin, $\mathbf{r}(\alpha_2)$, with energy barrier, E_a, can be calculated from the Arrhenius relation for the relaxations time

$$\tau(T, E_a) = \tau_M \exp\left(\frac{E_a}{k_b T}\right) \tag{5.1}$$

where τ_M is the Maxwell relaxation time for the material or $\tau_M = \eta/G_\infty$ [97]. By using this relation, we transform the landscape sampled from a function of all-atom metadynamics step to time.

This method assumes that dynamic trajectories are a two step process. The first step involves the system oscillating within a energy basin of the landscape and undergoing an activated process to a transition state.

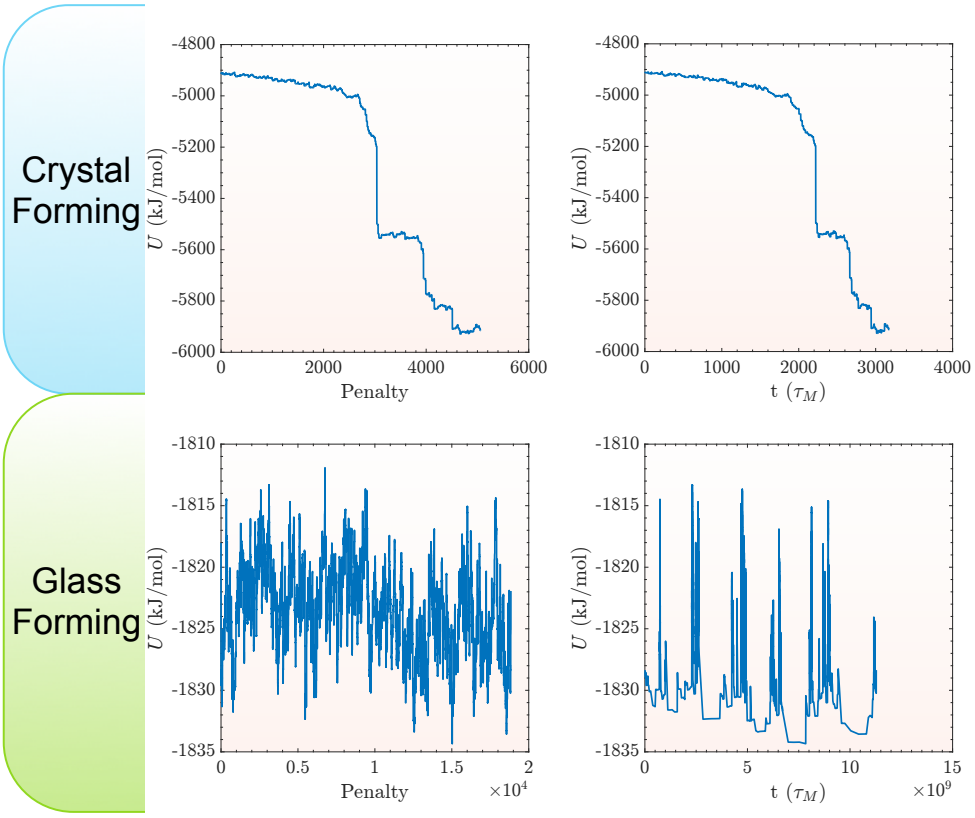

Figure 5.1: The top panels show the energy landscape of a crystal forming simulation (chapter 2) and the landscape once extrapolated to the time in terms of the Maxwell relaxation time. The bottom panels show the same analysis for a liquid and glass forming system.

The second step involves the system relaxing to a energy basin of the landscape. The entire process is assumed to occur with a probability based on the height of the transition state energy, and the timescale is based on the probability of occurring and the relaxation time of the system.

To display this method, two systems were run with all-atom metadynamics. The first system, analyzed in Chapter 2, is a monoatomic Lennard-Jones system, a known crystal former. The second system is a binary Lennard-Jones system, which is often used as a model liquid. The binary Lennard-Jones potential is defined as is [98]

$$U(\mathbf{r}) = \sum_i \sum_{j \neq i} 4\epsilon_{ij} \left[\left(\frac{\sigma_{ij}}{r_{ij}} \right)^{12} - \left(\frac{\sigma_{ij}}{r_{ij}} \right)^{6} \right] \tag{5.2}$$

where ϵ_{ij} and σ_{ij} is the potential depth and atom diameter based on the atom types i and j. This potential has a corresponding force of

$$\mathbf{F}_i = -\sum_{j \neq i} 4\epsilon_{ij} \left[\frac{12\sigma_{ij}^{12}}{r_{ij}^{14}} - \frac{6\sigma_{ij}^{6}}{r_{ij}^{6}} \right] \mathbf{r_{ij}} \tag{5.3}$$

The binary Lennard-Jones system simulated with all atom Metadynamics consists of 223 Lennard-Jones atoms with 178 atoms of type A (≈80%) and 45 atoms of type B (≈20%) in a periodic cubic box. The Lennard-Jones parameters are ϵAA =1.0, σAA =1.0, ϵBB =0.5, σBB =0.88, ϵAB = 1.5, σAB = 0.8 in reduced units. The penalty energy function height, H, and width, σ, used to sample the energy landscape was 1 kJ/mol and 0.1 nm, respectively.

Table 5.1: Table of raw data for the protein simulations performed.

Protein Name	PDB Name	Experimental Folding Time (us)	Energy Barrier	Number of Atoms	Width (nm)	Height (kJ/mol)
Chignolin	1uao	0.6	4.47E+02	138	1.00E-01	1.00E+03
alpha 3d	2a3d	27	1.61E+03	1140	1.00E-01	1.00E+03
bba	1fme	18	1.47E+03	504	1.00E-01	1.00E+03
bbl	2wxc	29	1.48E+03	710	1.00E-01	1.00E+03
gamma repressor	1lmb	49	1.59E+03	1352	1.00E-01	1.00E+03
homeodomain	2p6j	3.1	1.13E+03	919	1.00E-01	1.00E+03
ntl9	2hba	29	1.42E+03	825	1.00E-01	1.00E+03
protein_b	1prb	3.9	9.94E+02	851	1.00E-01	1.00E+03
protein_g	1gb1	65	1.46E+03	855	1.00E-01	1.00E+03
trp-cage	2jof	14	1.04E+03	284	1.00E-01	1.00E+03
villin	1vii	2.8	9.87E+02	596	1.00E-01	1.00E+03
ww domain	1i6c	21	1.30E+03	612	1.00E-01	1.00E+03
1BDD	1bdd	7.9	1.28E+03	941	1.00E-01	1.00E+03
1ENH	1enh	25.1	1.54E+03	1046	1.00E-01	1.00E+03
1FKB	1fkb	2.00E+05	3.91E+03	1663	1.00E-01	1.00E+04

Figure 5.1 shows the results of mapping the landscape of a crystal forming and a glass forming system to time based on the height of the barriers and the Maxwell relaxation time. First of note, if the relaxation time is on the scale of cage breaking or the ballistic regime of the mean squared displacement of these two systems (i.e. on the scale of hundreds of femtoseconds), then the crystal forming landscape is mapped to a timescale of hundreds of picoseconds. This is to be expected as the timescale of crystallization is magnitudes faster than the timescale of nucleation to occur in a supercooled system. Comparatively, the glass forming system has a landscape with dynamics on a much larger timescale, including regions where the system is stuck for extremely long periods of time, as is expected with glass forming systems that are under arrest. Additional information about this method can be found in [5], where the method and data was initially discussed.

5.3 Timescale from Experimental Values

A direct method for computing the time scale of the sampled energy landscape, either from all-atom metadynamics, Ascent Dynamics or any other energy landscape sampling method, is to compare the landscape to reported experimental values. For example, in this section, all-atom Metadynamics simulations were performed on a series of protein systems and compared to experimental and molecular dynamics simulations reported in [6].

the proteins simulated with all-atom metadynamics are include in Table 5.1. The protein name, PDB name, experimental folding time and number of atoms were determined from the proteins database information contained in PDB database. Further, twelve of the atoms included were simulated with molecular dynamics in [6]. The additional three selected were chosen because of there range of experimental folding times. The simulations were performed in our all-atom metadynamics package with a penalty height and penalty width list in Table 5.1. Except for protein 1FKB, all simulations were performed with a width of 1.00e-01 nm and a height of 1.00e+03 kJ/mol, as this width and height was determined to be appropriate for sampling the dynamics of these systems. Simulations were also performed with widths and heights varied by +/- 3 orders of magnitude, however, in those simulations the landscape sampled either exemplified dynamics of too short or too long of dynamics. For 1FKB, a large penalty was required due to the significantly longer folding time, the larger penalty resulted in a appropriate energy landscape sampling. The protein systems considered here were all chosen because their experimental folding times were determined at near room temperature conditions.

In the simulations, the initial protein configuration was determined by the protein database as the folded configuration. The system contained no explicit solvent for these simulations as the energy landscape of the protein alone was of interest. The metadynamics simulations were run for up to 4 hours on our campus cluster with. The box size for each protein varied based on the size of the protein system. The initial configuration of the proteins and their associated experimental folding times are contained in Figure 5.2. The figure is arranged in ascending order of the folding times. In addition to the twelve proteins simulated in [6], an additional three proteins were simulated with all-atom metadynamics. the protein simulations were performed with the OPLSAA force field. The force field parameters were determined from the Universal Force Field (UFF) used commonly for protein systems.

Figure 5.3 shows the resulting energy landscapes from the all-atom metadynamics simulations of the fifteen protein systems. Because the initial configuration was determined from experimental configurations, the initial minimization of energy was ignored for each proteins landscape. The proteins were arranged in

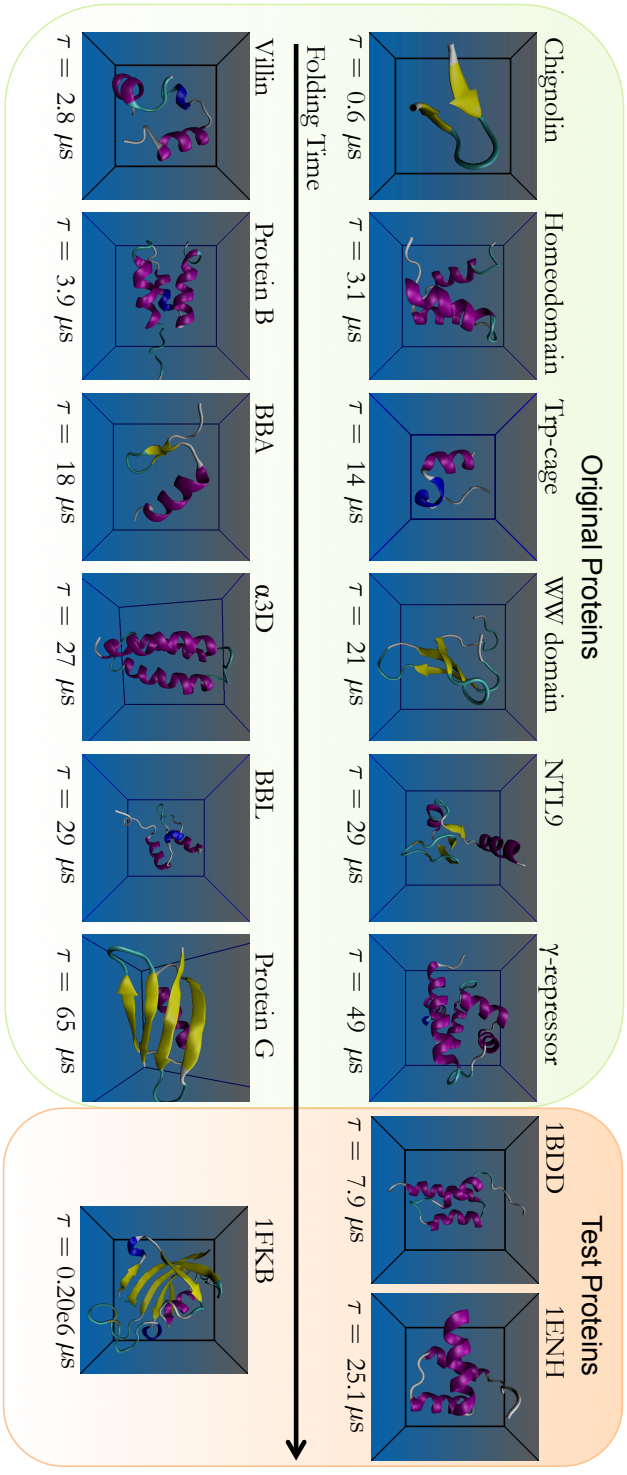

Figure 5.2: Proteins simulated with all-atom Metadynamics. The original proteins were the focus of the molecular dynamics study provided in [6]. The test proteins were additional proteins outside the scope of [6] but with experimental determined folding times. The proteins are ordered by their folding time.

same order as 5.2. First, one sees that in general, proteins with longer folding times have landscapes with larger scale energies.

To extract statistical information about the landscape, each landscape was divided into several equal sized portions, as shown in Figure 5.4. Each region is assumed to be a statistical representation of the energy landscape for the protein system. Each region was analyzed for the largest barrier separating two configurational basins, which were then averaged to produce the estimated activation barrier shown in Figure 5.3. This is a crude approximation of the energy landscape barrier of the proteins considered, and far more information can still be gleaned from these data sets

Figure 5.5 shows the experimentally determined protein folding times as a function of the activation energy determined from the all-atom Metadynamics simulations. First, as a note, based on the simulations in [6], we trust the force field used to estimate the timescales of the dynamics of these protein systems, as they found that using extremely long molecular dynamics simulations were able to reproduce the folding time of fast folding proteins systems. Figure 5.5 shows that there is a roughly linear relationship between the experimental folding time and the average activation barrier determined from the energy landscape sampled by all-atom metadynamics on a semi log scale. Because all of the proteins folding time was determined at nearly the same temperature conditions, we can gather that this linear correlation is a result of the larger barriers on the potential energy landscape for systems with longer dynamic behaviors. From this we can gather that the folding time and the landscape are correlated by

$$\tau \propto \exp(E_a) \tag{5.4}$$

The intercept when the data is fit with a line is around 109 ns. We are coining this the intrinsic protein folding time. Meaning, even if the protein has no barrier preventing folding and unfolding, the protein will still undergo a dynamic time of 109 ns on average. This value is in agreement with the reported "protein speed limit" of N/100 μs where N is the number of residues found by researchers that correlated the experimental protein folding time with the number of residues in the protein. They found that larger proteins had longer folding times, and that even a small protein with 10 residues would have a "speed limit" or minimum folding time of 100 ns [99]. While not tested here, one could infer then a correlation between the number of residues and the energy landscape barrier heights, that larger proteins undergo larger energy barrier dynamics. Further, Figure 5.5 shows that all-atom metadynamics can produce landscapes for proteins with folding times well beyond the timescales achievable by molecular dynamics simulation.

5.4 Summary

In this chapter, two methods considered for computing the timescale of the energy landscape was discussed. The first method involves assuming that the energy landscape can be mapped to time based on the Arrhenius nature of the activated process of a system evolving from one energy basin over a energy barrier to a new energy basin. This method was displayed on two types of systems, one a crystal former and one a glass former. The two landscapes are in juxtaposition of each other once mapped based on their energy barrier information, Maxwell relaxation time, and temperature. The glassy system confirms that on the energy landscape, the system gets trapped in energy minimums for extended periods of time before activating over large barriers and sampling new regions of the landscape, also known as arrest.

The second method involves comparing the landscape to known experimental data about the system. This manner is displayed by comparing a series of 15 protein systems energy landscapes sampled by all-atom metadynamics and comparing to the known experimental folding time. This method showed, at least for ordered proteins, that the size of the estimated activation barrier from the energy landscape is proportional to the log of the folding time determined from experiments. This method showed that the use of the energy landscape sampling method can provide barrier information, and therefore estimate the folding time, even for large proteins with folding times in macroscopic timescale of subseconds, well well beyond the longest molecular dynamics simulations can provide.

As an important note, in this chapter, the two methods were applied to all-atom Metadynamics simulations, however, as the energy landscape sampled should be unique to a physical system, the method of sampling the energy landscape should provide statistically equivalent information regardless of the method of sampling the landscape. Thus, the methods discussed here, and the methods used in other published works, should be applicable to both all-atom Metadynamics and Ascent Dynamics, and all other methods for sampling the energy landscape. With that said, the methods here provide possible methods for estimating the time scale of the phenomena under study, however, a great deal of future work is needed in this area to determine an ideal method for extracting the time information directly from the energy landscape simulations. For now, we consider energy sampling methods useful for gaining insights to the dynamics of material systems, however, should not be used for directly computing the exact time of the phenomena until more work is performed in this area.

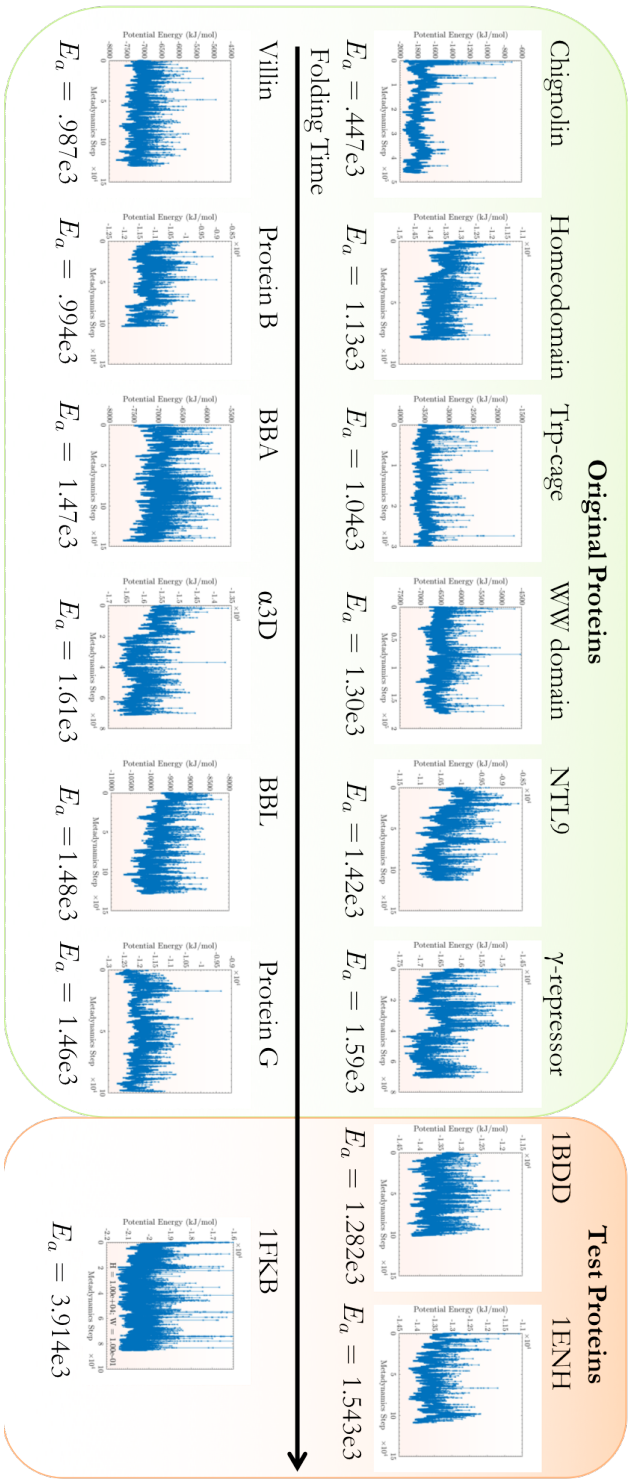

Figure 5.3: Energy Landscapes sampled from the proteins simulated with all-atom Metadynamics. The original proteins were the focus of the molecular dynamics study provided in [6]. The test proteins were additional proteins outside the scope of [6] but with experimental determined folding times. The proteins are ordered by their folding time listed in Figure 5.2.

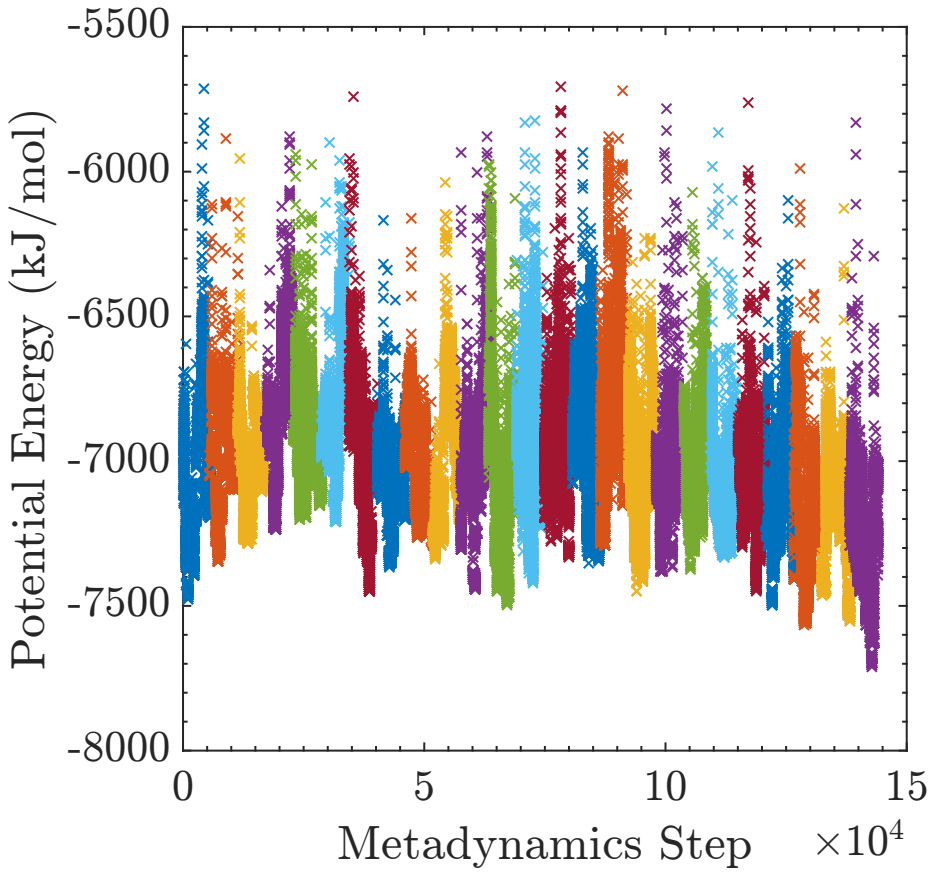

Figure 5.4: Example of the energy landscape dissected into equal portions to perform statistical analysis of the average energy barrier sampled on the landscape. Each color represents one of the many sections of the landscape.

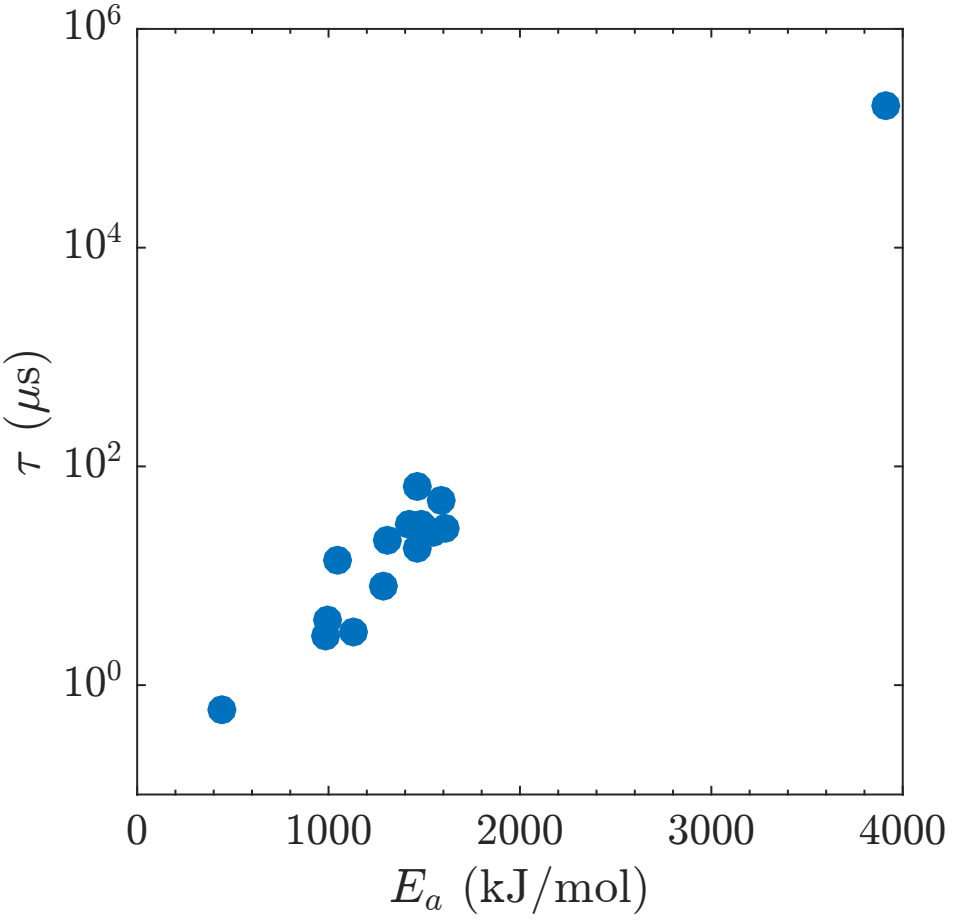

Figure 5.5: Figure of the experimentally determined protein folding times as a function of the activation energy determined from the all-atom Metadynamics simulations.

Chapter 6

Summary and Future Works

6.1 Summary

Some of the most interesting phenomena in material science occur out of equilibrium, over long timescales, or require an extremely rare event as an initiation, for example phase changes, chemical reactions, vitrification, protein folding, etc. The commonality of these interesting phenomena is the length and time scale on which they occur. Particularly, the origin of their understanding is on the atomic or molecular scale while requiring observational timescales beyond milliseconds to capture the entire process. However, most computational and experimental techniques struggle to observe this length and time scale. For example, the most common method for studying atomic behavior, molecular dynamics, stretches only into the high microseconds on the largest computers. On the other hand, experiments can easily capture long timescales on the macroscopic length scale, but methods to capture long timescales on the atomic scale are rare.

This thesis focuses on developing and implementing computational methods to allow for the study of long timescale phenomena from the molecular and atomic level. To approach this problem of developing methods for simulating long timescales of material systems, this thesis relies on the energy landscape framework which has found novel use in explaining schematically the dynamics and structural behavior of a range of material systems.

The potential energy landscape framework is used as a foundation on which to develop the methods to capture the long timescale phenomena of atomic systems. The potential energy landscape framework treats structural information as energy basins, and dynamical information as energy barriers, which separate basins of attraction. The framework has provided novel theories into the physics of these systems; however, few methods exist to experimentally or computationally prove or compute the energy landscape of a system.

First, we cover our previously implemented all-atom metadynamics method. The formulation of the method is displayed, in which, a system is driven out of basins of attraction by history-dependent potential energy penalty functions. After application of several penalties, a system is biased out of basins and over

barriers of the energy landscape. Based on the height and width of the energy penalty function, different scales of the landscape can be easily sampled. For example, if short timescale, or small barrier and local landscape information, is of interest, a small penalty is used to sample local and low energy information of the landscape. Comparatively, for long timescale information, large penalties can be used to sample large barrier information while ignoring small barrier information. The utility of the metadynamics method is shown on a model liquid to study nucleation and crystal growth, a monoatomic Lennard-Jones Argon system is chosen. The simulation was previously shown to generate a trajectory from a liquid system to a perfect FCC crystal system. In this thesis, the critical nucleus size was further studied and shown to display a spectrum of structural order and non-uniform shapes. We found from the all-atom metadynamics simulation that the nucleus site for crystal growth was non-spherical and had layers of low order between the nucleus and the liquid phase. As a result, we assume that a large source of error in the classical nucleation approximations from molecular dynamics simulations is the assumption of a spherical nucleus site with nearly perfect order, resulting in an inaccurate approximation to the interface energy barrier between the nucleus and the liquid phase. We then propose an alternative method of approximating the critical nucleus barrier and size based on the sampled energy landscape. We believe this is a novel approach to simulating the nucleation and crystal growth process, and can provide new insights to the mechanisms involved in crystallization of systems.

However, despite the success of all-atom metadynamics for the simulation of several phenomena, metadynamics has one major glaring short-coming, it's computational demand, as the method increases in computational cost for every penalty applied. Thus, second in this thesis, a new method for advanced sampling is proposed, Varied Steepness Ascent Dynamics (Ascent Dynamics), as a potential solution to study long timescale phenomena with less computational cost as metadynamics. In Ascent Dynamics, based on local information of the current system configuration determined from the Hessian, the system is evolved towards transition states by a force modified by multiple directions of lowest curvatures, akin to other surface walking methods. Physically, this results in the system overcoming complex transition states while avoiding non-physical events on the landscape. Previous methods focused on systems that were easily defined by a single collective variable. Here, Ascent Dynamics was developed to sample energy landscapes with complex transition states on hyper-dimensional energy landscapes, such as complex liquids or proteins. Ascent Dynamics' computational cost is constant over the simulation, thus allowing for more efficient sampling of the landscape over the simulation time. The method is verified on several test problems, validated on a simple vacancy diffusion problem, and then applied to a model material system to show the utility of the new method, based on the two dimensional polydisperse potential. The method is also shown to be successful on three dimensional systems. The method is developed into a package in the programming language Julia

in order to take advantage of Julia's fast linear algebra libraries, and is accompanied by several different force-fields. In this thesis, the method is developed, implemented, and produced into a package for further use to study several model systems. Ideally, future work with this method will unveil novel understandings of materials on long timescales from a molecular and atomic level.

Lastly, a brief discussion on how to compare the landscape to time is provided. Two methods studied in this work were shown. The first involves mapping the landscape to time based on the Arrhenius relationship between the transition state barrier energy and the relaxation time of the system. This method provides a statistically likely pathway along the energy landscape in terms of time. The relaxation time used can be the Maxwell relaxation time, the time of the ballistic to non-ballistic regime of the mean squared displacement, or any other characteristic relaxation time assumed to represent the phenomena sampled on the energy landscape.

The second method for estimating the time scale of the landscape involves comparing the landscape to experimentally known time scales. In this manner, a series of fifteen ordered proteins were simulated with all-atom Metadynamics, all of which have known folding times from experiments. An average energy barrier was then computed by dissecting the landscape into equal sized portions assumed to be representative of the landscape and computing the largest barrier separating two configurational basins of the landscape. This average energy barrier for each protein was shown to be linearly correlated with the log of the folding time determined by experiments. More work is required in this project to deduce exactly the origin of the average largest energy barrier of the landscape correlating well with the folding time. However, this method shows that indeed the larger the energy barrier the larger the characteristic dynamic time scale, at least in the case of protein systems. These two method allow us to confirm that the phenomena we are sampling with these methods is indeed occurring on long timescales outside the scope of molecular dynamics simulations.

In conclusion, in this thesis we developed and implemented two flavors of energy landscape sampling methods. The first all-atom metadynamics is an extension of the metadynamics force biasing methods, and the second, Ascent Dynamics, is a new surface walking method for sampling complex transition states of material systems. By comparing the landscape to experimental folding times of proteins and using the Maxwell relaxation time, we showed that these landscapes are producing phenomena on long timescales, and can be used to provide new insights to atomic phenomena difficult or impossible to study with molecular dynamics simulations. In the remaining portions, future work for both methods will be discussed.

6.2 Future Work

In this section various directions of future work are proposed.

6.2.1 Metadynamics Future Work

Determine Correlation Functions From Metadynamics

As discussed in Chapter 5, the landscape can be extended to time via Arrhenius relationships between the energy barrier height, temperature and a characteristic relaxation time. One direction of future work would be to use this landscape based on time to compute correlation functions.

Once we have extended the all-atom metadynamics simulations to time, we can use our landscape to compute long time quantities akin to a molecular dynamics simulation. After mapping to temperature and calculating the time, we can then use the trajectory and the configurations to compute quantities such as the mean squared displacement ($\langle r^2 \rangle(t)$), the pair distribution function ($g(r)$), the intermediate scattering functions ($F_s(k,t)$, $F(k,t)$), etc. Each are defined as

$$\langle r^2(t) \rangle = \frac{1}{N} \left\langle \sum_{l=1}^{N} |\mathbf{r}_l(t) - \mathbf{r}_l(0)|^2 \right\rangle \tag{6.1}$$

$$g(r) = \frac{1}{4\pi r^2 dr \rho N} \left\langle \sum_{l \neq l'} \delta(\mathbf{r} - |\mathbf{r}_l - \mathbf{r}_{l'}|) \right\rangle. \tag{6.2}$$

$$F_s(k,t) = \frac{1}{N} \left\langle \sum_{l=1}^{N} \exp\left\{-i\mathbf{k} \cdot [\mathbf{r}_l(t) - \mathbf{r}_l(0)]\right\} \right\rangle. \tag{6.3}$$

$$F(k,t) = \frac{1}{N} \left\langle \sum_{l=1}^{N} \sum_{l'=1}^{N} \exp\left\{-i\mathbf{k} \cdot [\mathbf{r}_l(t) - \mathbf{r}_{l'}(0)]\right\} \right\rangle. \tag{6.4}$$

where N is the number of atoms, $\mathbf{r}$ is the atomic coordinates, $\mathbf{k}$ is the wave vector [100, 61]. These quantities can help provide us insight to the dynamics of the system, and allows us to compare to experiments and results of molecular dynamics.

One caveat would be that because the landscape only contains barrier information, short time scale information (i.e. ballistic information of the mean squared displacement) would be inaccessible without accompanying this analysis with some molecular dynamics simulations on short time scales, or without determining a method for determining short timescale information from the shape or depth of the metastable basins.

Non-constant Density Metadynamics

Currently, our implementation of Metadynamics is only constant number, N, constant volume, V, or constant density. However, phase transitions are known to undergo a change in density as well. While several previous works have also studied nucleation under NVE or NVT, ideally, phase change should be considered under NPT or NPE. Thus, future work should include implementation of a constant pressure all-atom metadynamics. This however is not trivial, as pressure is not well defined in a all-atom metadynamics simulation, or any advanced sampling methods for that matter.

One method for simulating without constant density would be to add the density as a potential degree of freedom in the sampling algorithm. This could be done by also added the density to the variables penalized by the penalty functions or by adding the density to the Hessian matrix computation. In this manner, the density would also fluctuate as the system climbs the energy barriers and relaxes to new minimums, which would allow the density to adapt as the structure of the system evolves. As a direction of future work, this would be a novel addition to the advanced sampling community that as far as the authors are aware has not been implemented prior.

Protein Systems

Because both metadynamics and Ascent Dynamics use steepest descent to relax the system to new minimum states, the algorithms are biased towards minimizing the system to lower minimum states. This is exemplified by the nucleation simulation. Instead of sampling high disordered minimum states, all atom metadynamics simulations of systems that can order prioritize lowest energy minimums of the landscape if they can be found. As a result, a unique use of all atom metadynamics or Ascent Dynamics is to continue the protein simulation work by studying proteins with unknown folded states.

Figure 6.1 shows an example of how a metadynamics simulation could begin with a disordered protein and by sampling the landscape with a steepest descent for seeking minimums, the simulation would converge on a potentially folded state of the protein. This could further be expanded to categorize intrinsically disordered proteins from ordered proteins. This direction of work could be useful in the biology community for determining native states of new proteins and categorizing proteins based.

6.2.2 Ascent Dynamics Method Improvements

Future work for the Ascent Dynamics are mainly focused on how to further improve the algorithm or implementation of the method to further increase the efficiency or robustness of the method.

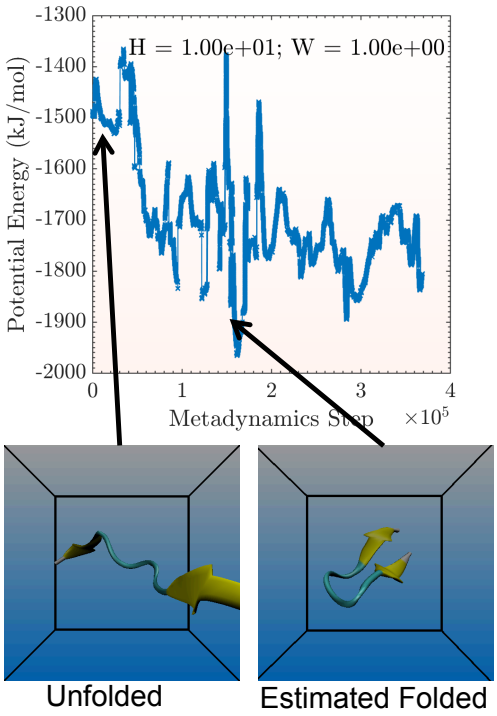

Figure 6.1: Energy Landscape sampled by all-atom metadynamics for the protein trp-cage while beginning from a disordered state. This figure is an example of how one might be able to use all-atom metadynamics or Ascent Dynamics to predict native states of proteins, or native states/transition states of other macromolecules. because advanced sampling methods tend to bias the system to lower energy states, these methods could be used to help quickly elucidate configurations of new macromolecules.

BFGS

While the finite difference scheme allows us to avoid the diagonalization of the Hessian matrix, computation of the Hessian matrix can still be expensive if the analytical form is unknown. Thus, one method that is widely used in minimization and optimization schemes is BFGS. In this scheme, the Hessian matrix is approximated based on the change of the function from one step to the next. From this change and the previous steps change, the Hessian matrix is approximated and then used to build a more optimal search direction.

It has been shown that using conjugate gradient method can increase the efficiency of sampling saddle points with the Locally Optimal Conjugate Gradient Method [101]

Thus, one direction of future work is to use BFGS for the ascents to approximate the Hessian matrix. This would allow for an N^2 calculation of the Hessian matrix when the analytical form is unknown. When the analytical form is unknown, calculation of the Hessian matrix is generally near N^3, while it is N^2 when

the analytical form is known [102]. Initial tests of this scheme showed promising results. However, there were some occasional stability issues. It appears that BFGS is more accurate at approximating the Hessian matrix near minimum states than near transition states. With some further investigation, this could however be a viable method for computationally calculating the Hessian matrix when the second derivatives are unknown.

Large Scale Implementation

While the Ascent Dynamics method has been developed as a stand alone package in Julia, as mentioned in the previous section, the limitation of stand alone implementations is the need to program ever potential desired to be studied. A direction of future work is to implement the Ascent Dynamics method into a large scale MD package such as we have previously done with all atom metadynamics into GROMACS. An ideal package for adding Ascent Dynamics could be GROMACS, LAMMPS, or NAMD. The advantage of this direction of future work is that then users can take advantage of the extensive potential library available in these large scale MD packages, rather than having to develop a new potential for every new system being considered.

Further, implementation into a large scale MD package allows for easy implementation of parallelization schemes, neighbor listing, and other computational improvements.

Another method to potentially parallelize Ascent Dynamics involves partitioning of the Hessian matrix. Particularly, the Hessian matrix for a real system is sparse in many elements. Specifically, atoms that are beyond a certain cut-off distance from one another. Thus, a direction of future work would be to utilize neighbor listing to build a smaller Hessian matrix for each atom. Then, rather than one large Hessian matrix, instead, there will be N smaller Hessian matrices (of the size of the neighbor list). Solving each of these smaller Hessian matrices will be less expensive than solving the one large Hessian matrix, and easier to distribute over computer nodes. In this sense, the total potential energy landscape will actually be partitioned into several sub landscapes, as proposed by [103]. After solving these simpler Hessian matrices, a modified force can be recomposed from the eigenvectors. Tests of this has shown that systems still evolve to transition states that are transition states on the complete landscape. However, further work is required to verify that these results are statistically equivalent to Ascent Dynamics on the complete Hessian matrix. A similar method for decomposing and following the lowest determined eigenvector was shown in [40]

6.2.3 Ascent Dynamics Usage

One direction of future work is to apply Ascent Dynamics to several other systems of interest. The package was developed with additional potentials other than those presented here. For example, a future direction of work is to use Ascent Dynamics and the Lennard-Jones potential to study nucleation and crystal growth, similar to the work presented in Chapter 2. Additionally, the package includes binary Lennard-Jones as a potential model liquid, and the two dimensional water model MB-water. These additional potentials are derived and demonstrated in Appendix B.

Appendix A

All-Atom Metadynamics Appendix

This work comes from [5], however, much of the considerations that were required in the implementation of Metadynamics were valuable considerations for implementation of AscentDynamics as well. This includes, how to account for finite precision rounding errors in the code, how to sample different scales of the landscape, how to prevent center of mass translation and rotations. Figure A.1 is included here to aid in the discussion of the differences between Metadynamics and AscentDynamics in sampling different scales of the energy landscape.

In metadynamics the two major user definable parameters are the height and width of the penalty functions. To study the height and width dependence of the potential energy penalty functions on the sampled energy landscape, the penalty height and width was varied for metadynamics simulations of a Kob-Andersen model liquid, as described in [104, 5], as shown in Figure A.1. Both the height and the width

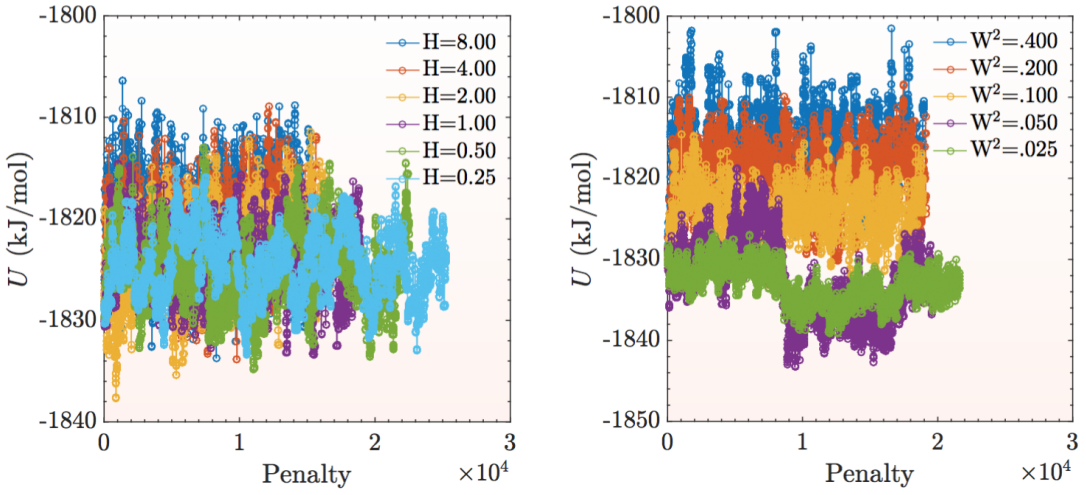

Figure A.1: Potential energy versus penalty number for various penalty function heights and widths. The left panel shows the effect of different penalty heights on the sampled energy landscape. The panel figure shows the effect of different penalty widths on the sampled energy landscape. For the width variation, the height of the barrier was fixed to 1 kJ/mol. For the height variation, the width squared was fixed to .1 nm^2. Adapted from [5]

affects the path along the potential energy landscape taken by the metadynamics method, as shown in Figure A.1, and thus, a balancing of the two parameters is essential to correctly sampling the energy landscape and the dynamics of interest. A full analysis of these parameters is performed in [5].

The metadynamics method described in Chapter 2 was implemented into the open-source molecular dynamics package GROMACS [7] in order to take advantage of the robust material force-field library available in the package. A more complete description of the implementation and development is in [5].

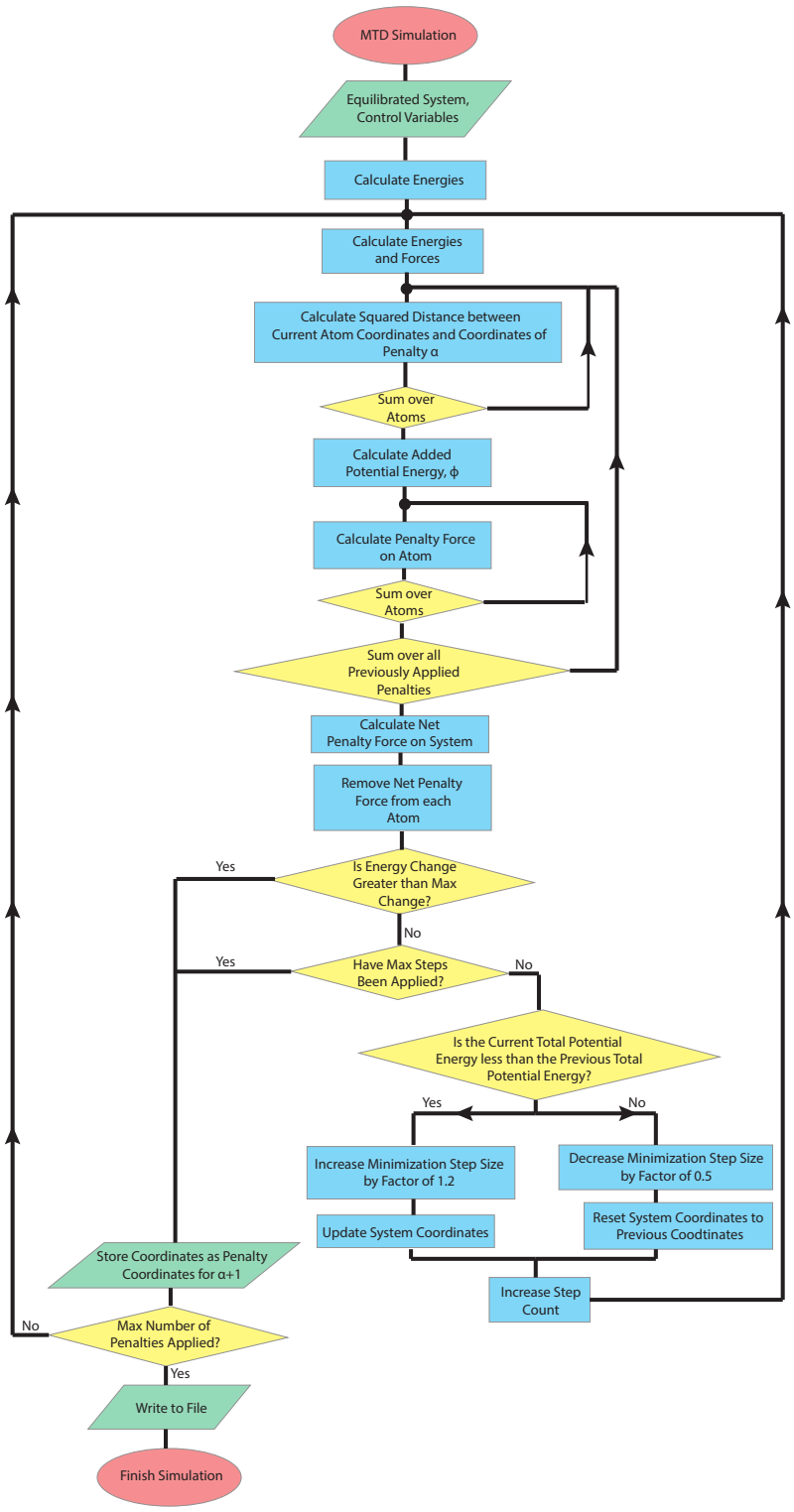

Figure A.2: A schematic flow chart of the all-atom metadynamics. The method was added to the open source package GROMACS [7] and hacked to allow for OpenMP parallelization [8]. Adapted from [5]

Appendix B

Varied Steepness Ascent Dynamics Appendix

B.1 Binary Lennard-Jones

Similar to the original Lennard-Jones potential, the potential of the binary Lennard-Jones system is [98]

$$U(\mathbf{r}) = \sum_i \sum_{j \neq i} 4\epsilon_{ij} \left[\left(\frac{\sigma_{ij}}{r_{ij}} \right)^{12} - \left(\frac{\sigma_{ij}}{r_{ij}} \right)^{6} \right] \tag{B.1}$$

where ϵ_{ij} and σ_{ij} is the potential depth and atom diameter based on the atom types i and j. This potential has a corresponding force of

$$\mathbf{F}_i = -\sum_{j \neq i} 4\epsilon_{ij} \left[\frac{12\sigma_{ij}^{12}}{r_{ij}^{14}} - \frac{6\sigma_{ij}^{6}}{r_{ij}^{6}} \right] \mathbf{r_{ij}} \tag{B.2}$$

and a hessian

$$H(\mathbf{r}) = \begin{bmatrix} \frac{\partial^2 U}{\partial x_1 \partial x_1} & \frac{\partial^2 U}{\partial x_1 \partial y_1} & \cdots & \frac{\partial^2 U}{\partial x_1 \partial y_n} \\ \frac{\partial^2 U}{\partial y_1 \partial x_1} & \frac{\partial^2 U}{\partial y_1 \partial y_1} & \cdots & \frac{\partial^2 U}{\partial y_1 \partial y_n} \\ \vdots & \vdots & \ddots & \vdots \\ \frac{\partial^2 U}{\partial x_n \partial x_n} & \frac{\partial^2 U}{\partial x_n \partial y_1} & \cdots & \frac{\partial^2 U}{\partial y_n \partial y_n} \end{bmatrix} \tag{B.3}$$

where each tri-diagonal term is

$$H_{i,i}(\mathbf{r}) = \frac{\partial^2 U(\mathbf{r})}{\partial x_i \partial x_i} = 4\epsilon_{ij} \sum_{j \neq i} \left[\left(\frac{168\sigma_{ij}^{12}}{r_{ij}^{16}} - \frac{48\sigma_{ij}^{6}}{r_{ij}^{8}} \right) (x_j - x_i)^2 - \left(\frac{12\sigma^{12}}{r_{ij}^{14}} - \frac{6\sigma^{6}}{r_{ij}^{6}} \right) \right] \tag{B.4}$$

$$H_{i,i+1}(\mathbf{r}) = \frac{\partial^2 U(\mathbf{r})}{\partial x_i \partial y_i} = 4\epsilon_{ij} \sum_{j \neq i} \left[\left(\frac{168\sigma_{ij}^{12}}{r_{ij}^{16}} - \frac{48\sigma_{ij}^{6}}{r_{ij}^{8}} \right) (x_j - x_i)(y_j - y_i) \right] \tag{B.5}$$

$$H_{i+1,i}(\mathbf{r}) = \frac{\partial^2 U(\mathbf{r})}{\partial y_i \partial x_i} = 4\epsilon_{ij} \sum_{j \neq i} \left[\left(\frac{168\sigma_{ij}^{12}}{r_{ij}^{16}} - \frac{48\sigma_{ij}^{6}}{r_{ij}^{8}} \right) (x_j - x_i)(y_j - y_i) \right] \tag{B.6}$$

$$H_{i+1,i+1}(\mathbf{r}) = \frac{\partial^2 U(\mathbf{r})}{\partial y_i \partial y_i} = 4\epsilon_{ij} \sum_{j \neq i} \left[\left(\frac{168\sigma_{ij}^{12}}{r_{ij}^{16}} - \frac{48\sigma_{ij}^{6}}{r_{ij}^{8}} \right) (y_j - y_i)^2 - \left(\frac{12\sigma^{12}}{r_{ij}^{14}} - \frac{6\sigma^{6}}{r_{ij}^{6}} \right) \right] \tag{B.7}$$

and the off diagonal terms are

$$H_{i,j}(\mathbf{r}) = \frac{\partial^2 U(\mathbf{r})}{\partial x_i \partial x_j} = -4\epsilon_{ij}\left[\left(\frac{168\sigma_{ij}^{12}}{r_{ij}^{16}} - \frac{48\sigma_{ij}^{6}}{r_{ij}^{8}}\right)(x_j - x_i)^2 - \left(\frac{12\sigma^{12}}{r_{ij}^{14}} - \frac{6\sigma^{6}}{r_{ij}^{6}}\right)\right] \tag{B.8}$$

$$H_{i,j+1}(\mathbf{r}) = \frac{\partial^2 U(\mathbf{r})}{\partial x_i \partial y_j} = -4\epsilon_{ij}\left[\left(\frac{168\sigma_{ij}^{12}}{r_{ij}^{16}} - \frac{48\sigma_{ij}^{6}}{r_{ij}^{8}}\right)(x_j - x_i)(y_j - y_i)\right] \tag{B.9}$$

$$H_{i+1,j}(\mathbf{r}) = \frac{\partial^2 U(\mathbf{r})}{\partial y_i \partial x_j} = -4\epsilon_{ij}\left[\left(\frac{168\sigma_{ij}^{12}}{r_{ij}^{16}} - \frac{48\sigma_{ij}^{6}}{r_{ij}^{8}}\right)(x_j - x_i)(y_j - y_i)\right] \tag{B.10}$$

$$H_{i+1,j+1}(\mathbf{r}) = \frac{\partial^2 U(\mathbf{r})}{\partial y_i \partial y_j} = -4\epsilon_{ij}\left[\left(\frac{168\sigma_{ij}^{12}}{r_{ij}^{16}} - \frac{48\sigma_{ij}^{6}}{r_{ij}^{8}}\right)(y_j - y_i)^2 - \left(\frac{12\sigma^{12}}{r_{ij}^{14}} - \frac{6\sigma^{6}}{r_{ij}^{6}}\right)\right] \tag{B.11}$$

In the Ascent Dynamics package, the first A atoms are of type A, and the remaining particles are of type B. Ordering the atoms in this way simplified looping of the atoms.

B.2 Mercedes Benz Water Model

This model has been proposed as a two dimensional potential with a single point to model water systems. The name is derived from the atom's appearance similarity to a Mercedes Benz logo [105, 106].

The potential is defined as

$$U(\mathbf{r}_{ij}) = U_{LJ}(\mathbf{r}_{ij}) + U_{HB}(\mathbf{r}_{ij}) \tag{B.12}$$

where LJ is the Lennard-Jones component and the HB is the hydrogen bond component.

$$U_{LJ}(\mathbf{r}_{ij}) = 4\epsilon_{LJ}\left(\left(\frac{\sigma_{LJ}}{r_{ij}}\right)^{12} - \left(\frac{\sigma_{LJ}}{r_{ij}}\right)^{6}\right) \tag{B.13}$$

where the standard Lennard-Jones parameters are used, $\epsilon_{LJ} = -0.1\epsilon_{HB}$, $\sigma_{LJ} = 0.7 r_{HB}$, $\sigma_r = \sigma_\theta = 0.085$.

$$U_{HB}(\mathbf{x}_i, \mathbf{x}_j) = \sum_{k,l=1}^{3} U_{HB}^{kl}(r_{ij}, \theta_i, \theta_j) \tag{B.14}$$

where k and l are indexes for the three arms of atom i and j respectively, and θ is the angle of the atom measured from horizontal.

$$U_{HB}^{kl}(r_{ij}, \theta_i, \theta_j) = \epsilon_{HB} G(r_{ij} - r_{HB}) G(i_k \cdot \mathbf{u}_{ij} - 1) G(j_l \cdot \mathbf{u}_{ij} + 1) \tag{B.15}$$

where $\epsilon_{HB} = -1$, $r_{HB} = 1$, i_k is the direction of the arm k of atom i or $i_k = [\cos(\theta_k), \sin(\theta_k)]$, where θ_k is

equal to $\theta_i + k * \frac{2\pi}{3}$, and

$$G(x) = \exp\left(-\frac{x^2}{2\sigma^2}\right) \tag{B.16}$$

The first derivatives are as follows

$$\frac{\partial U(\mathbf{r}_{ij})}{\partial x} = \frac{\partial U_{LJ}(\mathbf{r}_{ij})}{\partial x} + \frac{\partial U_{HB}(\mathbf{r}_{ij})}{\partial x} \tag{B.17}$$

where the first derivative in y can be deduced by replacing x with y.

$$\frac{\partial U_{LJ}(\mathbf{r}_{ij})}{\partial x} = 4\epsilon_{LJ}\left[\frac{12\sigma_{LJ}^{12}}{r_{LJ}^{14}} - \frac{6\sigma_{LJ}^{6}}{r_{ij}^{6}}\right](x_j - x_i) \tag{B.18}$$

and

$$\begin{aligned}\frac{\partial U_{HB}(\mathbf{r}_{ij})}{\partial x} =& \epsilon_{HB}\frac{\partial G(r_{ij} - r_{HB})}{\partial x}G(i_k \cdot \mathbf{u}_{ij} - 1)G(j_l \cdot \mathbf{u}_{ij} + 1) && \text{(B.19)}\\ &+ \epsilon_{HB}G(r_{ij} - r_{HB})\frac{\partial G(i_k \cdot \mathbf{u}_{ij} - 1)}{\partial x}G(j_l \cdot \mathbf{u}_{ij} + 1) && \text{(B.20)}\\ &+ \epsilon_{HB}G(r_{ij} - r_{HB})G(i_k \cdot \mathbf{u}_{ij} - 1)\frac{\partial G(j_l \cdot \mathbf{u}_{ij} + 1)}{\partial x} && \text{(B.21)}\end{aligned}$$

where

$$\frac{\partial G(r_{ij} - r_{HB})}{\partial x} = \exp\left(-\frac{(r_{ij} - r_{HB})^2}{2\sigma_R^2}\right)(r_{ij} - r_{HB})\frac{1}{\sigma_R^2}(x_j - x_i)\frac{1}{r_{ij}} \tag{B.22}$$

$$\frac{\partial G(i_k \cdot \mathbf{u}_{ij} - 1)}{\partial x} = \exp\left(-\frac{(i_k \cdot \mathbf{u}_{ij} - 1)^2}{2\sigma_\theta^2}\right)(i_k \cdot \mathbf{u}_{ij} - 1)\frac{1}{\sigma_\theta^2}(i_k \cdot \mathbf{u}'_{ij}) \tag{B.23}$$

$$\frac{\partial G(j_l \cdot \mathbf{u}_{ij} + 1)}{\partial x} = \exp\left(-\frac{(j_l \cdot \mathbf{u}_{ij} + 1)^2}{2\sigma_\theta^2}\right)(j_l \cdot \mathbf{u}_{ij} + 1)\frac{1}{\sigma_\theta^2}(j_l \cdot \mathbf{u}'_{ij}) \tag{B.24}$$

The derivatives for y can be inferred from the above definitions

$$\frac{\partial U(\mathbf{r}_{ij})}{\partial \theta} = \frac{\partial U_{HB}(\mathbf{r}_{ij})}{\partial \theta} \tag{B.25}$$

$$\frac{\partial U_{HB}(\mathbf{r}_{ij})}{\partial \theta} = \epsilon_{HB}G(r_{ij} - r_{HB})\frac{\partial G(i_k \cdot \mathbf{u}_{ij} - 1)}{\partial \theta}G(j_l \cdot \mathbf{u}_{ij} + 1) \tag{B.26}$$

where

$$\frac{\partial G(i_k \cdot \mathbf{u}_{ij} - 1)}{\partial \theta} = \exp\left(-\frac{(i_k \cdot \mathbf{u}_{ij} - 1)^2}{2\sigma_\theta^2}\right)(i_k \cdot \mathbf{u}_{ij} - 1)\frac{1}{\sigma_\theta^2}(i'_k \cdot \mathbf{u}_{ij}) \tag{B.27}$$

where

$$i'_k = [-\sin(\theta), \cos(\theta)] \tag{B.28}$$

B.3 3-D polydisperse and Lennard-Jones

For the three dimensional implementation of Lennard-Jones and polydisperse, the equations for the potential and the force remain the same, however now, $\mathbf{r} = [x_i - x_j, y_i - y_j, z_i - y_j]$. The hessian becomes

$$H(\mathbf{r}) = \begin{bmatrix} \frac{\partial^2 U}{\partial x_1 \partial x_1} & \frac{\partial^2 U}{\partial x_1 \partial y_1} & \frac{\partial^2 U}{\partial x_1 \partial z_1} & \cdots & \frac{\partial^2 U}{\partial x_1 \partial z_n} \\ \frac{\partial^2 U}{\partial y_1 \partial x_1} & \frac{\partial^2 U}{\partial y_1 \partial y_1} & \frac{\partial^2 U}{\partial y_1 \partial z_1} & \cdots & \frac{\partial^2 U}{\partial y_1 \partial z_n} \\ \frac{\partial^2 U}{\partial z_1 \partial x_1} & \frac{\partial^2 U}{\partial z_1 \partial y_1} & \frac{\partial^2 U}{\partial z_1 \partial z_1} & \cdots & \frac{\partial^2 U}{\partial z_1 \partial z_n} \\ \vdots & \vdots & \ddots & \vdots & \\ \frac{\partial^2 U}{\partial z_n \partial x_1} & \frac{\partial^2 U}{\partial z_n \partial y_1} & \frac{\partial^2 U}{\partial z_n \partial z_1} & \cdots & \frac{\partial^2 U}{\partial z_n \partial z_n} \end{bmatrix} \tag{B.29}$$

where for polydisperse the terms become

$$\begin{aligned} H_{i,i}(\mathbf{r}) = \frac{\partial^2 U(\mathbf{r})}{\partial x_i \partial x_i} = \sum_{j \neq i} & v_0 n(n+2) \frac{\sigma_{ij}^n}{r^{n+4}} (x_i - x_j)^2 + 8c_2 \frac{1}{\sigma_{ij}^4} (x_i - x_j)^2 \\ & - v_0 n \frac{\sigma_{ij}^n}{r^{n+2}} + 2c_1 \frac{1}{\sigma_{ij}^2} + 4c_2 \frac{r^2}{\sigma_{ij}^4} \end{aligned} \tag{B.30}$$

$$\begin{aligned} H_{i,i+1}(\mathbf{r}) = H_{i+1,i}(\mathbf{r}) = \frac{\partial^2 U(\mathbf{r})}{\partial x_i \partial y_i} = \sum_{j \neq i} & v_0 n(n+2) \frac{\sigma_{ij}^n}{r^{n+4}} (x_i - x_j)(y_i - y_j) \\ & + 8c_2 \frac{1}{\sigma_{ij}^4} (x_i - x_j)(y_i - y_j) \end{aligned} \tag{B.31}$$

$$\begin{aligned} H_{i,i+2}(\mathbf{r}) = H_{i+2,i}(\mathbf{r}) = \frac{\partial^2 U(\mathbf{r})}{\partial x_i \partial z_i} = \sum_{j \neq i} & v_0 n(n+2) \frac{\sigma_{ij}^n}{r^{n+4}} (x_i - x_j)(z_i - z_j) \\ & + 8c_2 \frac{1}{\sigma_{ij}^4} (x_i - x_j)(z_i - z_j) \end{aligned} \tag{B.32}$$

$$\begin{aligned} H_{i+1,i+1}(\mathbf{r}) = \frac{\partial^2 U(\mathbf{r})}{\partial y_i \partial y_i} = \sum_{j \neq i} & v_0 n(n+2) \frac{\sigma_{ij}^n}{r^{n+4}} (y_i - y_j)^2 + 8c_2 \frac{1}{\sigma_{ij}^4} (y_i - y_j)^2 \\ & - v_0 n \frac{\sigma_{ij}^n}{r^{n+2}} + 2c_1 \frac{1}{\sigma_{ij}^2} + 4c_2 \frac{r^2}{\sigma_{ij}^4} \end{aligned} \tag{B.33}$$

$$\begin{aligned} H_{i+1,i+2}(\mathbf{r}) = H_{i+2,i+1}(\mathbf{r}) = \frac{\partial^2 U(\mathbf{r})}{\partial y_i \partial z_i} = \sum_{j \neq i} & v_0 n(n+2) \frac{\sigma_{ij}^n}{r^{n+4}} (y_i - x_j)(y_i - z_j) \\ & + 8c_2 \frac{1}{\sigma_{ij}^4} (y_i - y_j)(z_i - z_j) \end{aligned} \tag{B.34}$$

$$\begin{aligned} H_{i+2,i+2}(\mathbf{r}) = \frac{\partial^2 U(\mathbf{r})}{\partial z_i \partial z_i} = \sum_{j \neq i} & v_0 n(n+2) \frac{\sigma_{ij}^n}{r^{n+4}} (z_i - z_j)^2 + 8c_2 \frac{1}{\sigma_{ij}^4} (z_i - z_j)^2 \\ & - v_0 n \frac{\sigma_{ij}^n}{r^{n+2}} + 2c_1 \frac{1}{\sigma_{ij}^2} + 4c_2 \frac{r^2}{\sigma_{ij}^4} \end{aligned} \tag{B.35}$$

where i is a multiple of three from 0 to 3N-3. These terms are the tridiagonal terms of the matrix. The non-tridiagonal terms are defined as

$$\begin{aligned} H_{i,i}(\mathbf{r}) = \frac{\partial^2 U(\mathbf{r})}{\partial x_i \partial x_i} = &- v_0 n(n+2)\frac{\sigma_{ij}^n}{r^{n+4}}(x_i - x_j)^2 - 8c_2\frac{1}{\sigma_{ij}^4}(x_i - x_j)^2 \\ &+ v_0 n\frac{\sigma_{ij}^n}{r^{n+2}} - 2c_1\frac{1}{\sigma_{ij}^2} - 4c_2\frac{r^2}{\sigma_{ij}^4} \end{aligned} \tag{B.36}$$

$$\begin{aligned} H_{i,i+1}(\mathbf{r}) = H_{i+1,i}(\mathbf{r}) = \frac{\partial^2 U(\mathbf{r})}{\partial x_i \partial y_i} = &-v_0 n(n+2)\frac{\sigma_{ij}^n}{r^{n+4}}(x_i - x_j)(y_i - y_j) \\ &- 8c_2\frac{1}{\sigma_{ij}^4}(x_i - x_j)(y_i - y_j) \end{aligned} \tag{B.37}$$

$$\begin{aligned} H_{i,i+2}(\mathbf{r}) = H_{i+2,i}(\mathbf{r}) = \frac{\partial^2 U(\mathbf{r})}{\partial x_i \partial z_i} = &-v_0 n(n+2)\frac{\sigma_{ij}^n}{r^{n+4}}(x_i - x_j)(z_i - z_j) \\ &- 8c_2\frac{1}{\sigma_{ij}^4}(x_i - x_j)(z_i - z_j) \end{aligned} \tag{B.38}$$

$$\begin{aligned} H_{i+1,i+1}(\mathbf{r}) = \frac{\partial^2 U(\mathbf{r})}{\partial y_i \partial y_i} = &-v_0 n(n+2)\frac{\sigma_{ij}^n}{r^{n+4}}(y_i - y_j)^2 - 8c_2\frac{1}{\sigma_{ij}^4}(y_i - y_j)^2 \\ &+ v_0 n\frac{\sigma_{ij}^n}{r^{n+2}} - 2c_1\frac{1}{\sigma_{ij}^2} - 4c_2\frac{r^2}{\sigma_{ij}^4} \end{aligned} \tag{B.39}$$

$$\begin{aligned} H_{i+1,i+2}(\mathbf{r}) = H_{i+2,i+1}(\mathbf{r}) = \frac{\partial^2 U(\mathbf{r})}{\partial y_i \partial z_i} = &-v_0 n(n+2)\frac{\sigma_{ij}^n}{r^{n+4}}(y_i - x_j)(y_i - z_j) \\ &- 8c_2\frac{1}{\sigma_{ij}^4}(y_i - y_j)(z_i - z_j) \end{aligned} \tag{B.40}$$

$$\begin{aligned} H_{i+2,i+2}(\mathbf{r}) = \frac{\partial^2 U(\mathbf{r})}{\partial z_i \partial z_i} = &-v_0 n(n+2)\frac{\sigma_{ij}^n}{r^{n+4}}(z_i - z_j)^2 - 8c_2\frac{1}{\sigma_{ij}^4}(z_i - z_j)^2 \\ &+ v_0 n\frac{\sigma_{ij}^n}{r^{n+2}} - 2c_1\frac{1}{\sigma_{ij}^2} - 4c_2\frac{r^2}{\sigma_{ij}^4} \end{aligned} \tag{B.41}$$

where j is a multiple of three from 0 to 3N-3.

Three dimensional Lennard Jones can be easily inferred from the above derivation for 3-D polydisperse.

References

[1] P. J. Steinhardt, D. R. Nelson, M. Ronchetti, Bond-orientational order in liquids and glasses, Phys. Rev. B 28 (1983) 784–805. doi:10.1103/PhysRevB.28.784.

[2] Y. Wang, S. Teitel, C. Dellago, Melting of icosahedral gold nanoclusters from molecular dynamics simulations, The Journal of Chemical Physics 122 (21).

[3] S. Yang, Multiscale modeling of nanocomposites.
URL https://sites.google.com/site/mmfslab/research/multiscale-modeling-of-nanocomposites

[4] P. Debenedetti, F. Stillinger, Supercooled liquids and the glass transition, Nature 410 (6825) (2001) 259–267.

[5] N. P. Walter, Direct energy landscape sampling of the homogeneous nucleation and crystal growth of a model liquid, Master's thesis, University of Illinois (2016).
URL http://hdl.handle.net/2142/92804

[6] K. Lindorff-Larsen, S. Piana, R. O. Dror, D. E. Shaw, How fast-folding proteins fold, Science 334 (6055) (2011) 517–520. arXiv:https://science.sciencemag.org/content/334/6055/517.full.pdf, doi:10.1126/science.1208351.
URL https://science.sciencemag.org/content/334/6055/517

[7] E. Lindahl, B. Hess, D. van der Spoel, Gromacs 3.0: a package for molecular simulation and trajectory analysis, Molecular modeling annual 7 (8) 306–317. doi:10.1007/s008940100045.

[8] OpenMP Architecture Review Board, OpenMP application program interface version 3.0 (May 2008).

[9] M. D. Ediger, C. A. Angell, S. R. Nagel, Supercooled liquids and glasses, The Journal of Physical Chemistry 100 (31) (1996) 13200–13212. doi:10.1021/jp953538d.

[10] L. C. E. Struik, Physical aging in plastics and other glassy materials, Polymer Engineering & Science 17 (3) 165–173. arXiv:https://onlinelibrary.wiley.com/doi/pdf/10.1002/pen.760170305, doi:10.1002/pen.760170305.
URL https://onlinelibrary.wiley.com/doi/abs/10.1002/pen.760170305

[11] Y. W. Kwon, Multiphysics and Multiscale Modeling: Techniques and Applications, CRC Press, 2015.

[12] E. Weinan, Principles of multiscale modeling, Cambridge University Press, 2011.

[13] C. R. Weinberger, G. J. Tucker, Multiscale materials modeling for nanomechanics, Springer, 2016.

[14] M. Goldstein, Viscous liquids and the glass transition: A potential energy barrier picture, The Journal of Chemical Physics 51 (9) (1969) 3728–3739. doi:10.1063/1.1672587.

[15] F. H. Stillinger, T. A. Weber, Hidden structure in liquids, Phys. Rev. A 25 (1982) 978–989. doi:10.1103/PhysRevA.25.978.

[16] F. H. Stillinger, Relaxation and flow mechanisms in "fragile" glass-forming liquids, The Journal of Chemical Physics 89 (10) (1988) 6461–6469. doi:10.1063/1.455365.

[17] F. H. Stillinger, A topographic view of supercooled liquids and glass formation, Science 267 (5206) (1995) 1935–1939. doi:10.1126/science.267.5206.1935.

[18] F. Sciortino, Potential energy landscape description of supercooled liquids and glasses, Journal of Statistical Mechanics: Theory and Experiment 2005 (05) (2005) P05015.

[19] D. Wales, Energy landscapes: Applications to clusters, biomolecules and glasses, Cambridge University Press, 2003.

[20] G. Henkelman, G. Jóhannesson, H. Jónsson, Methods for Finding Saddle Points and Minimum Energy Paths, Springer Netherlands, Dordrecht, 2002, pp. 269–302. doi:10.1007/0-306-46949-9.
URL https://doi.org/10.1007/0-306-46949-9

[21] T. R. Jahn, S. E. Radford, The yin and yang of protein folding, FEBS Journal 272 (23) (2005) 5962–5970. doi:10.1111/j.1742-4658.2005.05021.x.

[22] C. L. Brooks, J. N. Onuchic, D. J. Wales, Taking a walk on a landscape, Science 293 (5530) (2001) 612–613. doi:10.1126/science.1062559.

[23] D. J. Wales, Decoding the energy landscape: extracting structure, dynamics and thermodynamics., Philosophical transactions. Series A, Mathematical, physical, and engineering sciences 370 (1969) (2012) 2877–99. doi:10.1098/rsta.2011.0208.

[24] D. Quigley, P. M. Rodger, Metadynamics simulations of ice nucleation and growth, Journal of Chemical Physics 128 (15). doi:10.1063/1.2888999.

[25] A. Kushima, X. Lin, J. Li, J. Eapen, J. C. Mauro, X. Qian, P. Diep, S. Yip, Computing the viscosity of supercooled liquids., The Journal of chemical physics 130 (22) (2009) 224504. doi:10.1063/1.3139006.

[26] A. Kushima, X. Lin, J. Li, X. Qian, J. Eapen, J. C. Mauro, P. Diep, S. Yip, Computing the viscosity of supercooled liquids. II. Silica and strong-fragile crossover behavior., The Journal of chemical physics 131 (16) (2009) 164505. doi:10.1063/1.3243854.

[27] P. Crowther, F. Turci, C. P. Royall, The nature of geometric frustration in the kob-andersen mixture, The Journal of Chemical Physics 143 (4) (2015) 044503. doi:10.1063/1.4927302.

[28] E. J. Bylaska, J. Q. Weare, J. H. Weare, Extending molecular simulation time scales: Parallel in time integrations for high-level quantum chemistry and complex force representations, The Journal of Chemical Physics 139 (7) (2013) 074114. arXiv:https://doi.org/10.1063/1.4818328, doi:10.1063/1.4818328.
URL https://doi.org/10.1063/1.4818328

[29] A. F. Voter, Parallel replica method for dynamics of infrequent events, Physical Review B 57 (22) (1998) R13985.

[30] R. Gutiérrez, S. Karmakar, Y. G. Pollack, I. Procaccia, The static lengthscale characterizing the glass transition at lower temperatures, EPL (Europhysics Letters) 111 (5) (2015) 56009. doi:10.1209/0295-5075/111/56009.

[31] K. Lindorff-Larsen, S. Piana, R. O. Dror, D. E. Shaw, How fast-folding proteins fold, Science 334 (6055) (2011) 517–520. doi:10.1126/science.1208351.

[32] D. Hamelberg, J. Mongan, J. A. McCammon, Accelerated molecular dynamics: A promising and efficient simulation method for biomolecules, The Journal of Chemical Physics 120 (24) (2004) 11919–11929. arXiv:https://doi.org/10.1063/1.1755656, doi:10.1063/1.1755656.
URL https://doi.org/10.1063/1.1755656

[33] A. Laio, M. Parrinello, Escaping free-energy minima, Proceedings of the National Academy of Sciences 99 (20) (2002) 12562–12566. doi:10.1073/pnas.202427399.

[34] A. Laio, F. L. Gervasio, Metadynamics: a method to simulate rare events and reconstruct the free energy in biophysics, chemistry and material science, Reports on Progress in Physics 71 (12) (2008) 126601.

[35] A. Barducci, M. Bonomi, M. Parrinello, Metadynamics, Wiley Interdisciplinary Reviews: Computational Molecular Science 1 (5) (2011) 826–843. doi:10.1002/wcms.31.

[36] J. Comer, J. C. Gumbart, J. Hénin, T. Lelièvre, A. Pohorille, C. Chipot, The adaptive biasing force method: Everything you always wanted to know but were afraid to ask, The Journal of Physical Chemistry B 119 (3) (2015) 1129–1151, pMID: 25247823. arXiv:https://doi.org/10.1021/jp506633n, doi:10.1021/jp506633n.
URL https://doi.org/10.1021/jp506633n

[37] P. Tiwary, A. van de Walle, A Review of Enhanced Sampling Approaches for Accelerated Molecular Dynamics, Springer International Publishing, Cham, 2016, pp. 195–221. doi:10.1007/978-3-319-33480-6.
URL https://doi.org/10.1007/978-3-319-33480-6

[38] D. Perez, B. P. Uberuaga, Y. Shim, J. G. Amar, A. F. Voter, Accelerated molecular dynamics methods: introduction and recent developments, Annual Reports in computational chemistry 5 (2009) 79–98.

[39] A. F. Voter, F. Montalenti, T. C. Germann, Extending the time scale in atomistic simulation of materials, Annual Review of Materials Research 32 (1) (2002) 321–346. arXiv:https://doi.org/10.1146/annurev.matsci.32.112601.141541, doi:10.1146/annurev.matsci.32.112601.141541.
URL https://doi.org/10.1146/annurev.matsci.32.112601.141541

[40] D. Alhat, V. Lasrado, Y. Wang, A review of recent phase transition simulation methods: Saddle point search, Proceedings of the ASME Design Engineering Technical Conference 1. doi:10.1115/DETC2008-49411.

[41] A. Barducci, M. Bonomi, M. Parrinello, Metadynamics, Wiley Interdisciplinary Reviews: Computational Molecular Science 1 (5) 826–843. arXiv:https://onlinelibrary.wiley.com/doi/pdf/10.1002/wcms.31, doi:10.1002/wcms.31.

[42] A. Barducci, G. Bussi, M. Parrinello, Well-tempered metadynamics: A smoothly converging and tunable free-energy method, Phys. Rev. Lett. 100 (2008) 020603. doi:10.1103/PhysRevLett.100.020603.
URL https://link.aps.org/doi/10.1103/PhysRevLett.100.020603

[43] A. Kushima, J. Eapen, J. Li, S. Yip, T. Zhu, Time scale bridging in atomistic simulation of slow dynamics: viscous relaxation and defect activation, The European Physical Journal B 82 (3) (2011) 271. doi:10.1140/epjb/e2011-20075-4.
URL https://doi.org/10.1140/epjb/e2011-20075-4

[44] N. Mousseau, G. T. Barkema, Traveling through potential energy landscapes of disordered materials: The activation-relaxation technique, Phys. Rev. E 57 (1998) 2419–2424. doi:10.1103/PhysRevE.57.2419.

[45] W. E, X. Zhou, The gentlest ascent dynamics, Nonlinearity 24 (6) (2011) 1831–1842. doi:10.1088/0951-7715/24/6/008.

[46] G. Henkelman, B. P. Uberuaga, H. Jónsson, A climbing image nudged elastic band method for finding saddle points and minimum energy paths, The Journal of Chemical Physics 113 (22) (2000) 9901–9904. doi:10.1063/1.1329672.

[47] P. M. Zimmerman, Growing string method with interpolation and optimization in internal coordinates: Method and examples, The Journal of Chemical Physics 138 (18) (2013) 184102. arXiv:https://doi.org/10.1063/1.4804162, doi:10.1063/1.4804162.
URL https://doi.org/10.1063/1.4804162

[48] Y. Sun, X. Zhou, An improved adaptive minimum action method for the calculation of transition path in non-gradient systems (2017). arXiv:arXiv:1701.04044.

[49] S. T. Chill, J. Stevenson, V. Ruehle, C. Shang, P. Xiao, J. D. Farrell, D. J. Wales, G. Henkelman, Benchmarks for characterization of minima, transition states, and pathways in atomic, molecular, and condensed matter systems, Journal of Chemical Theory and Computation 10 (12) (2014) 5476–5482, pMID: 26583230. arXiv:https://doi.org/10.1021/ct5008718, doi:10.1021/ct5008718.
URL https://doi.org/10.1021/ct5008718

[50] Y. Zeng, P. Xiao, G. Henkelman, Unification of algorithms for minimum mode optimization, The Journal of Chemical Physics 140 (4) (2014) 044115. arXiv:https://doi.org/10.1063/1.4862410, doi:10.1063/1.4862410.
URL https://doi.org/10.1063/1.4862410

[51] W. Lechner, C. Dellago, Accurate determination of crystal structures based on averaged local bond order parameters, The Journal of Chemical Physics 129 (11).

[52] N. P. Walter, A. Jaiswal, Z. Cai, Y. Zhang, Liquidlib: A comprehensive toolbox for analyzing classical and ab initio molecular dynamics simulations of liquids and liquid-like matter with applications to neutron scattering experiments, Computer Physics Communications 228 (2018) 209 – 218. doi:https://doi.org/10.1016/j.cpc.2018.03.005.
URL http://www.sciencedirect.com/science/article/pii/S0010465518300778

[53] J. S. van Duijneveldt, D. Frenkel, Computer simulation study of free energy barriers in crystal nucleation, The Journal of Chemical Physics 96 (6) (1992) 4655–4668. doi:10.1063/1.462802.

[54] P. R. ten Wolde, M. J. Ruiz-Montero, D. Frenkel, Numerical calculation of the rate of crystal nucleation in a lennard-jones system at moderate undercooling, The Journal of Chemical Physics 104 (24) (1996) 9932–9947. doi:10.1063/1.471721.

[55] K. Iland, J. Wedekind, J. Wölk, P. E. Wagner, R. Strey, Homogeneous nucleation rates of 1-pentanol, The Journal of Chemical Physics 121 (24) (2004) 12259–12264. doi:10.1063/1.1809115.

[56] P. Debenedetti, Metastable Liquids: Concepts and Principles, Physical chemistry : science and engineering, Princeton University Press, 1996.

[57] B. Mutaftschiev, The Atomistic Nature of Crystal Growth, Springer Series in Materials Science, Springer Berlin Heidelberg, 2001.
URL https://books.google.com/books?id=XesJbYTQk_8C

[58] H. Vehkamäki, Classical nucleation theory in multicomponent systems, Springer Science & Business Media, 2006.

[59] J. R. Espinosa, C. Vega, C. Valeriani, E. Sanz, Seeding approach to crystal nucleation, Journal of Chemical Physics 144 (3). doi:10.1063/1.4939641.
URL http://dx.doi.org/10.1063/1.4939641

[60] E. Sanz, C. Vega, J. R. Espinosa, R. Caballero-Bernal, J. L. F. Abascal, C. Valeriani, Homogeneous ice nucleation at moderate supercooling from molecular simulation, Journal of the American Chemical Society 135 (40) (2013) 15008–15017. arXiv:arXiv:1312.0822v1, doi:10.1021/ja4028814.

[61] J.-P. Hansen, I. R. McDonald, third edition Edition, Academic Press, Burlington, 2006. doi:http://dx.doi.org/10.1016/B978-012370535-8/50003-3.

[62] J.-P. Hansen, L. Verlet, Phase transitions of the lennard-jones system, Phys. Rev. 184 (1969) 151–161. doi:10.1103/PhysRev.184.151.

[63] T. Kawasaki, H. Tanaka, Formation of a crystal nucleus from liquid, Proceedings of the National Academy of Sciences 107 (32) (2010) 14036–14041. arXiv:https://www.pnas.org/content/107/32/14036.full.pdf, doi:10.1073/pnas.1001040107.
URL https://www.pnas.org/content/107/32/14036

[64] L. A. Zepeda-Ruiz, B. Sadigh, A. A. Chernov, T. Haxhimali, A. Samanta, T. Oppelstrup, S. Hamel, L. X. Benedict, J. L. Belof, Extraction of effective solid-liquid interfacial free energies for full 3d solid crystallites from equilibrium md simulations, The Journal of Chemical Physics 147 (19) (2017) 194704. arXiv:https://doi.org/10.1063/1.4997595, doi:10.1063/1.4997595.
URL https://doi.org/10.1063/1.4997595

[65] R. L. Davidchack, B. B. Laird, Direct calculation of the hard-sphere crystal /melt interfacial free energy, Phys. Rev. Lett. 85 (2000) 4751–4754. doi:10.1103/PhysRevLett.85.4751.
URL https://link.aps.org/doi/10.1103/PhysRevLett.85.4751

[66] J. Q. Broughton, G. H. Gilmer, Molecular dynamics investigation of the crystal–fluid interface. vi. excess surface free energies of crystal–liquid systems, The Journal of Chemical Physics 84 (10) (1986) 5759–5768. arXiv:https://doi.org/10.1063/1.449884, doi:10.1063/1.449884.
URL https://doi.org/10.1063/1.449884

[67] D. Branduardi, G. Bussi, M. Parrinello, Metadynamics with adaptive gaussians, Journal of Chemical Theory and Computation 8 (7) (2012) 2247–2254, pMID: 26588957. arXiv:https://doi.org/10.1021/ct3002464, doi:10.1021/ct3002464.
URL https://doi.org/10.1021/ct3002464

[68] J. F. Dama, G. M. Hocky, R. Sun, G. A. Voth, Exploring valleys without climbing every peak: More efficient and forgiving metabasin metadynamics via robust on-the-fly bias domain restriction, Journal of Chemical Theory and Computation 11 (12) (2015) 5638–5650, pMID: 26587809. arXiv:https://doi.org/10.1021/acs.jctc.5b00907, doi:10.1021/acs.jctc.5b00907.
URL https://doi.org/10.1021/acs.jctc.5b00907

[69] G. Barkema, N. Mousseau, The activation–relaxation technique: an efficient algorithm for sampling energy landscapes, Computational Materials Science 20 (3) (2001) 285 – 292, 9th Int. Workshop on Computational Materials Science. doi:https://doi.org/10.1016/S0927-0256(00)00184-1.
URL http://www.sciencedirect.com/science/article/pii/S0927025600001841

[70] R. Malek, N. Mousseau, Dynamics of lennard-jones clusters: A characterization of the activation-relaxation technique, Physical Review E 62 (6) (2000) 7723.

[71] N. Mousseau, G. Barkema, Activated mechanisms in amorphous silicon: An activation-relaxation-technique study, Physical Review B 61 (3) (2000) 1898.

[72] G. Wei, N. Mousseau, P. Derreumaux, Exploring the energy landscape of proteins: A characterization of the activation-relaxation technique, The Journal of chemical physics 117 (24) (2002) 11379–11387.

[73] R. Larson, Elementary Linear Algebra, Cengage Learning, 2012.
URL https://books.google.com/books?id=rqWCVMYk5mEC

[74] A. Samanta, W. E, Atomistic simulations of rare events using gentlest ascent dynamics, The Journal of Chemical Physics 136 (12) (2012) 124104. arXiv:https://doi.org/10.1063/1.3692803, doi:10.1063/1.3692803.
URL https://doi.org/10.1063/1.3692803

[75] M. Chen, T.-Q. Yu, M. E. Tuckerman, Locating landmarks on high-dimensional free energy surfaces, Proceedings of the National Academy of Sciences 112 (11) (2015) 3235–3240. arXiv:https://www.pnas.org/content/112/11/3235.full.pdf, doi:10.1073/pnas.1418241112.
URL https://www.pnas.org/content/112/11/3235

[76] A. Samanta, M. Chen, T.-Q. Yu, M. Tuckerman, W. E, Sampling saddle points on a free energy surface, The Journal of Chemical Physics 140 (16) (2014) 164109. arXiv:https://doi.org/10.1063/1.4869980, doi:10.1063/1.4869980.
URL https://doi.org/10.1063/1.4869980

[77] J. M. Bofill, W. Quapp, The variational nature of the gentlest ascent dynamics and the relation of a variational minimum of a curve and the minimum energy path, Theoretical Chemistry Accounts 135 (1) (2015) 11. doi:10.1007/s00214-015-1767-7.
URL https://doi.org/10.1007/s00214-015-1767-7

[78] C. Li, J. Lu, W. Yang, Gentlest ascent dynamics for calculating first excited state and exploring energy landscape of kohn-sham density functionals, The Journal of Chemical Physics 143 (22) (2015) 224110. arXiv:https://doi.org/10.1063/1.4936411, doi:10.1063/1.4936411.
URL https://doi.org/10.1063/1.4936411

[79] A. Levitt, C. Ortner, Convergence and cycling in walker-type saddle search algorithms, SIAM Journal on Numerical Analysis 55. doi:10.1137/16M1087199.

[80] J. M. Bofill, W. Quapp, M. Caballero, Locating transition states on potential energy surfaces by the gentlest ascent dynamics, Chemical Physics Letters 583 (2013) 203 – 208. doi:https://doi.org/10.1016/j.cplett.2013.07.074.
URL http://www.sciencedirect.com/science/article/pii/S0009261413009652

[81] S. Gu, X. Zhou, Multiscale gentlest ascent dynamics for saddle point in effective dynamics of slow-fast system (2016). arXiv:arXiv:1602.00953.

[82] W. Gao, J. Leng, X. Zhou, Iterative minimization algorithm for efficient calculations of transition states, Journal of Computational Physics 309 (2016) 69 – 87. doi:https://doi.org/10.1016/j.jcp.2015.12.056.
URL http://www.sciencedirect.com/science/article/pii/S0021999115008815

[83] S. Gu, X. Zhou, Simplified gentlest ascent dynamics for saddle points in non-gradient systems, Chaos: An Interdisciplinary Journal of Nonlinear Science 28 (12) (2018) 123106. arXiv:https://doi.org/10.1063/1.5046819, doi:10.1063/1.5046819.
URL https://doi.org/10.1063/1.5046819

[84] W. Quapp, J. Maria Bofill, Embedding of the saddle point of index two on the pes of the ring opening of cyclobutene, International Journal of Quantum Chemistry 115 (23) 1635–1649. arXiv:https://onlinelibrary.wiley.com/doi/pdf/10.1002/qua.24996, doi:10.1002/qua.24996.
URL https://onlinelibrary.wiley.com/doi/abs/10.1002/qua.24996

[85] W. Quapp, J. M. Bofill, Locating saddle points of any index on potential energy surfaces by the generalized gentlest ascent dynamics, Theoretical Chemistry Accounts 133 (8) (2014) 1510. doi:10.1007/s00214-014-1510-9.
URL https://doi.org/10.1007/s00214-014-1510-9

[86] P. Collins, G. S. Ezra, S. Wiggins, Index k saddles and dividing surfaces in phase space with applications to isomerization dynamics, The Journal of Chemical Physics 134 (24) (2011) 244105. arXiv:https://doi.org/10.1063/1.3602465, doi:10.1063/1.3602465.
URL https://doi.org/10.1063/1.3602465

[87] J. P. K. Doye, D. J. Wales, Saddle points and dynamics of lennard-jones clusters, solids, and supercooled liquids, The Journal of Chemical Physics 116 (9) (2002) 3777–3788. arXiv:https://doi.org/10.1063/1.1436470, doi:10.1063/1.1436470.
URL https://doi.org/10.1063/1.1436470

[88] A. Cavagna, Fragilevs.strong liquids: A saddles-ruled scenario, Europhysics Letters (EPL) 53 (4) (2001) 490–496. doi:10.1209/epl/i2001-00179-4.

[89] D. Coslovich, G. Pastore, Understanding fragility in supercooled lennard-jones mixtures. ii. potential energy surface, The Journal of Chemical Physics 127 (12) (2007) 124505. arXiv:https://doi.org/10.1063/1.2773720, doi:10.1063/1.2773720.
URL https://doi.org/10.1063/1.2773720

[90] D. Heidrich, W. Quapp, Saddle points of index 2 on potential energy surfaces and their role in theoretical reactivity investigations, Theoretica chimica acta 70 (2) (1986) 89–98. doi:10.1007/BF00532206.
URL https://doi.org/10.1007/BF00532206

[91] Z. Yao, M. O. de la Cruz, Dynamics of vacancies in two-dimensional lennard-jones crystals, Phys. Rev. E 90 (2014) 062318. doi:10.1103/PhysRevE.90.062318.
URL https://link.aps.org/doi/10.1103/PhysRevE.90.062318

[92] A. Ninarello, L. Berthier, D. Coslovich, Models and algorithms for the next generation of glass transition studies, Phys. Rev. X 7 (2017) 021039. doi:10.1103/PhysRevX.7.021039.
URL https://link.aps.org/doi/10.1103/PhysRevX.7.021039

[93] M. Ozawa, L. Berthier, Does the configurational entropy of polydisperse particles exist?, The Journal of Chemical Physics 146 (1) (2017) 014502. arXiv:https://doi.org/10.1063/1.4972525, doi:10.1063/1.4972525.
URL https://doi.org/10.1063/1.4972525

[94] D. J. Wales, J. P. K. Doye, Stationary points and dynamics in high-dimensional systems, The Journal of Chemical Physics 119 (23) (2003) 12409–12416. arXiv:https://doi.org/10.1063/1.1625644, doi:10.1063/1.1625644.
URL https://doi.org/10.1063/1.1625644

[95] T. S. Grigera, Geometrical properties of the potential energy of the soft-sphere binary mixture, The Journal of Chemical Physics 124 (6) (2006) 064502. arXiv:https://doi.org/10.1063/1.2151899, doi:10.1063/1.2151899.
URL https://doi.org/10.1063/1.2151899

[96] L. Angelani, G. Ruocco, F. Zamponi, Saddles and dynamics in a solvable mean-field model, The Journal of Chemical Physics 118 (18) (2003) 8301–8306. arXiv:https://doi.org/10.1063/1.1565996, doi:10.1063/1.1565996.
URL https://doi.org/10.1063/1.1565996

[97] A. R. Dexter, A. J. Matheson, Elastic moduli and stress relaxation times in liquid argon, The Journal of Chemical Physics 54 (1) (1971) 203–208. doi:10.1063/1.1674594.

[98] W. Kob, H. C. Andersen, Testing mode-coupling theory for a supercooled binary lennard-jones mixture i: The van hove correlation function, Physical Review E 51 (5) (1995) 4626.

[99] J. Kubelka, J. Hofrichter, W. A. Eaton, The protein folding 'speed limit', Current Opinion in Structural Biology 14 (1) (2004) 76 – 88. doi:https://doi.org/10.1016/j.sbi.2004.01.013.
URL http://www.sciencedirect.com/science/article/pii/S0959440X04000144

[100] G. L. Squires, Introduction to the Theory of Thermal Neutron Scattering, 3rd Edition, Cambridge University Press, 2012, cambridge Books Online.

[101] J. Leng, W. Gao, C. Shang, Z.-P. Liu, Efficient softest mode finding in transition states calculations, The Journal of Chemical Physics 138 (9) (2013) 094110. arXiv:https://doi.org/10.1063/1.4792644, doi:10.1063/1.4792644.
URL https://doi.org/10.1063/1.4792644

[102] C. Lavor, N. Maculan, Reducing the cost of evaluation of the gradient and hessian of molecular potential energy functions (2004) 275–287.

[103] M. Scott Shell, P. G Debenedetti, A. Panagiotopoulos, Saddles in the energy landscape: Extensivity and thermodynamic formalism, Physical review letters 92 (2004) 035506. doi:10.1103/PhysRevLett.92.035506.

[104] W. Kob, H. C. Andersen, Testing mode-coupling theory for a supercooled binary lennard-jones mixture i: The van hove correlation function, Phys. Rev. E 51 (1995) 4626–4641. doi:10.1103/PhysRevE.51.4626.
URL https://link.aps.org/doi/10.1103/PhysRevE.51.4626

[105] T. Urbic, V. Vlachy, K. A. Dill, Confined water: A mercedes-benz model study, The Journal of Physical Chemistry B 110 (10) (2006) 4963–4970, pMID: 16526737. arXiv:https://doi.org/10.1021/jp055543f, doi:10.1021/jp055543f.
URL https://doi.org/10.1021/jp055543f

[106] A. Scukins, V. Bardik, E. Pavlov, D. Nerukh, Molecular dynamics implementation of bn2d or 'mercedes benz' water model, Computer Physics Communications 190 (2015) 129 – 138. doi:https://doi.org/10.1016/j.cpc.2014.12.019.
URL http://www.sciencedirect.com/science/article/pii/S0010465515000053